

Received 27 November 2022, accepted 7 December 2022, date of publication 26 December 2022, date of current version 3 January 2023.

Digital Object Identifier 10.1109/ACCESS.2022.3232561

TOPICAL REVIEW

UNet Deep Learning Architecture for Segmentation of Vascular and Non-Vascular Images: A Microscopic Look at UNet Components Buffered With Pruning, Explainable Artificial Intelligence, and Bias

JASJIT S. SURI¹, (Fellow, IEEE), MRINALINI BHAGAWATI²,
SUSHANT AGARWAL^{3,4}, (Member, IEEE), SUDIP PAUL⁵, (Senior Member, IEEE),
AMIT PANDEY⁵, SUNEET K. GUPTA⁵, (Member, IEEE), LUCA SABA⁶,
KOSMAS I. PARASKEVAS⁷, NARENDRA N. KHANNA⁸, JOHN R. LAIRD⁹, AMER M. JOHRI¹⁰,
MANUDEEP K. KALRA¹¹, MOSTAFA M. FOUDA¹², (Senior Member, IEEE),
MOSTAFA FATEMI¹³, (Life Fellow, IEEE), AND SUBBARAM NAIDU¹⁴, (Life Fellow, IEEE)

¹Stroke Diagnostic and Monitoring Division, AtheroPoint, Roseville, CA 95661, USA²Department of Biomedical Engineering, North-Eastern Hill University, Shillong 793022, India³TechNet Cyber Solutions Pvt. Ltd., Andhra Pradesh 530045, India⁴Advanced Knowledge Engineering Centre, GBTI, Roseville, CA 95661, USA⁵Department of Computer Science, Bennett University, Greater Noida 201310, India⁶Department of Radiology, University of Cagliari, 09124 Cagliari, Italy⁷Department of Vascular Surgery, Central Clinic of Athens, 14122 Athens, Greece⁸Department of Cardiology, Indraprastha Apollo Hospitals, New Delhi 110076, India⁹Cardiology Department, St. Helena Hospital, St. Helena, CA 94574, USA¹⁰Department of Medicine, Division of Cardiology, Queen's University, Kingston, ON K7L 3N6, Canada¹¹Department of Radiology, Massachusetts General Hospital, Boston, MA 02114, USA¹²Department of Electrical and Computer Engineering, Idaho State University, Pocatello, ID 83209, USA¹³Department of Physiology and Biomedical Engineering, Mayo Clinic College of Medicine and Science, Rochester, MN 55441, USA¹⁴Electrical Engineering Department, University of Minnesota, Duluth, MN 55812, USA

Corresponding author: Jasjit S. Suri (jasjit.suri@atheropoint.com)

ABSTRACT Biomedical image segmentation (BIS) task is challenging due to the variations in organ types, position, shape, size, scale, orientation, and image contrast. Conventional methods lack accurate and automated designs. Artificial intelligence (AI)-based UNet has recently dominated BIS. This is the first review of its kind that microscopically addressed UNet types by complexity, stratification of UNet by its components, addressing UNet in vascular vs. non-vascular framework, the key to segmentation challenge vs. UNet-based architecture, and finally interfacing the three facets of AI, the pruning, the explainable AI (XAI), and the AI-bias. PRISMA was used to select 267 UNet-based studies. Five classes were identified and labeled as conventional UNet, superior UNet, attention-channel UNet, hybrid UNet, and ensemble UNet. We discovered 81 variations of UNet by considering six kinds of components, namely encoder, decoder, skip connection, bridge network, loss function, and their combination. Vascular vs. non-vascular UNet architecture was compared. AP(ai)Bias 2.0-UNet was identified in these UNet classes based on (i) attributes of UNet architecture and its performance, (ii) explainable AI (XAI), and, (iii) pruning (compression). Five bias methods such as (i) ranking, (ii) radial, (iii) regional area, (iv) PROBAST, and (v) ROBINS-I were applied and compared using a Venn diagram. Vascular and non-vascular UNet systems dominated with sUNet classes with attention. Most of the studies suffered from a low interest in XAI and pruning strategies. None of the UNet models qualified to be bias-free. There is a need to move from paper-to-practice paradigms for clinical evaluation and settings.

The associate editor coordinating the review of this manuscript and approving it for publication was Chulhong Kim¹⁵.

• **INDEX TERMS** Image segmentation, vascular, non-vascular, UNet classes, UNet variations, UNet-components, explainable AI, pruning, bias.

I. INTRODUCTION

Segmentation, the branch of computer vision that has shown its variations in the form of cycles over the last 50 years [1] from regional-based [2] to boundary-based techniques such as parametric-based snakes [3] or geometric-based level sets [4], and just recently in the artificial intelligence (AI)-based framework [5], [6], [7]. It was exactly 20 years ago that the geometric-based level set paradigm for segmentation was introduced by Sethian and extended in medical imaging by Suri [8], [9].

The concept of level set image segmentation was based on the paradigm of traversing the zero-level curves using partial differential equations (PDE) and clamping the final boundaries at the high gradient edge points [10], [11]. Level set-based geometric curves suffered due to initialization of the segmentation curves which was later automated [12], however, it still needed several speed functions or regularization terms to prevent bleeding of the boundaries of the segmented organs [13]. This bleeding was due to factors like local noise, incomplete shape information, poor digitization or acquisition of target organs in images, leading to lower performance of Jaccard index or Dice similarities [14]. Thus, there was a clear need for knowledge-based innovation.

The fundamental concept of deriving knowledge by fusing the image features extracted from the training database and corresponding gold standard, and later applying it in the classification or characterization framework, was tapped by the machine learning framework [15], [16]. A mammoth of literature exists in various applications under the class of computer-aided diagnosis [17], [18], [19], [20] and covers several medical imaging modalities such as magnetic resonance [21], computed tomography [22], and ultrasound [23]. Although such training models are powerful, they suffer from (a) the ad-hoc training feature extraction and (b) training optimization frameworks to prevent gridlock due to noise while using gradient search for local minima [24]. Thus, under the class of AI, machine learning (ML) transpired for some duration, until recently, the power of automated feature extraction for segmentation was desired in the deep learning (DL) framework [6], [20], such as UNet [25]. A typical flowchart using UNet-based diagnosis is shown in Figure 1. The UNet-based segmentation is designed in a pruning paradigm (removing redundant weights during propagation) and visualized using explainable AI (XAI), with performance evaluated using the mean alignment index (MAI) where expert rates the error between AI output and Ground Truth (GT).

While UNet-based DL foundation models have been evolving for the last *five* years, the concept of (i) scales, size, shape, orientation, position, (ii) filter sizes, (iii) feature extraction using encoders, (iv) image reconstruction using decoders, (v) fusion of low-level and high-level features via

skip connection, (vi) dimensions of image modalities, and finally, (iv) covering the spectrum from *vascular* (angiography) to *non-vascular* paradigms is not well presented [26]. While there are very limited number of UNet-based review articles, which we will discuss in the benchmarking subsection in discussion section, here, we present a classic framework to better understand these black boxes, which are adopted in a plug-and-play framework. Further, the computer vision industry is relentlessly pursuing to cherry-pick the hybridization process and tailor UNet components for their niche applications. While the computer vision industry gallops by wearing its own blinkers, there is a need to explore the scientific validation paradigm using explainable AI (XAI), which seems to be left behind. Further, these training models can be large in storage and slow in speed, thus, demand pruning of redundant weights. Lastly, since AI is prone to bias due to (i) poor data collection, (ii) low performing models, and (iii) overemphasis on the accuracy of these UNet models by memorizing the models, the concept of generalization needs to be revised in an “unseen AI” framework.

Thus, this study offers special attention to (i) showing the variations of UNet-based DL into *five* innovative categories, namely conventional UNet (cUNet), superior UNet (sUNet), attention-channel UNet (acUNet), hybrid UNet (hUNet), and ensemble UNet (eUNet); (ii) eight sUNet types were identified based on scale, parallel connection, cascade connections, integration of probability maps, role of residual models, role of feedback systems, context derivation, high-dimensional inputs, and finally loss function designs; (iii) understanding the 81 variations in UNets due to *six* types of variations in fundamental cUNet due to changes in encoder, decoder, skip connection, bridge network, and loss function; (iv) role of UNet in *vascular vs. non-vascular* segmentation paradigms in medical imaging: its architectural characteristics, difference, and similarities; (v) introducing “key for segmentation challenges and corresponding architecture solutions”; (vi) scientific validation using XAI; (vii) pruning paradigm to reduce the storage sizes and to improve speed; (viii) biases in UNet-based DL architectures; and finally, (ix) the recommendations ensuring the mapping between the segmentation type and UNet variations.

The hypothesis of this study states that the variations in the UNet, such as an encoder, decoder, skip connection, bridge network, loss function design, or input to the UNet, itself shall improve the performance of the UNet-based segmentation system. The performance can be in the form of speed, accuracy, receiver operating curves (ROC), or performance matrices. Such a variational UNet system can lead to better design towards XAI, bias, and possible new innovations in compressing the model size. This is the first study of its kind, which has spearheaded the understanding of these concepts by expanding the experienced wings of authors while

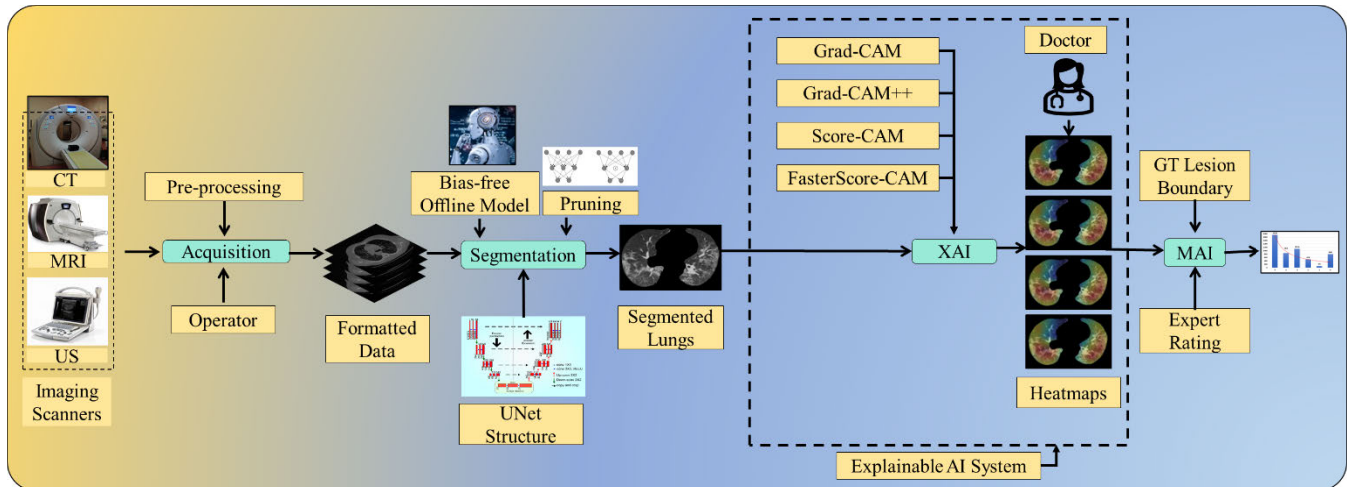


FIGURE 1. Flow diagram of UNet-based segmentation process. The pipeline consists of acquisition, segmentation via pruning trained models, XAI, and MAI.

demonstrating the architectural variations for *vascular* and *non-vascular* applications for the healthcare industry.

II. SEARCH STRATEGY AND STATISTICAL DISTRIBUTION

The statistical distribution of the literature is necessary to understand the types of UNet in *vascular* and *non-vascular* paradigm distributions, understanding the variations in the components of UNet, participation of the feature extraction methods, types of performance parameters, and their frequency in the selected studies, pruning models for storage reduction, XAI techniques for UNet, and bias in the AI-based solutions. Thus, we adapt the PRISMA model for the selection of the studies for the UNet, XAI, pruning, and bias assessment [27], [28], [29], [30], [31], [32], [33], [34]. Therefore, this section is therefore divided into two parts: section II.A discusses the study selection criteria and section II.B presents the statistical distributions.

A. PRISMA MODEL

The selection and searching of the studies for this review were conducted using the PRISMA model. The keywords used for the search were “UNet for *vascular* studies”, “UNet for *non-vascular* studies”, “UNet variations for segmentation”, “UNet-based segmentation”, “UNet-based segmentation of coronary artery using IVUS”, “UNet-based segmentation of carotid artery”, “UNet-based segmentation of aorta or aortic artery”, “UNet-based segmentation of peripheral artery”, “UNet-based segmentation of retinal scans or fundus images”, “UNet-based segmentation of brachial images”, “UNet-based segmentation of brain, liver, kidney, knee, prostate, COVID-19 lesions”, “AI-Bias in UNet”, “Pruning methods for UNet”, “Storage size of UNet-based”, “Explainable-AI for UNet-based segmentation methods” and combination of these. The different search platforms used were Science Direct, IEEE Xplore, PubMed, and Google Scholar. The PRISMA flow chart for selected studies is shown in Figure 2. An exhaustive search resulted in

a total of 2,672 studies. The three criteria used for exclusion were (a) non-relevant studies (b) articles removed after search and screening of the studies (c) records rejected due to insufficient data. The implementation of exclusion criteria provided 2,307, 88, and 10 studies for exclusion, shown by E1, E2, and E3 (Figure 2). The important scientific knowledge from these final studies was gained, and the statistical classification was drawn. The architecture, their features, UNet classification, bias estimation, explainable AI, and pruning were used to the analysis [35].

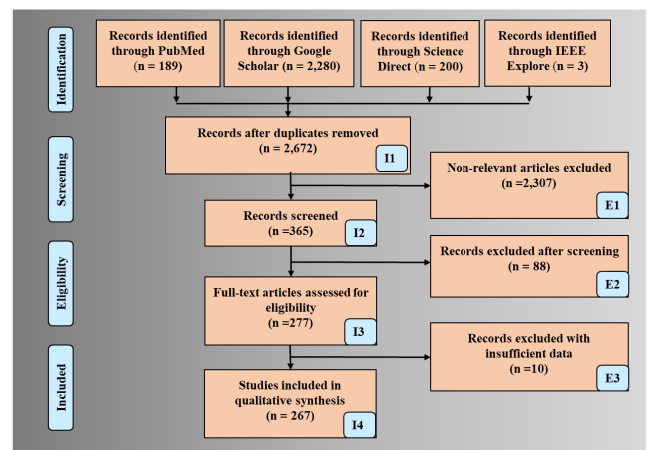


FIGURE 2. PRISMA model for selection of the UNet-based CVD studies.

B. STATISTICAL DISTRIBUTION

The statistical distribution was done to analyze the aspect or feature of UNet-based DL systems. The distribution was done for the publication per year (Figure 3 (a)), field of view or application (Figure 3 (b)), UNet types used among the systems (Figure 3 (c)), and performance parameter used (Figure 3 (d)) *vascular* vs. *non-vascular* (Figure 3 (e)), and UNet variation types (Figure 3 (f)).

III. STRATIFICATION OF UNET ARCHITECTURES

A. BASIC UNET ARCHITECTURE AND ITS COMPONENTS

UNet-based DL has recently dominated the medical image segmentation industry in nearly all body imaging modalities, harnessing the power of automated feature extraction and reconstruction of desired shapes. It was in 2015 when Ronneberger et al. [25] first introduced UNet as a way of image segmentation for benchmarking against standard conventional segmentation approaches. This UNet architecture is shown in Figure 4. The main components of UNet architecture are encoders, decoders, bridge network, skip connection, loss function criteria, and the process of binary conversion (so-called softmax layer). This historical innovation of down-convolution, and up-convolution, when combined with the ability to pick the highest-level relevant information or features, so-called max pooling, added the fuel to the fire towards the process of automated feature extraction [25]. The ability to transfer the feature information from the encoder to decoder phases of the UNet-based DL model retains the desired features during the shape reconstruction (decoder phase). In contrast to level set-based geometric curves, UNet-based DL does not need manual placement of the initial curves. However, it requires the gold standard for training of the UNet-based DL models. Thus, it is supervised UNet in nature, which is the focus of this study. It was only a minor improvement in image segmentation, but it has now dominated the computer vision, image processing, and artificial intelligence industries.

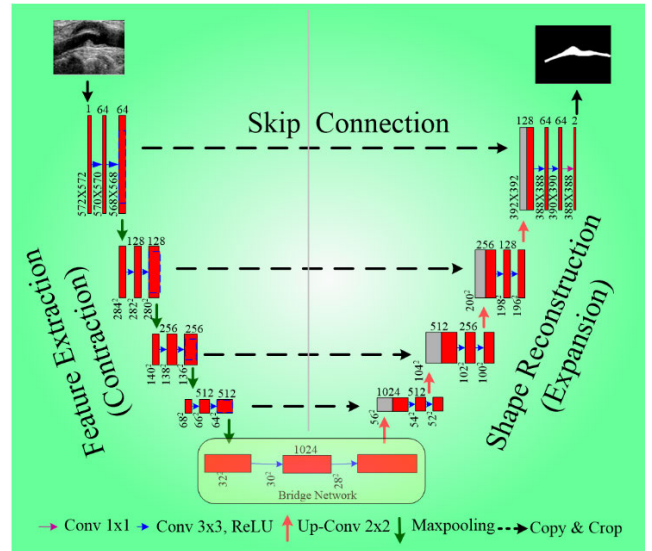


FIGURE 4. Basic UNet architecture showing encoder, decoder, bridge network, and skip connection. Encoder layers (contraction phase): feature extraction, and Decoder layers (expansion phase): shape reconstruction.

to understand the engraving application path in computer vision industry. Based on the UNet’s complexity and superiority evolution, we have classified the UNet series for segmentation application into *five* major classes and attempted the first time, dubbed cUNet, sUNet, acUNet, hUNet, and eUNet. Table 1 shows the comparison these *five* types of UNet classes having *seven* cluster of attributes, labeled as (i) C1: demographics, risk factors, and field-of-view, (ii) C2: UNet architecture components, (iii) C3: number of UNet types on each of the five classes, (iv) C4: UNet performance, (v) C5: statistical tests, (vi) C6: benchmarking, and (vii) C7: clinical analysis. Note that, even though all attributes of the UNet classes are important, however, UNet types in each class (labelled as column UT) is vital to understand since it talks about the growth or evolution of UNet enveloping image processing and computer vision industry. Following are the major and interesting inferences derived from the Table 1: (i) acUNet used all kinds of medical imaging modalities such as MRI, CT, X-ray, and US; (ii) cUNet, acUNet, and sUNet were mainly implemented covering the field of view (FoV) of immunology, pulmonary affected by COVID-19 [36], odontology (dental), and Angiography such as carotid, and neurology (brain). Since COVID-19 is a still a major health crisis [36], [37], [38], [39], [40], [41], so cUNet was first adopted in this framework. The same reason holds for the pulmonary FoV; (iii) All UNet classes had four to five layers, expect sUNet that had up to a maximum of 13 layers [42], [43], [44], [45], [46], [47], [48], [49], [50], [51], [52], [53], [54]. Note that as the number of layers increase, the DL system becomes more complex; (iv) Cross-Entropy (CE) loss function was most common or popular in all the five types of UNet [42], [43], [44], [45], [46], [47], [48], [49], [50], [51], [52], [53], [54], [55], [56], [57], [58], [59], [60],

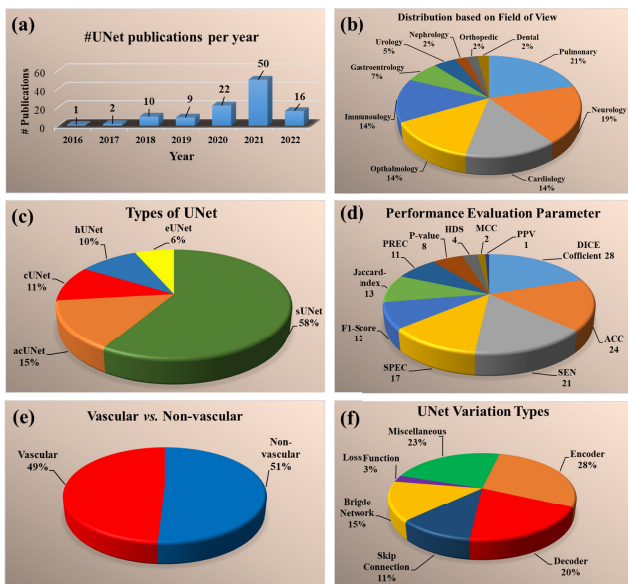


FIGURE 3. Statistical distribution (a) number of UNet publications per year; (b) distribution based on field of view or applications; (c) five types of UNet; (d) performance evaluation parameter of UNet evaluation; (e) vascular vs. non-vascular; and (f) UNet variation types.

B. FIVE TYPES OF UNET AND THEIR ATTRIBUTES

The dominance of UNet for segmentation is in its infancy stage, and it is vital to grasp its power of expansion now

TABLE 1. Comparison of five types of UNet (cUNet, sUNet, acUNet, hUNet, and eUNet) using seven clusters. (C1, C2, C3, C4, C5, C6, and C7)

UNet C	Cluster (right)	C1: Demographics, Risk Factors, Field of View						C2: UNet Architecture Components						C3: UT	C4: UNet Performance Evaluation										C5: UNet Statistical Test					C6: Bm	C7: Clinical				
		References	TP*	FH	RFT	IM	MC	FOV	EL	DL	ConvT	LossT	Optm		BgT	UT	SEN	SPE	ACC	PRE	F1S	PV	DS	Jl	MCC	PPV	HDS	StA	PwA		SciV	PTT	KWT	Bm	FDA
cUNet	[42-54]	20	✓	OBBM LBBM	IM3	×	F4	4	4	ReLU	CE	Adam	SC	1	✓	✓	✓	✓	×	✓	✓	✓	✓	×	×	✓	✓	✓	×	×	✓	×	✓	×	✓
sUNet	[49, 55-124]	50	✓	OBBM HT CS	IM4	✓	F4	4-13	4-13	ReLU	CE, Dice	Adam	SC	9	✓	✓	✓	✓	✓	✓	✓	✓	×	✓	✓	✓	✓	✓	✓	✓	✓	✓	×	×	✓
acUNet	[59, 113, 125-140]	58	✓	OBBM LBBM	IM2	✓	F3	4-5	4-5	ReLU	CE, Dice	Adam	SC	3	✓	✓	✓	✓	✓	×	✓	✓	×	×	✓	✓	✓	×	×	✓	×	✓	×	×	✓
hUNet	[53, 68-71, 74, 75, 113, 131, 141-143]	99	✓	OBBM LBBM	US	×	CTD	4	4	ReLU	CE	Adam	SC	2	✓	✓	✓	×	×	×	✓	✓	×	×	×	✓	✓	✓	×	×	✓	×	×	✓	
eUNet	[81, 93, 123, 144-148]	144	✓	OBBM LBBM	US	×	CTD	4	4	ReLU	CE	Adam	SC	1	✓	✓	✓	×	×	×	✓	✓	×	×	×	✓	✓	✓	×	×	✓	×	×	×	✓

UNet C: UNet Classification Types; TP*: Total patients range (cUNet: 20-1171, sUNet: 50-1302, acUNet: 58-500); RFT: Types of Risk Factors; HT: Histological types; CS: Clinical stages; IM: Imaging Modality; IM3: MRI, CT, US; IM4: MRI, CT, US, PET; IM2: MRI, CT; MC: Multicentre; FOV: Field of view; F4: Immunology, Pulmonary; Dental, Carotid, Neurology; CTD: Carotid; EL: Encoder layer; DL: Decoder layer; ConvT: Conouation type; LossT: Loss function type; CE: Cross-Entropy; Optm: Optimizer; BgT: Bridge network type; SC: Skip connection; UT: UNet types; SEN: Sensitivity; SPE: Specificity; A: Accuracy; PRE: Precision; F1S: F1 Score; PV: p -value; DS: Dice Similarity; Jl: Jaccard index; MCC: Mathew's correlation coefficient; PPV: Positive predictive value; HDS: Hausdorff distance-surface; StA: Statistical analysis; PwA: Power analysis; SciV: Scientific validation; PTT: Paired T-test; KWT: Kruskal-Wallis test; Bm: Benchmarking; FDA: Food and Drug Administration; CS: Clinical setting.

[61], [62], [63], [64], [65], [66], [67], [68], [69], [70], [71], [72], [73], [74], [75], [76], [77], [78], [79], [80], [81], [82], [83], [84], [85], [86], [87], [89], [90], [91], [92], [93], [94], [95], [96], [97], [98], [99], [100], [101], [102], [103], [104], [105], [106], [107], [108], [109], [110], [111], [112], [113], [114], [115], [116], [117], [118], [119], [120], [121], [122], [123], [124], [125], [126], [127], [128], [129], [130], [131], [132], [133], [134], [135], [136], [137], [138], [139], [140], [141], [142], [143], [144], [145], [146], [147], [148], while, Dice loss function was also part of cUNet and sUNet classes [42], [43], [44], [45], [46], [47], [48], [49], [50], [51], [52], [53], [54], [55], [56], [57], [58], [59], [60], [61], [62], [63], [64], [65], [66], [67], [68], [69], [70], [71], [72], [73], [74], [75], [76], [77], [78], [79], [80], [81], [82], [83], [84], [85], [86], [87], [89], [90], [91], [92], [93], [94], [95], [96], [97], [98], [99], [100], [101], [102], [103], [104], [105], [106], [107], [108], [109], [110], [111], [112], [113], [114], [115], [116], [117], [118], [119], [120], [121], [122], [123], [124]; (v) sUNet and acUNet were the two sets of classes which embraced multicenter studies [49], [55], [56], [57], [58], [59], [60], [61], [62], [63], [64], [65], [66], [67], [68], [69], [70], [71], [72], [73], [74], [75], [76], [77], [78], [79], [80], [81], [82], [83], [84], [85], [86], [87], [89], [90], [91], [92], [93], [94], [95], [96], [97], [98], [99], [100], [101], [102], [103], [104], [105], [106], [107], [108], [109], [110], [111], [112], [113], [114], [115], [116], [117], [118], [119], [120], [121], [122], [123], [124], [125], [126], [127], [128], [129], [130], [131], [132], [133], [134], [135], [136], [137], [138], [139], [140]. One reason could be the larger data set prompted for superior UNet designs. Lastly, note that since sUNet provides an easy pathway for variations, it was, therefore the most dominant of all the UNet types [49], [55], [56], [57], [58], [59], [60], [61], [62], [63], [64], [65], [66], [67], [68], [69], [70], [71], [72], [73], [74], [75], [76], [77], [78], [79], [80], [81], [82], [83], [84], [85], [86], [87], [89], [90], [91], [92], [93], [94], [95], [96], [97], [98], [99], [100], [101], [102], [103], [104], [105], [106], [107], [108], [109], [110], [111], [112], [113], [114], [115], [116], [117], [118], [119], [120], [121], [122], [123], [124]. We therefore have provided an exclusive study on the comparison of sUNet types ahead.

C. SUPERIOR UNET TYPES – A SPECIAL NOTE

The most well adapted UNet observed in our study was sUNet, which had evolved from cUNet by adding the variations in them. These sUNet had evolved based on the applications of the individual studies. We have taken special care by categorizing the sUNet into *eight* distinct types, that integrates concepts such as (i) scales (**sUNet.Scale**) [57], (ii) parallel connection of convolutions (**sUNet.Par**) [57], (iii) cascading (or tandem connection) of convolutions (**sUNet.Cascade**) [60], (iv) integration of probability maps for boundary extraction (**sUNet.Bndy**) [65], (v) tailoring of fundamental cUNet by residual network (ResNet) models (**sUNet.Res**) [59], [70], [75], [76], (vi) introducing feed-back system to improve cUNet performance (**sUNet.Feed**) [58] (vii) deriving the contextual encoder network information during the down sampling process (**sUNet.Context**) [74], (viii) change in dimensionality from 2-D to 3-D (**sUNet.Dim**) [59], [60], and (ix) adjustment in the loss function upgrades while up sampling during the reconstruction process (**sUNet.Loss**) [76]. The components of UNet that were changed are encoder (E), decoder (D), skip connection (SC), bridge network (BgN), and the loss function (LF). The sUNet tree with variations in E, D, SC, BgN building blocks were displayed in the Table 2 keeping *vascular* and *non-vascular* frameworks. As for the sUNet, the maximum variation is in the encoder (E) component for both *vascular* and *non-vascular*. A more detailed analysis for *vascular* vs. *non-vascular* will be presented in section VI.

IV. ANALYZING UNET COMPONENTS: A MICROSCOPIC LOOK

It is vital to understand the “components of the UNet architecture” which are responsible for processing the image data for the objective either in (i) segmentation (S) of medical organs or (ii) joint segmentation and classification (JSC) of the disease. Each of the components of the UNet architecture has a unique role in handling the complex nature of the image data. These UNet components are either used independently or jointly to effectively meet the objectives. Thus, we have now divided the UNet architecture into *six* types components variations, namely, (i) encoder; (ii) decoder; (iii) skip

connection; (iv) bridge network; (v) incorporating; (vi) loss functionality, and miscellaneous UNet design. These components are used in its entirety or the alterations in UNet that are categorized by changing the components of UNet, and hence classified as miscellaneous. Note that each of the components has its own function to handle shape, position, size, and scale of image objects in the image domain. Table 3 presents the in-depth coverage of the variations for each of the components of the UNet which are now discussed below.

A. ENCODER VARIATIONS

To begin with, the encoder is the most adapted and most changeable component of the UNet architecture. Since it is practically not possible to study each of the architectural variations in the encoder, we have therefore listed here the 23 variations (E1 to E23, representing encoder changes) along with their references in a tabular format and it is as follows: (E1) conventional system (Ronneberger) [43], [44], [45], [46], [47], [48], [49], [50], [51], [52], [90]; (E2) cascade of convolutions [77], [91], [99], [116], [117]; (E3) parallel convolutions (multiple convolution network) [57]; (E4) convolution with dropout [70], [76], [86], [95], [101], [102], [134], [138]; (E5) Residual network [76], [78], [105], [129], [135], [138], [149], [150], [151]; (E6) Xception encoder [56], [88], [112]; (E7) encoder layers with independent inputs [104, 140]; (E8) squeeze excitation (SE) network [92], [103], [138]; (E9) pooling types (max pooling, global average pooling) [95]; (E10) input image dimension change with changing filter (channels) [47], [74], [79], [99], [136], [152];

(E11) input image dimension 2D to 3D [59, 62, 81, 100, 141]; (E12) cascaded UNets where encoder of second UNet becomes input from the first decoder [123]; (E13) combination of exponential ReLU in encoder [89]; (E14) dilated convolution and activation function [67], [76]; (E15) Dense layer [68], [87], [91], [100], [102], [114], [122], [142]; (E16) boundary refinement [65]; (E17) batch normalization [95], [106], [125], [137], [155]; (E18) patch convolution and transformer [66], [94], [100], [105]; (E19) UNet++ type encoder change [144]; (E20) addition of original image to each layer [100]; (E21) Inception block [97], [102]; (E22) Ghost [118]; (E23) VGG16 [156]. A set of representative examples will be discussed in section 5.

B. DECODER VARIATIONS

Decoder plays a critical role in UNet design since it carries the outflow of the captured features from encoder, while retaining the image size using bilinear interpolation. The task of decoder is to ensure that the number of iterations per epoch are smoothly conducted using the designed loss function. Note that the decoder receives input in many different ways, such as encoder, skip connection or data after data transmission via bridge network (or bottle neck). Using these fundamental changes, the decoder variations can be categorized into 16 different type listed as follows: (D1) convolution

TABLE 2. sUNet Tree with variations in E, D, B building blocks.

SN	Author	EC	DC	BgC	Explanations changes in E, D, B, L	Performance JI/DS
Non-Vascular						
1	Ahmed <i>et al.</i> [55]	✓	✓	✗	E, D: Transposed 2D convolutional Layers; L: Dice	✗
2	Ajmera <i>et al.</i> [56]	✓	✗	✗	E: Xception; L: BCE	✗
3	Pezzano <i>et al.</i> [57]	✓	✗	✗	E: MCL; L: Hybrid	DS: 97
4	Voulodimos <i>et al.</i> [58]	✓	✓	✗	D: Few shot learning	DS: 77
5	Yang <i>et al.</i> [59]	✓	✓	✗	E: 3D conv., ResBlock; D: 3D conv., ResBlock	DS: 69
6	Cendejas-Zaragoza <i>et al.</i> [60]	✓	✓	✗	E: 3D conv; D: 3D conv. transpose	DS: 91
7	Jin1 <i>et al.</i> [153]	✗	✗	✓	B: DAC and RMP block	JI/DS: 90 and 82
8	Pan <i>et al.</i> [154]	✓	✓	✗	E, D: Conv (i,j)	JI: 95.41
9	Zhang <i>et al.</i> [61]	✗	✗	✓	B: Bridge normalization, L: Dice	DS: 86.23
10	Ma <i>et al.</i> [62]		✓	✗	D: Transverse Conv.	JI: 85.0
11	Chen <i>et al.</i> [67]	✓	✓	✗	E and D: Dilated Conv.	DS/JI: 97.43 and 96.27
12	Cao <i>et al.</i> [68]	✓	✗	✗	E: Dense Block	DS/JI: 69.02 and 56.61
13	Kumar <i>et al.</i> [69]	✗	✓	✓	D: Dense Block; B: Flatten	DS: 51.03
14	Rampun <i>et al.</i> [70]	✓	✗	✓	E: Residual Conv. Model; B: Dilated Conv. Model; L: Hybrid	DS/JI: 91.2 and 85.7
15	Wang <i>et al.</i> [71]	✗	✗	✓	B: CA Block	DS: 97.9
16	Yong <i>et al.</i> [74]	✓	✓	✗	E, D: QCBCT block	✗
17	Zhou <i>et al.</i> [75]	✓	✗	✓	E: Residual Conv. Model; B: Dilated Conv. Model; L: Hybrid	DS: 70.47
18	Gu <i>et al.</i> [113]	✗	✓	✓	D: CA; B: Spatial attention	DS: 90.83
Vascular						
19	Cai <i>et al.</i> [72]	✓	✓	✗	E,D: Batch Normalization	JI: 83.02
20	Claux <i>et al.</i> [63]	✗	✗	✓	B: Segmentation Block	DS: 78
21	Yi <i>et al.</i> [64]	✗	✗	✗	Training dataset added	DS/JI: 94.9 and 90.3
22	Liu <i>et al.</i> [65]	✓	✓	✓	E: Boundary refinement; D: Position attention; B: Channel attention	✗
23	Chen <i>et al.</i> [66]	✓	✓	✗	E: Dilated Conv.; D: Dilated Conv; H: No change	JI/DS: 0.9627 and 0.9743
24	Xu <i>et al.</i> [73]	✗	✓	✗	D: Post processing unit	DS: 83
25	Ding <i>et al.</i> [79]	✓	✗	✗	E: Multi-objective Optimization	✗
26	Zhao <i>et al.</i> [76]	✓	✗	✓	E: Residual Conv. Model; B: Dilated Conv. Model; L: Hybrid	✗

EC: Encoder change; DC: Decoder change; BgC: Bridge Network Change; BCE: Binary cross entropy; MCL: Multiple convolution layers; Conv: convolution; DAC: RMP: residual multi-kernel pooling; CA: Channel attention; E: Encoder; B: Bridge; D: Decoder.

with dropout [70, [76], [86], [95], [101], [102], [134], [138]; (D2) UNet++ type of change [130], [144], [154]; (D3) UNet+ + + (UNet 3+) Full scale deep supervision [157]; (D4) Output from decoders to make a loss function [104], [140]; (D5) fusion of the decoder outputs for scale adjustment [59, 107]; (D6) recurrent residual [118], [129], [138]; (D7) residual block [75], [84], [88], [105], [138], [150]; (D8) channel attention and scale attention block [65], [113]; (D9) transpose convolution [66], [88], [94], [95], [139]; (D10) squeeze excitation (SE) Network [103], [125]; (D11) cascade convolution [99]; (D12) addition of original image to each layer [100]; (D13) batch normalization [95], [106], [155]; (D14) inception block [97]; (D15) dense layer [87], [91], [122]; and (D16) convolution with feature maps [111], [115], [158]. A set of representative examples will be discussed in section VI.

C. SKIP CONNECTION AND ITS VARIATIONS

The skip connection is one of the most important components of the UNet architecture. This is primarily due to the transfer of image features from article encoder to decoder. The skip connection has taken many kinds of advances during the evolution of UNet architecture. We have categorized the variation in the skip connection of the UNet architecture by considering *nine* new variations shown in Table 3, namely (S1) direct skip without any addition [44], [46], [51], [76]; (S2) UNet++ with middle neurons are supported by the encoder layers [130], [144], [154]; (S3) UNet+ + + (UNet 3+) skip connection with full scale [157]; (S4) addition of long short-term memory network (LSTM) [159], recurrent neural network (RNN) [109], generative adversarial network (GAN), bidirectional long short-term memory network (BiLSTM), bidirectional recurrent neural network (BiRNN), bidirectional generative adversarial network (BiGAN) [74], [160]; (S5) skip connection between two cascaded UNet where skip of one is connected with skip of second and output of UNet first decoder goes in the skip of second UNet [81]; (S6) skip of first UNet into the skip of second UNet [89]; (S7) addition of the channel attention to improve the feature extraction along with atrous dense convolution block [65], [66], [71], [75], [82], [113], [119], [125], [126], [128], [129], [131], [132], [133], [134], [135], [139], [161]; (S8) squeeze-excitation (SE) network [125], [133]; and (S9) Res skip [150]. The skip connection offers the ability to interface the powerful classification paradigms such as LSTM, RNN, and GAN. It is during the skip connection framework that the concatenation phenomenon allows to interface the feature from the encoder along with bilinear interpolation of the previous layers. It has been observed that output of the skip connection leads to a loss function application.

D. BRIDGE NETWORK AND ITS VARIATIONS

The contextual to semantic features are passed ultimately through the bridge network. Fundamentally, the bridge network is nothing but a cascade of convolution. We have fundamentally categorized the batch normalization into *twelve*

types of variation, namely, (B1) serial cascades of convolutions [95]; (B2) convolutions with dropouts [102], [134]; (B3) dropout in bridge network [80], [134], [138]; (B4) cascade of convolutions in serial and parallel (DAC and RMP blocks) [108], [153]; (B5) bridge normalization [61], [95]; (B6) flatten block [69]; (B7) atrous spatial pyramid pooling [135]; (B8) transpose convolution [137]; (B9) patch convolution and transformer [66]; (B10) inception block [97]; (B11) dense layer [114], [122]; and (B12) quartent attention [82]. A set of representative examples will be discussed in section VI.

E. MISCELLANEOUS VARIATIONS IN UNET BY EXTERNAL ADDITIONS

The UNet architecture has been modified in some way which does not correspond to any of the above-mentioned main components. By improving the quality of feature extraction, these provide better results in image segmentation and classification. We have identified 19 such modifications and categorized them as miscellaneous UNet. The modifications were namely, (M1) UNet combined with CNN for feature extraction and Random Forest for ML classification [63], [124]; UNet-based lung segmentation + feature extraction using high resolution network (HRNet) + FCN (Softmax) [55], [63]; (M2) changes after the last decoder with Conv [54], [162]; (M3) cascade of two plain UNet for segmentation [53], [72], [73], [93], [148]; (M4) cascade of two 3D UNet [42], [53], [96], [114], [141]; (M5) patch input to the conventional CNN [98], [105], [121]; (M6) feedback system to improve the training [58]; (M7) fusion of parametric (active contour model) curves with UNet for COVID-19 lesion segmentation [60]; (M8) combination of different application [146], [151]; (M9) fusion of different classifiers [145]; (M10) linear combination [147]; (M11) UNet training model [64]; (M12) combination of fully convolutional net (FCN) and UNet [143]; (M13) hierarchically-fused multi-task learning (MTL) [83]; (M14) ZNet [85]; (M15) BRAVE-Net [110]; (M16) DiUNet [115]; (M17) T-Net [117]; (M18) RFARN [119]; and (M19) CondenseUNet [163]. A set of representative examples will be discussed in section VI.

F. LOSS FUNCTION VARIATIONS FOR UNET DEEP LEARNING MODELS

The loss function identified were of two types: (L1) fusion of cross-entropy (CE) and Dice similarity (DS) [56], [68], [69], [70], [74], [75], [79], [130], [145]; (L2) CE using the output of decoders [59], [104], [107], [110], [140], [152].

The loss function can be mathematically described as given in Eq. 1 if α_{BCE} represented the BCE-loss function, a_i represented the classifier's probability utilized in the AI model, x_i represented the input gold standard label 1, $(1-x_i)$ represented the gold standard label 0.

$$\alpha_{CE} = -[(x_i \times \log a_i) + (1 - x_i) \times \log(1 - a_i)] \quad (1)$$

Here \times represents the product of the two terms. The dice loss is named after the Dice-Sørensen coefficient, a statistic

developed in the 1940s to evaluate the similarity between two samples. When X is the input image and Y is the target or ground truth image, the Dice loss employed in this manuscript can be represented as given in Eq. 2.

$$DiceLoss = 1 - \frac{2|X \cap Y|}{|X| + |Y|} \quad (2)$$

G. UNDERSTANDING MAJOR BLOCKS AFFECTING FOR UNET MODIFICATION

The different fundamental blocks which were adapted for UNet modification were (Table 4): (1) residual block [75], [76], [78], [84], [88], [105], [129], [135], [138]; (2) classifier in encoder [145]; (3) Xception block [56], [88]; (4) dense layer block [68], [100], [102], [122], [142]; (5) recurrent residual block; (6) attention block [65], [66], [71], [75], [113], [125], [128], [129], [131], [132], [133], [134], [135], [139], [161]; (7) dropout layer [70], [76], [86], [95], [101], [102], [134], [138]; (8) dilated convolution [67], [76]; (9) transpose convolution [66], [88], [95], [137], [139]; (10) SE network [92], [103], [125], [133], [138], and (11) squeeze and excitation block [92], [103], [125], [133], [138].

The residual block (Figure 5 (a)) mainly consists of pile weight layers in which the convolution result of a layer was taken and summed to another deeper layer in the block. It provides a better feature extraction from the input images. The addition of classifiers in the encoder layer is a kind of modification. The different classifiers used were LSTM, GAN, RNN, bidirectional LSTM, and bidirectional RNN. Figure 5 (b) shows the LSTM block, which helps in dealing with the vanishing gradient problems that were encountered due to traditional RNN. Xception is a profound convolutional brain network engineering that includes depth-wise separable convolutions. It does not create any non-linearity and also provides better segmentation results. A translation of Xception modules (Figure 5 (c)) was introduced in convolutional brain networks just like an intermediate step in-between customary convolution and the depth-wise divisible convolution activity (a depth-wise convolution followed by a point-wise convolution). The dense layer block (Figure 5 (d)) for better feature extraction with feature map, batch normalization (BN), ReLU, and transition layer in it is another modification. It improves the parameter efficiency and easy to train.

The recurrent residual block addition is the next type of modification. It is used for generating the final output by combining the original input and output from second recurrent unit [129], [138]. It is added to obtain a better result for feature extraction (see Figure 6. (a)). The attention block addition is the change or modification to the UNet architecture [65], [66], [71], [75], [113], [125], [128], [129], [131], [132], [133], [134] [135], [139], [161] (Figure 6. (b)). The attention is of two types, namely, channel attention and spatial attention. It is added in the skip connection and sometimes in the encoder.

It is to handle the change in (a) position, (b) shape, (c) size, (c) scale, and (d) contrast in image segmentation. Dropout

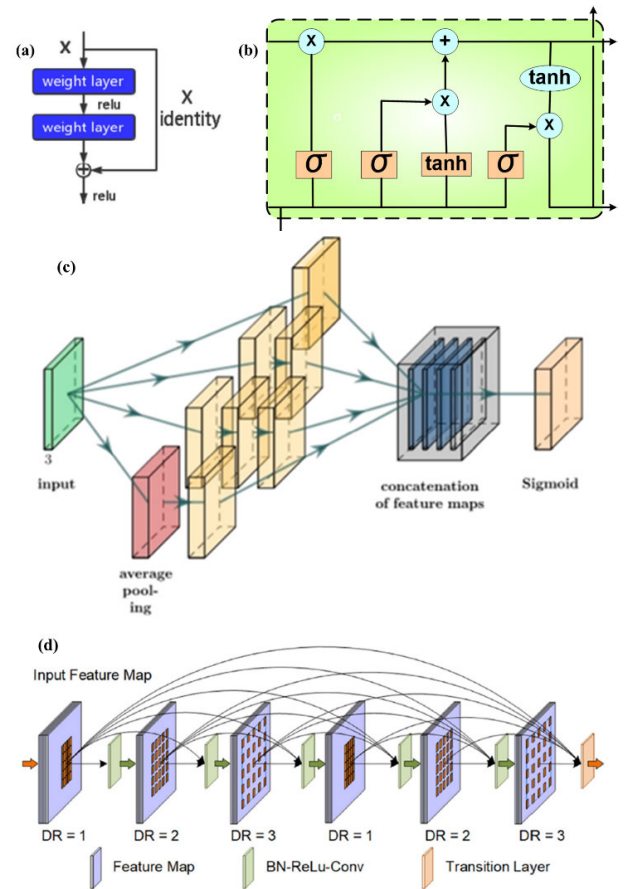


FIGURE 5. (a) Residual block [75], [76], [78], [84], [88], [105], [129], [135], [138] Copyright © 2018, IEEE; (b) Classifier in encoder [145]; (c) Xception block [56], [88] [112] Copyright © 2020, IEEE; and (d) Dense layer block [68], [100], [102], [122], [142]. (This figure was published in "Dilated densely connected U-Net with uncertainty focus loss for 3D ABUS mass segmentation., Cao, Xuyang, et al." Computer Methods and Programs in Biomedicine 209 (2021): 106313.)

layer addition to the UNet architecture is for further extraction by the mechanisms of dropping out the external noises from the features and enhancing the feature (Figure 6. (c)). The dilated convolution is done by expanding the kernel (input) through the process of insertion of holes in-between each element [67], [76] (Figure 6. (d)). It is the process of skipping pixel to accommodate a larger area for segmentation. It generally gets added to the encoder and decoder layers of the UNet architecture [113].

The Inception block being another kind of modification for UNet architecture that contains various convolutional and pooling layers stacked together thereby improving the results and diminishing calculation costs [164]. Initiation networks have improved gradually with more up-to-date and fresher variants and have outperformed different structure (Figure 7 (a)). The other modification is the transpose convolution [46], [64], [71], [113], [115], which is opposite of the convolution.

In the convolutional layer, a special operation named cross-correlation is used to obtain the output values, while for the

TABLE 3. UNet components and its variations.

SN	UNet Components	Variation in Components with References
1	Total Encoder Types, 23	E1 Conventional system (Ronneberger) [43-52, 90]
		E2 Cascade of convolutions [77, 91, 99, 116, 117]
		E3 Parallel Convolutions (Multiple Convolution Network) [57]
		E4 Convolution with dropout [70, 76, 86, 95, 101, 102, 134, 138];
		E5 Residual network [76, 78, 105, 129, 135, 138, 149-151]
		E6 Xception Encoder [56, 88, 112]
		E7 Encoder layers with independent inputs [104, 140]
		E8 Squeeze Excitation (SE) Network [92, 103, 138];
		E9 Pooling Types (Max Pooling, Global Average Pooling) [95]
		E10 Input image dimension change with changing filter (channels) [47, 74, 79, 99, 136, 152]
		E11 Input image dimension 2D to 3D [47, 74, 79, 99, 136, 152]
		E12 Cascaded UNets where encoder of second UNet becomes input from the first decoder [123]
		E13 Combination of exponential ReLU in Encoder [89]
		E14 Dilated convolution and activation function [67, 76]
		E15 Dense layer [68, 87, 91, 100, 102, 114, 122, 142]
		E16 Boundary Refinement [65]
		E17 Batch normalization (BN) [95, 106, 125, 137]
		E18 Patch convolution and transformer [66, 94, 100, 105]
		E19 UNet++ [144]
		E20 Addition of original image to each layer [100]
		E21 Inception Block [97, 102]
		E22 Ghost [118]
		E23 VGG 16 [156]
2	Total Decoder Types, 16	D1 Convolution with dropout [70, 76, 86, 95, 101, 102, 134, 138]
		D2 UNet++ [130, 144, 154]
		D3 UNet+++ [144];
		D4 Output from Decoders to make a loss function [104, 140];
		D5 Fusion of the Decoder outputs for scale adjustment [59, 107]
		D6 Recurrent residual [118, 129, 138]
		D7 Residual Block [75, 84, 88, 105, 138, 150]
		D8 Channel Attention and scale attention block [65, 113]
		D9 Transpose Convolution [66, 88, 94, 95, 139]
		D10 Squeeze Excitation (SE) Network [103, 125]
		D11 Cascade convolution [99]
		D12 Addition of original image to each layer [100]
		D13 Batch normalization (BN) [95, 106, 155]
		D14 Inception Block [97]
		D15 Dense layer [87, 91, 122]
		D16 Convolution with feature maps [111, 115, 158]
3	Total Skip Connection Types, 9	S1 Direct skip without any addition [44, 46, 51, 76];
		S2 UNet++ with middle neurons are supported by the encoder layers [130, 154]
		S3 UNet+++ where middle neurons are supported by the encoders and previous middle layers [144]
		S4 Addition of LSTM [159], RNN [109], GAN [160] [74], BiLSTM, BiRNN, BiGAN
		S5 Skip connection between two cascaded UNets where skip of one is connected with skip of second and output of UNet first decoder goes in the skip of second UNet [81].
		S6 Skip of first UNet into the skip of second UNet [89].
		S7 Addition of the channel attention to improve the feature extraction along with atrous dense convolution block [65, 66, 71, 75, 82, 113, 119, 125, 126, 128, 129, 131-135, 139, 161]
		S8 Squeeze Excitation (SE) Network [125, 133]
		S9 Res Skip [150]
4	Total Bridge Network Types, 12	B1 Serial cascades of convolutions [95]
		B2 Convolutions with Dropouts [102, 134]
		B3 Dropout in bridge network [80, 134, 138]
		B4 Cascade of convolutions in serial and parallel (DAC and RMP blocks) [108, 153]
		B5 Bridge Normalization [61, 95]
		B6 Flatten Block [69]
		B7 Atrous Spatial Pyramid Pooling [135]
		B8 Transpose Convolution [137]
		B9 Patch convolution and transformer [66]
		B10 Inception Block [97]
		B11 Dense layer [114, 122]
		B12 Quartent Attention [82]
5	Miscellaneous UNet Designs, 19	M1 UNet combined with CNN for feature extraction and Random Forest for ML classification [63, 124]; UNet-based Lung Segmentation + Feature Extraction using High Resolution Network (HRNet) + FCN (Softmax) [55, 63]
		M2 Changes after the last decoder with Conv [54, 162]
		M3 Cascade of two plain UNets for segmentation [53, 72, 73, 93, 148]

TABLE 3. (Continued.) UNet components and its variations.

		M4 Cascade of two 3D UNets [42, 53, 96, 114, 141]
		M5 Patch input to the conventional CNN [98, 105, 121]
		M6 Feedback system to improve the training [58]
		M7 Fusion of Parametric (active contour model) Curves with UNet for COVID-19 lesion segmentation [60]
		M8 Combination of different application [146]
		M9 Fusion of different classifiers [145]
		M10 Linear Combination [147]
		M11 UNet training model [64]
		M12 Combination of Fully convolutional net (FCN) and UNet [143]
		M13 Hierarchically-Fused MTL [83]
		M14 ZNet [85]
		M15 BRAVE-Net [110]
		M16 DilUNet [115]
		M17 T-Net [117]
		M18 RFARN [119]
		M19 CondenseUNet [163]
6	Loss Function types, 2	L1 Fusion of Cross-Entropy (CE) and Dice Similarity (DS) [56, 68-70, 74, 75, 79, 130, 145]; L2 CE using the output of decoders [59, 104, 107, 110, 140, 152]

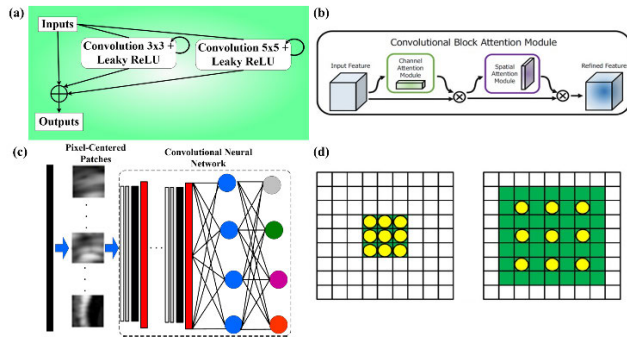


FIGURE 6. (a) Recurrent residual block [129], [138]; (b) Attention block [65], [66], [71], [75], [113], [125], [128], [129], [131], [132], [133], [134], [135], [139], [161]; (c) Dropout layer [70], [76], [86], [95], [101], [102], [134], [138]; (d) Dilated convolution [67], [76]. (This figure was published in Lung computed tomography image segmentation based on U-Net network fused with dilated convolution, Chen, K.B., et al., 2021. Computer Methods and Programs in Biomedicine, 207, p.106170.)

transpose convolution, the process operates in the reverse way (Figure 7 (b)). The block 2 represents the transpose convolution block which was applied three times by taking the output from block 1. It offers better segmentation results.

V. ADVANCED UNET TYPES

Due to challenges in the time complexity and large number of parameters in deep learning models, there has been recent advances which addresses these issues. We have characterized them as “advanced UNet types”. The three most important advanced UNets which is prominently dominated the UNet industry are Half-UNet, AM-UNet, and Efficient-UNet discussed in V.A, V.B, and V.C, respectively.

A. HALF-UNET

Half-UNet was invented by Lu et al. [165] which was flushed with three kid innovations, all geared towards a common

TABLE 4. Blocks adapted for UNet modification.

SN	Popular Fundamental Block	References
1	Residual Block	[75, 76, 78, 84, 88, 105, 129, 135, 138]
2	Inception Block	[97, 102]
3	Xception Block	[56, 88]
4	Dense Layer Block	[68, 100, 102, 122, 142]
5	Classifier in Encoder	[145]
6	Dropout Layer	[70, 76, 86, 95, 101, 102, 134, 138]
7	Dilated Convolution	[67, 76]
8	Recurrent Residual Block	[129, 138]
9	Transpose Convolution	[66, 88, 95, 137, 139]
10	Attention Block	[65, 66, 71, 75, 113, 125, 128, 129, 131-135, 139, 161]
11	Squeeze and Excitation Block	[92, 103, 125, 133, 138]

spirit of reducing complexity while retaining the performance of the feature extraction compared to original UNet. These three ideas were conceptually labeled as (i) unification of channels *i.e.*, number of channels in each layer should be same. Further, removal of the decoders to a single bar decoder *i.e.*, optimization of the architecture ensuring performance approximately equivalent to cUNet; (ii) full-scale feature fusion that consists of different scaled features maps obtained from contractual path (encoders), which was fused using an “addition operation” after upsampling, and (iii) Ghost model for reduction in complexity of convolution. The spirit of unification of channel was felt after looking at the complexity of UNet, UNet3+ models. In these models, the number of channels were doubled after every down-sampling step. In UNet3+, because of an unequal number of channels 3 × 3 convolution operation is added after every max pool operation to unify the channel numbers, hence

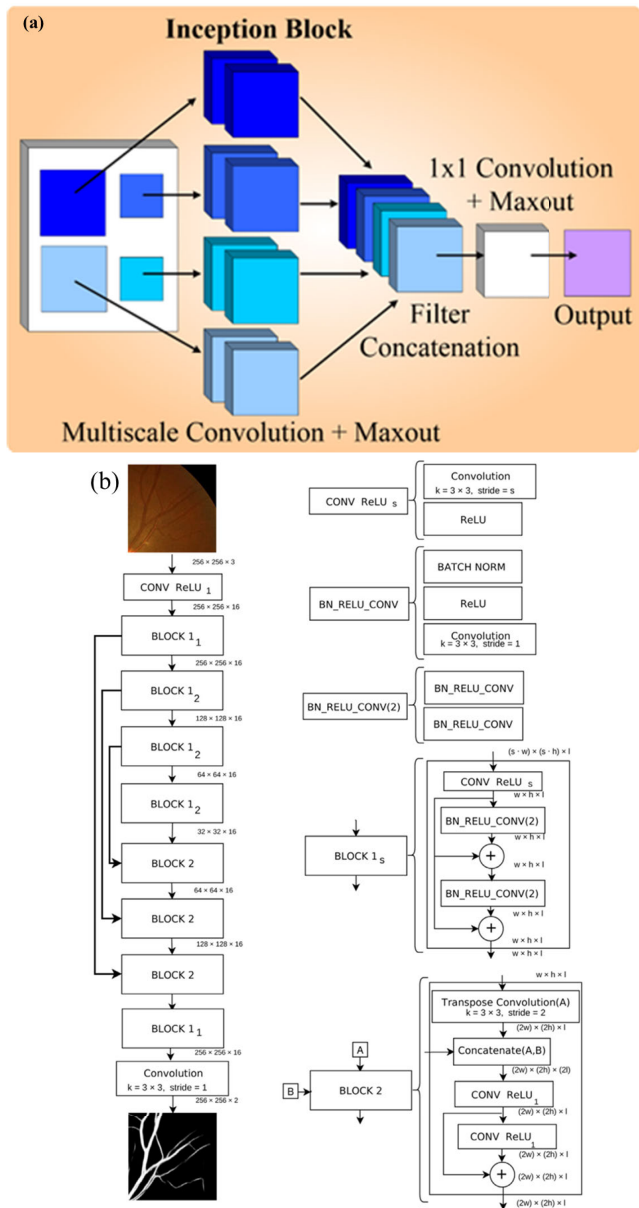


FIGURE 7. (a) Inception block [97], [102]. (b) Transpose convolution block [66], [88], [95], [137], [139]. (This figure was published in A new deep learning method for blood vessel segmentation in retinal images based on convolutional kernels and modified U-Net model, Gegundez-Arias et al., Computer Methods Programs in Biomedicine, 2021. 205: p. 106081.)

increasing the required number of parameters and Floating-Point Operations per Second (FLOPs). On the contrary, in Half-UNet, the number of the channel of all feature maps is unified, which reduces the number of filters in the convolution operation and contributes feature fusion on the decoder. This is because the decoder does not need 3 × 3 convolution. This can be seen in Figure 8, where the decoder layers are removed by a single stacked decoder, which received the input from the bottleneck and subsequently inputs via skip connection. This reduces the complexity in Half-UNet. The second important feature of Half-UNet was the Full-Scale

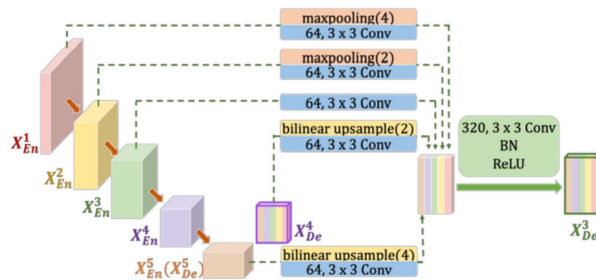


FIGURE 8. Full-scale aggregated feature map of 3rd decoder layer – concept used in the design of Half UNet [165].

Feature Fusion. Note that in the original UNet and UNet3+ use concatenation operation for feature fusion. Concatenation operation is a great choice as it provides better results but it also takes more memory and time and hence complexity increases. He et al. [166] proposed a ResNet, which uses addition operation as a feature fusion method. In this operation, the authors perform identity mapping and add their outputs to the outputs of the stacked layer. This operation does not increase the dimension of an image but increases the information for each dimension. This operation does not increase the number of parameters, as a result, does not increase complexity. This concept is used in Half-UNet and is shown in Figure 9. It shows the \oplus sign which signifies the merger of the skip connections and fused in a single decoder. The third architectural feature of Half-UNet was Ghost Module design (Figure 10 (a) and Figure 10 (b)). The whole idea behind this was the reduction of convolution complexity (Figure 10(a)). We already know that deep convolutional neural networks [166], [167], [168] often consist of many convolutions that results in massive computational costs. Although recent works such as MobileNet [169], [170] and ShuffleNet [171] have introduced depth-wise convolution or shuffle operation to build efficient CNNs using smaller convolution filters (floating number operations), the remaining 1 × 1 convolution layers would still occupy considerable memory and FLOPs. The idea behind the Ghost module is to generate more feature maps while using cheap operations, i.e., a smaller number of operations. The parameters and FLOPs can be calculated during convolution operation:

$$\text{params} = (k^2 * \text{Cin} + 1) * \text{Cout} \quad (3)$$

$$\text{FLOPs} = 2 * k^2 * \text{Cin} * \text{Cout} * \text{Hout} * \text{Wout} \quad (4)$$

where k is kernel size, Cin is input size, Cout is output size, Hout is the height of the output maps and Wout is the width of output maps, and * represents the arithmetic product. Han et al. [172] proposed a Ghost module to generate more feature maps while using cheap operations. In Ghost module ($s = 2$, s represents the reciprocal of the proportion of intrinsic feature map), half of the feature map is generated by convolution operation and the other half of the feature map is generated by depth-wise separable convolution and finally concatenated to form the output of the same dimension

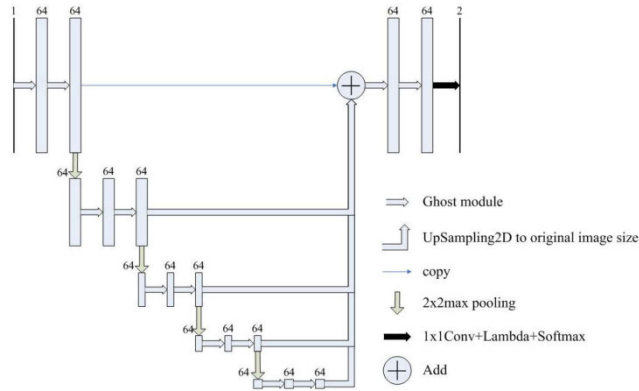


FIGURE 9. Half-UNet architecture [165].

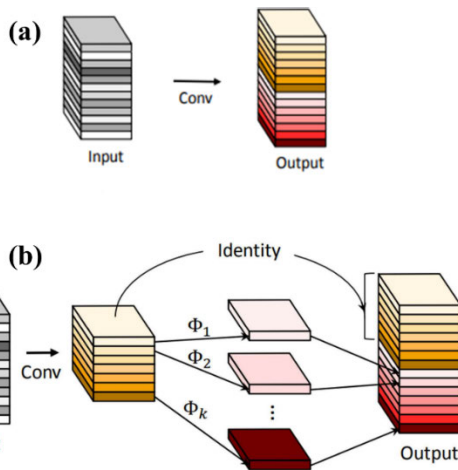


FIGURE 10. (a) Convolution module; (b) Ghost module [172].

as input.

$$\text{params} = \left(k^2 * (\text{Cin} + 1) + 2 \right) * \frac{\text{Cout}}{2} \quad (5)$$

$$\text{FLOPS} = 2 * k^2 * (\text{Cin} + 1) * \frac{\text{Cout}}{2} * \text{Hout} * \text{Wout} \quad (6)$$

For example, if the image size is 128×128 , 3×3 convolution, and both input and output channels are 64 then the required number of parameters and FLOPS is 36.92K and 12.08G while using the Ghost module required a number of parameters and FLOPS are 18.78K and 0.61G only. Therefore, the Ghost module is used in Half-UNet.

Advantage and Application of Half-UNet: We already know from previous discussions that the variants of UNet showed to improve model performance without affecting the U-shape model architecture. In Half-UNet, the encoder and decoder are simplified. Half-UNet took advantage of the unification of channel numbers, full-scale feature fusion, and Ghost module. Authors compared the results of Half-UNet with UNet and its variants and obtained similar segmentation accuracy results but parameters and FLOPS were reduced by 98.6% and 81.8% respectively as compared to UNet. The authors compared the results of Half-UNet with

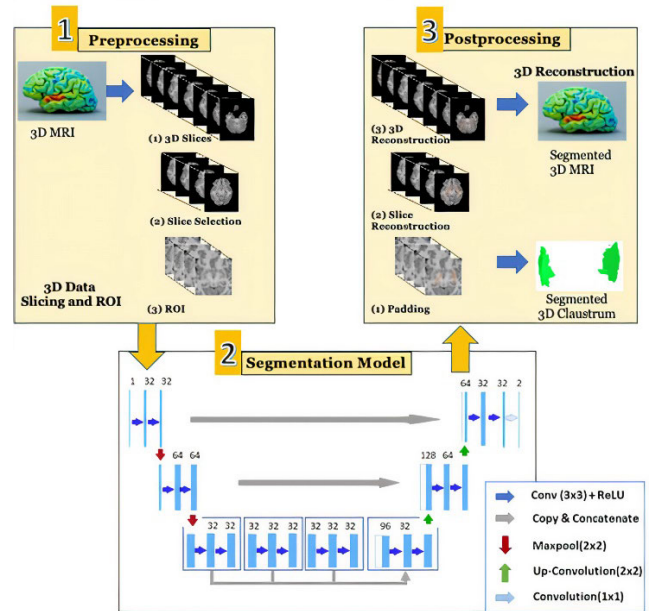


FIGURE 11. AM-UNet [173]. (Reproduced with permission.)

UNet and its variants across different medical image segmentation like mammography segmentation (*non-vascular*), lung nodule segmentation in computed tomography image (*non-vascular*), and left ventricle MRI image segmentation (*non-vascular*).

B. AM-UNET

This class of advanced UNet was again to simply the complexity of UNet paradigm. AM-UNet is a lightweight and scalable solution that has achieved state-of-art accuracy. It reduces the complexity, time required for segmentation. Albishri et al. [173], [174] proposed an automatic optimized UNet-based 3D segmentation model named as automated mini-UNet (AM-UNet), Figure 11, designed as an end-to-end process for human brain claustrum (CL) segmentation. AM-UNet was adapted for CL segmentation since it was challenging due to its thin, sheet-like structure, heterogeneity of its image modalities and formats, imperfect labels, and data imbalance. In AM-UNet authors reduced the model size to half by removing the last two layers of the original UNet (five vs. three) and expanding the bottleneck layer of the segmentation model (Figure 11). The system consisted of three steps: preprocessing, segmentation, and post-processing. In preprocessing step, the 3D-MRI volumes are converted into a series of 2D slices, and regions-of-interest is created. In the second step, the preprocessing of region-of-interest selection is done from the 2D selected slices and segmentation of CL was conducted. In the third step data augmentation and normalization are applied to images to 3-D reconstruct. The postprocessing step was used to ensure high prediction accuracy for 3D claustrum segmentation.

Applications: The authors have predicted that AM-UNet is very useful in vascular i.e., for the brain, cardiology, and

non-vascular i.e. for lung, liver, and kidney medical image segmentation because it is capable to segment the image even if it is very thin, heterogeneous in nature, imperfect labels, and data imbalance.

C. EFFICIENT-UNET

Another advanced UNet where encoders were drastically altered to improve the computation burden was Efficient (Eff)-UNet. The birth of this innovation came from the spirit that when the Indian road and driving environment conditions are not structured, then such segmentation paradigms are well suited. They are far superior to semantic scenes using conventional models of DL and CNN.

It was Baheti et al. [175] who proposed an architecture called Efficient (Eff)-UNet that combined the compound scaled Eff-Net as the encoder for feature extraction and decoder having same function as original cUNet for reconstructing the fine-grained segmentation map. The combination between the high-level feature information as well as low-level spatial information was important for the precise segmentation.

Tan et al. [176] proposed a novel compound scaling method that uniformly scales the network depth, width, and resolution for improved performance based on a fixed set of scaling factors. A new architecture called EfficientNetB0 was designed initially and scaled up to generate a family of Eff-Net by the compound scaling method. There are eight variants of the EfficientNets, namely EfficientNetB0 to EfficientNetB7. Scaling the network systematically improves model performance balancing all compound coefficients of the architecture width, depth, and image resolution. The basic building block of the Eff-Net architecture was mobile inverted bottleneck convolution (MBCnv) [170] with squeeze and excitation (SE) optimization, shown in Figure 12. The shortcut connections between the thin bottleneck layers are the shortcut connections in MBCnv are based on an inverted residual structure. Lightweight depth wise convolutions are used in the intermediate expansion layer as a source of non-linearity to filter features.

The best-performing model EfficientNetB7 outperforms other state-of-art CNNs in terms of accuracy using ImageNet. It also has $8.4\times$ smaller and $6.1\times$ faster than the best existing CNN [176]. The network architecture of EfficientNetB7 is shown in Figure 13. It can be divided into seven blocks, which were based on filter size, striding, and the number of channels. The authors used EfficientNetB5, and EfficientNetB7 as an encoder with UNet decoder and achieved the best performance with EfficientNetB7. The authors proposed to use Efficient-Net as an encoder in the contracting path instead of a conventional set of convolution layers. The decoder module is similar to the original UNet. The Eff-UNet showed in Figure 14. The number of levels, resolution, and number of channels of each feature map, and the detailed architecture of blocks in the encoder can be found in Figure 13.

Advantage and Application of Efficient-UNet: The main advantage of Eff-UNet is its ability to offer strong semantic

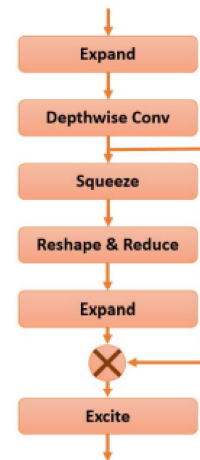


FIGURE 12. Squeeze and excite model [170] copyright © 2020, IEEE.

segmentations in an unstructured environment. Both vascular and non-vascular medical images are sometimes unstructured so Eff-UNet is useful in both cases.

VI. UNDERSTANDING VASCULAR AND NON-VASCULAR APPLICATIONS

One of the innovations of this study is to compare and contrast UNet architecture in vascular vs. non-vascular applications.

We have attempted this comparison in four different UNet classes (sUNet, acUNet, eUNet, and hUNet). Further, this section also presents the similarities and differences between the vascular vs. non-vascular architectures. All the above analysis is discussed in graphical representation format. Sections VI.A–VI.D discuss vascular vs. non-vascular architectures. Section VI.E presents the UNet characteristics for vascular vs. non-vascular applications. Section VI.F presents the key for segmentation challenges and architecture solutions for vascular and non-vascular paradigm. Finally, the section concludes with similarities and differences between vascular and non-vascular architectures.

A. SUNET ARCHITECTURE

1) NON-VASCULAR

The sUNet architecture is created for obtaining a better result of segmentation. The sUNet architecture for the non-vascular paradigm is displayed by Pezzano et al. [57] (Figure 15 (a)). There is an addition of multiple convolution block (MCL) along with max pooling layer, which is a modification in the encoder layer of the UNet system (shown in light blue color). It has four layers in it, of which three is mainly for convolution of the input image, while in the fourth layer is copied by using the identity function. Finally, all the four layers are concatenated (represented as “cat”) and finally up-sampled (represented as “up”) and convoluted one time (represented as “conv”) (Figure 15 (a)). The filters are increased to double in each layer. The key factors of this architecture and study are: (i) use of loss function with a parameter

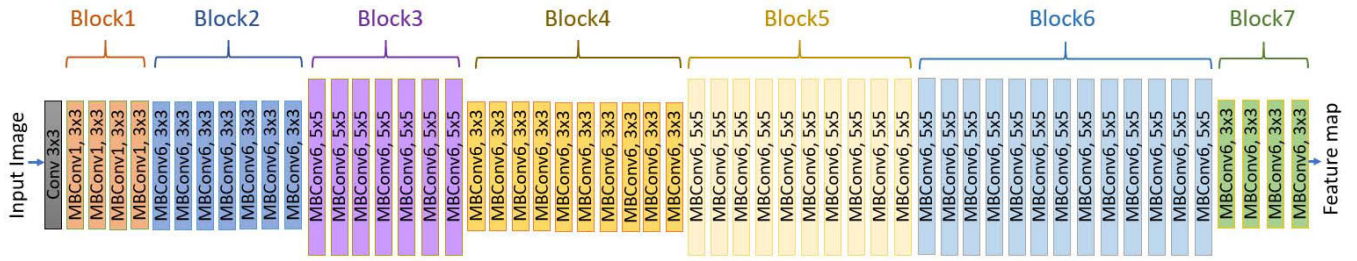


FIGURE 13. Architecture of EfficientNetB7 with MBConv as basic building blocks. The overall architecture can be divided into seven blocks which are shown in different colors. The basic building block of the network is MBConv (mobile inverted bottleneck convolution). Each MBConvX block is shown with the corresponding filter size and the X = 1 and X = 6 denote the standard ReLU and ReLU6 activation function respectively [175] Copyright © 2020, IEEE.

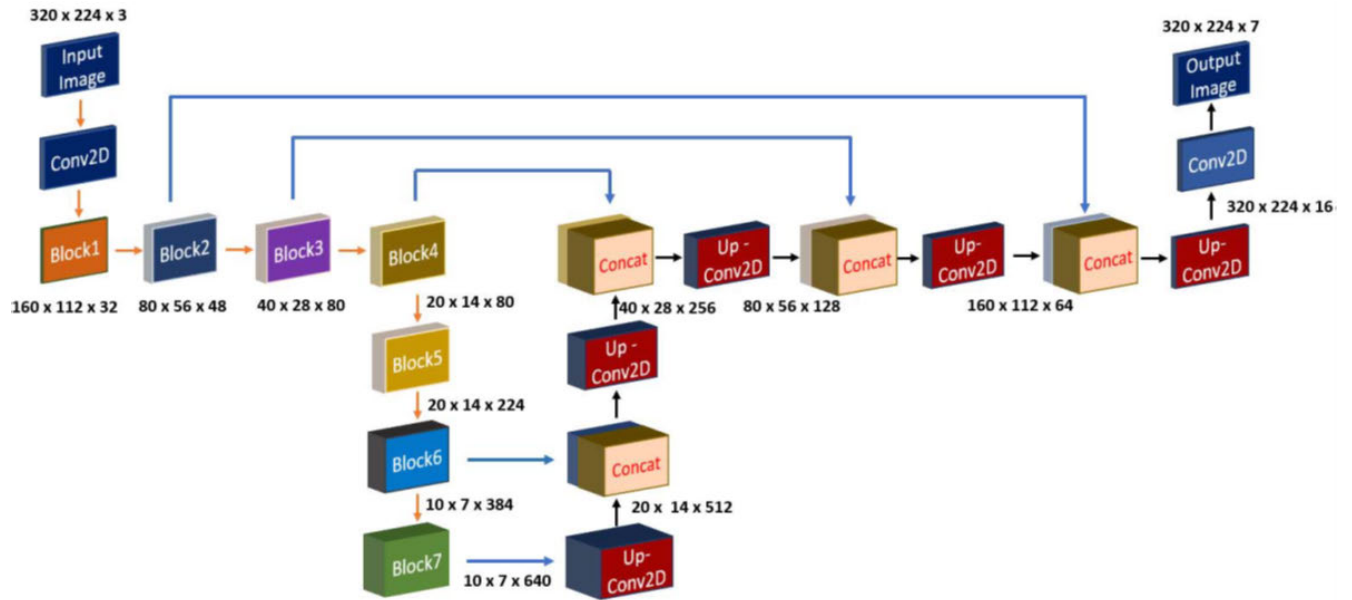


FIGURE 14. Architecture of proposed Eff-UNet with EfficientNetB7 framework for semantic segmentation. The decoder consists of a sequence of Upconvolution and Concatenation layers to obtain the segmentation map [175] Copyright © 2020, IEEE.

for maximizing sensitivity; (ii) addition of MCL; (iii) a mask calculation formula used for refining the input by removing the unitary values only; (iv) post-processing procedure used for reducing false positives and increase specificity; (v) two additional levels of depth of the network; and (vi) an extensive validation.

2) VASCULAR

The sUNet architecture for the retinal-based vascular application is described in Figure 15 (b). Chen et al. [66] has introduced patches convolution attention-based transformer UNet (PCAT-UNet) architecture. This architecture has PCAT block (Figure 15 (c)) in the encoder for local feature extraction along with the *feature grouping attention modules* (FGAM) (Figure 15 (d)) basically for global information extraction for getting more detailed feature maps of multiscale characteristics. Note that in the encoder, the size of the image decreases by half while in the decoder the size the image increases by twice. This architecture helps in achieving better

results, improves sensitivity and performance. It also involves attention between different patches and pixels, which in turns reduces the calculation and increases input resolution. The encoder extracts spatial and semantic information by the process of down sampling. The dropout block is added that suppress over-fitting during training. Overall, the architecture improves segmentation sensitivity and has a good segmentation performance.

B. AC-UNET ARCHITECTURE

1) NON-VASCULAR

The acUNet architecture is basically the addition of attention channel block as a fundamental block into any of the parts such as encoder, decoder, and skip connection. It is used in a variety of applications, including liver [71], tumor [71], lung [50], and neuron segmentation [177]. Generally, it is in the skip connection to obtain a better transfer of the feature extracted in the encoder to the decoder layer. Figure 16 (a) shows the fundamental architecture of the acUNet.

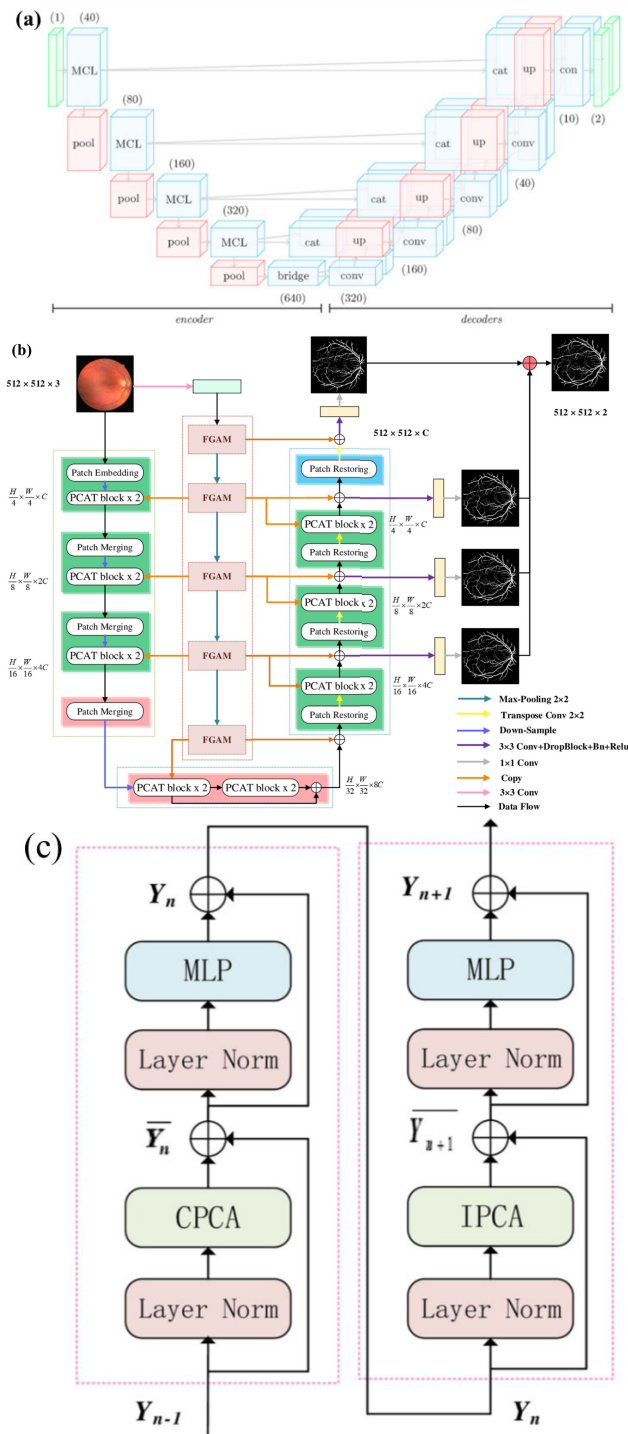


FIGURE 15. (a) sUNet architecture for non-vascular [57] (This figure was published in CoLe-CNN+: Context learning-Convolutional neural network for COVID-19-Ground-Glass-Opacities detection and segmentation, Pezzano, G et al. Computers in Biology Medicine, 2021. 136: p. 104689); (b) vascular [66] applications; (c) Two consecutive PCAT blocks. CPCA and IPCA are multihead self-attention modules with cross and inner patching configurations, respectively [66]; (d) Feature grouping attention module (FGAM) block [66].

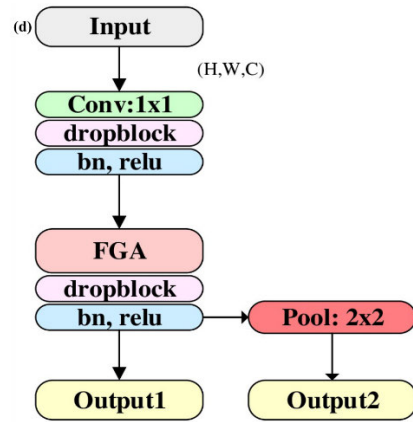


FIGURE 15. (Continued.) (a) sUNet architecture for non-vascular [57] (This figure was published in CoLe-CNN+: Context learning-Convolutional neural network for COVID-19-Ground-Glass-Opacities detection and segmentation, Pezzano, G et al. Computers in Biology Medicine, 2021. 136: p. 104689); (b) vascular [66] applications; (c) Two consecutive PCAT blocks. CPCA and IPCA are multihead self-attention modules with cross and inner patching configurations, respectively [66]; (d) Feature grouping attention module (FGAM) block [66].

Wang et al. [127] have added a convolution block attention module (CBAM) into the architecture (light blue color). The addition was made after each convolution layer and up sampling layer. It provides a better segmentation effect. The feature graphs were generated at the last layer and then maximized, average pooled, for obtaining spatial context descriptors. These descriptors were made to enter into the shared network called *multi-layer perceptron* (MLP) and the final eigenvectors are merged by using a summation process. The “Res connect” (depicted by solid lines) called as jump connection is used in each convolution layer and upper sampling layer (for the same dimensions) that provides better segmentation results (Figure 16 (a)).

2) VASCULAR

The acUNet architecture (Figure 16 (b)), the self-attention mechanism in CNN-Transfer hybrid network was implemented by Shen et al. [133]. It helps the system to learn the correlation between any two pixel-wise feature maps. Also, the *residual attention block* (bottom left) was constructed to improve the process of feature extraction. The third block added was the squeeze-excitation (SE) block for constructing a more efficient multi-head attention process by focusing on effective weights and neglecting invalid weights of the attention heads. This process is carried out by the SE block in the SE transformers. The SE transformer is the length of value vectors in the transformer layers. The SE transformer decreases the weights of weak correlation embedding vectors massively. It helps in distinguishing the strong and weak correlation vectors, and hence helps in focusing on vascular

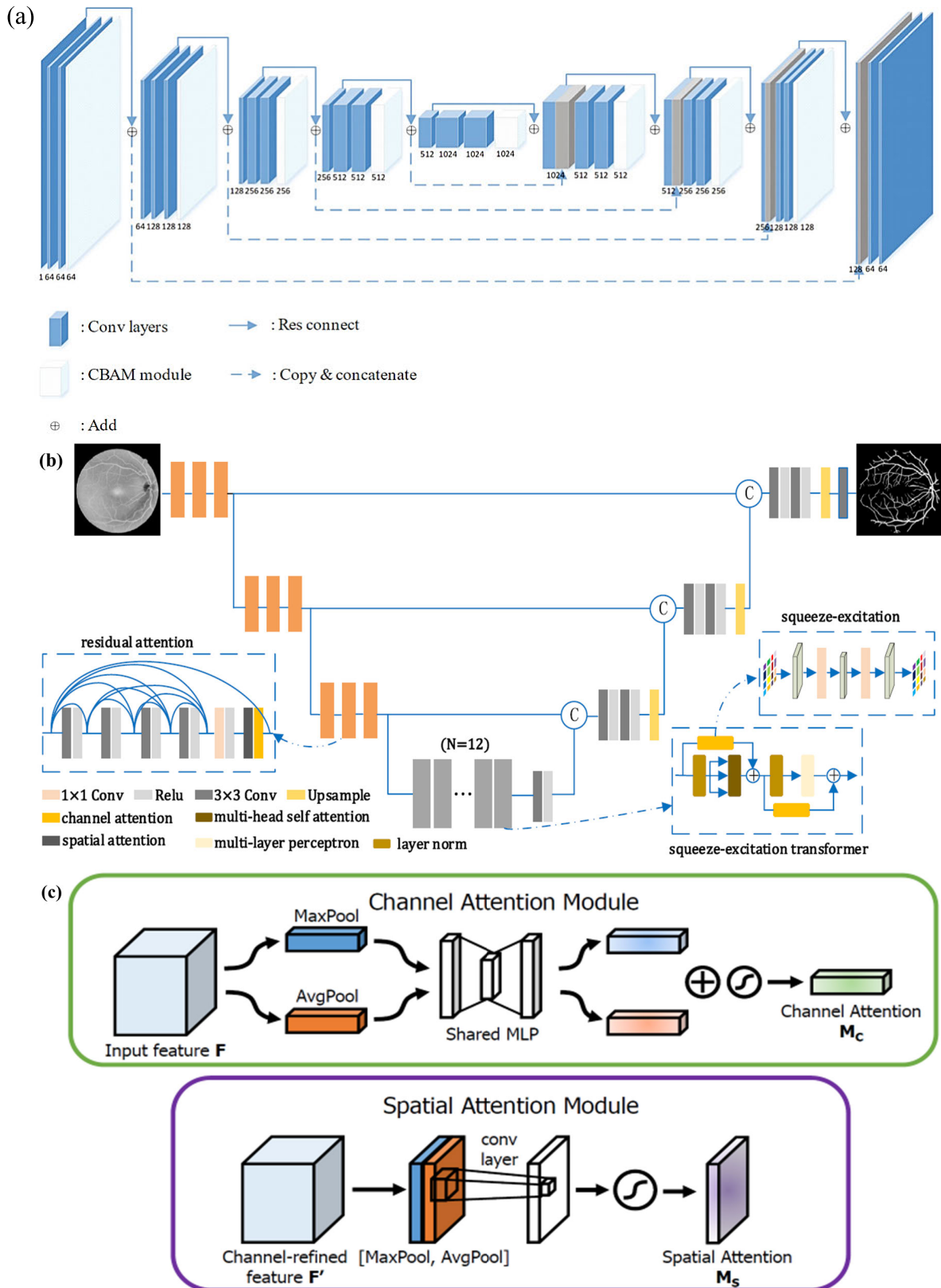


FIGURE 16. acUNet architecture. (a) Non-vascular using Resconnect [127] (This figure was published in Hybrid dilation and attention residual U-Net for medical image segmentation, Wang, Z. et al. Computers in Biology Medicine, 2021. 134: p. 104449); (b) UNet-based vascular using residual attention and squeeze-excitation transformer [133] (This figure was published in Self-Attentional Microvessel Segmentation via Squeeze-Excitation Transformer Unet, Shen, X. et al. Computerized Medical Imaging Graphics, 2022: p. 102055); (c) Channel block attention module and spatial block attention module [140].

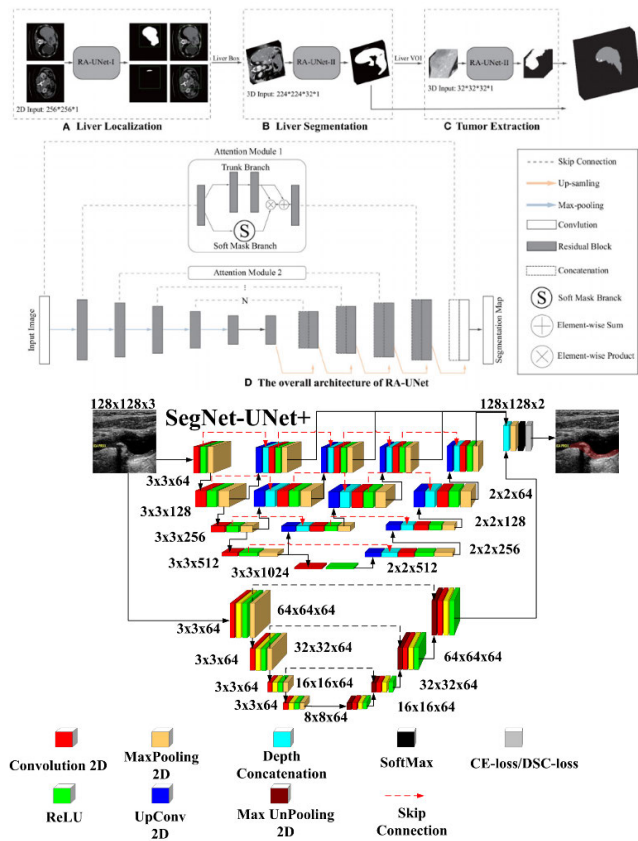


FIGURE 17. Top: hUNet architecture for non-vascular [131]; Bottom: AtheroEdge™ 3.0 for vascular [141] applications (This figure was published in Hybrid deep learning segmentation models for atherosclerotic plaque in internal carotid artery B-mode ultrasound, Jain, P.K., Computers in Biology Medicine, 2021. 136: p. 104721.)

connectivity image patches (Figure 16 (b)). The detailed structure of the convolution block attention module (CBAM) in shown in (Figure 16 (c)).

C. H-UNET ARCHITECTURE

1) NON-VASCULAR

The hUNet architecture involves liver [131] and brain tumor segmentation [131] and has two UNet types. For the non-vascular domain, the architecture shown here has two attention module, namely attention module 1 and attention modules 2 (Figure 17 (top)) [131], labelled as RA-UNet. It was used for liver and brain tumor [131] for segmentation map generation.

2) VASCULAR

The hUNet for the vascular paradigm uses SegNet-UNet+, which is the combination of SegNet and UNet+ (Figure 17 (bottom)) [53], [141], and VGG-UNet [178] and ResNet-UNet [179]. The same input images were given to SegNet and UNet+ separately and the outputs were obtained. Finally, the outputs from both UNets were merged and supplied to the SoftMax layer of the overall system.

Such a system has application for the cardiovascular field such as carotid segmentation for carotid ultrasound. Recently, a non-UNet based segmentation paradigm was attempted using an encoder-decoder combination [98], [180]. There have been non-AI based methods, so-called conventional strategies based on the scale-space paradigm [181], [182], [183], [184].

D. E-UNET ARCHITECTURE

1) NON-VASCULAR

The eUNet architecture in the non-vascular stands for ensemble UNet architecture. It combines two different UNet types, two processes, and more than one classifier. Here, the eUNet non-vascular paradigm in Figure 18 (top) [146] shows different applications like kidney segmentation and renal mass localization. Two UNets were used, first for kidney segmentation for training and the second for renal mass localization or identification (Figure 18 (top)).

2) VASCULAR

The eUNet vascular paradigm uses carotid images as the input. UNet++ was used eight different backbones for segmentation of the carotid artery. Eight different segmentation maps were generated from each of the backbones of UNet++. These maps were fused and finally output was obtained after final segmentation. At last, the total plaque area (TPA) was evaluated (Figure 18 (bottom)) [144].

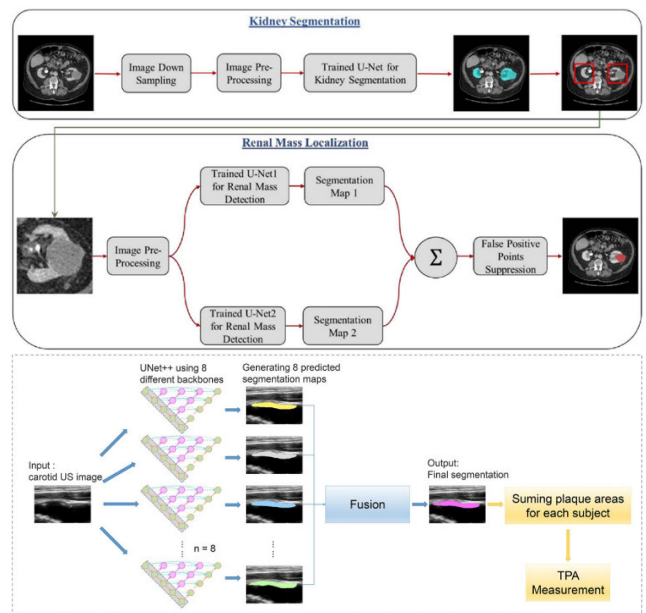


FIGURE 18. Top: eUNet architecture for non-vascular [146]; Bottom: vascular [144] applications Copyright © 2021, IEEE.

E. VASCULAR VS. NON-VASCULAR UNET CHARACTERISTICS

1) UNET FOR SEVERAL FIELD OF VIEW APPLICATIONS

The UNet architecture can be divided into application-based classes (i) vascular; and (ii) non-vascular. Vascular having

TABLE 5. Vascular and non-vascular-based UNet characteristics.

SN	Attributes	Vascular	Non-vascular
	References	[43, 46-49, 53, 63-66, 72, 73, 76, 79, 95-112, 114-122, 125, 126, 133-141, 143, 144]	[42, 44, 45, 50-52, 54-62, 67-71, 74, 75, 77, 78, 80-94, 113, 123, 124, 127-132, 142, 145-148, 153, 154, 161]
A1	TPR	58-630	50-1307
A2	FH	✓	✓
A3	RFT	OBBM, LBBM, CUSIP	OBBM, LBBM, HT, CS
A4	IM	Image	Point, Image
A5	MC	✓	✓
A6	FOV	F1	F2
A7	UNet CIT	cUNet, sUNet, acUNet	cUNet, sUNet, acUNet, hUNet, eUNet
A8	EnL	4 - 5	4 - 13
A9	DcL	4 - 5	4 - 13
A10	ConvT	ReLU	ReLU
A11	LossT	CE, Dice, Soft Dice	Cross-Entropy, Dice, Hybrid
A12	Optm	Adam, SDG	Adam
A13	BgT	Skip Connection	Skip Connection
A14	# PE	11	9
A15	SEN	✓	✓
A16	SPEC	✓	✓
A17	ACC	✓	✓
A18	PREC	✓	✓
A19	F1S	✓	✓
A20	PV	✓	✓
A21	DCS	✓	✓
A22	JI	✓	✓
A23	MCC	✓	✓
A24	PPV	✓	x
A25	HDS	✓	x
A26	StA	✓	✓
A27	PwA	✓	✓
A28	Sci.V	✓	✓
A29	Bm	✓	✓
A30	PTT	x	✓
A31	KWT	x	✓
A32	FDA	x	x
A33	CS	✓	x

TP*: Total patients range (cUNet: 20-1171, sUNet: 50-1302, acUNet: 58-500); RFT: Types of Risk Factors; HT: Histological types; CS: Clinical stages; IM: Imaging Modality; MC: Multicenter; FOV: Field of view; F1: cardiology, carotid, ophthalmology, neurology, pulmonary; F2: pulmonary, immunology (ILD), Immunology (COVID-19), urology, neurology, neurology (BTS), orthopedic, gastroenterology, dental; EL: Encoder layer; DL: Decoder layer; ConvT: Convolution type; LossT: Loss function type; CE: Cross-Entropy; Optm: Optimizer; BgT: Bridge network type; SC: Skip connection; UT: UNet types; SEN: Sensitivity; SPE: Specificity; A: Accuracy; PRE: Precision; F1S: F1 Score; PV: p -value; DS: Dice Similarity; JI: Jaccard index; MCC: Mathew's correlation coefficient; PPV: Positive predictive value; HDS: Hausdorff distance-surface; StA: Statistical analysis; PwA: Power analysis; SciVal: Scientific validation; PTT: Paired T-test; KWT: Kruskal-Wallis test; Bm: Benchmarking; FDA: Food and Drug Administration; CS: Clinical setting; UNet CIT: UNet class type.

the field of view (FoV) of cardiology (includes coronary and carotid) [53], [68], [69], [70], [71], [74], [75], [113], [131], [141], [142], [143], [185], ophthalmology [66], vascular neurology [79], and vascular pulmonary, while non-vascular FoV includes pulmonary [73], immunology (ILD or COVID-19) [82], urology [62], cancer-neurology [45] such as brain tumor segmentation, orthopedic [154], gastroenterology [71], [130], and dental [44]. Table 5 describes the vascular and non-vascular-based UNet characteristics spanned using 33 UNet attributes using different UNet architectures. The attributes belong to the following clusters (i) C1: demographics, risk factors, and field-of-view, (ii) C2: UNet architecture components, (iii) C3: number of UNet types on each of the five classes, (iv) C4: UNet performance, (v) C5: statistical tests, (vi) C6: benchmarking, (vii) C7: clinical analysis. It was observed in the Table 5 that the total patient range was high for the nonvascular paradigm. The histological types and clinical stages were used as risk factors only in nonvascular cases. Point data was used along with image data for the

nonvascular [42], [44], [45], [50], [51], [52], [53], [54], [55], [56], [57], [58], [59], [60], [61], [62], [63], [64], [65], [66], [67], [68], [69], [70], [71], [72], [73], [74], [75], [76], [77], [78], [79], [80], [81], [82], [83], [84], [85], [86], [87], [89], [90], [91], [92], [93], [94], [95], [96], [97], [98], [99], [100], [101], [102], [103], [104], [105], [106], [107], [108], [109], [110], [111], [112], [113], [114], [115], [116], [117], [118], [119], [120], [121], [122], [123], [124], [125], [126], [127], [128], [129], [130], [131], [132], [133], [134], [135], [136], [137], [138], [139], [140], [141], [142], [143], [144], [145], [146], [147], [148], [153], [154], [161] while only image data was used for vascular application [43], [46], [47], [48], [49], [53], [63], [64], [65], [66], [72], [73], [76], [79], [95], [96], [97], [98], [99], [100], [101], [102], [103], [104], [105], [106], [107], [108], [109], [110], [111], [112], [114], [115], [116], [117], [118], [119], [120], [121], [122], [125], [126], [133], [134], [135], [136], [137], [138], [139], [140], [141], [143], [144]. More types of performance parameter were applied for the vascular [43], [46], [47], [48], [49], [53], [63], [64],

[65], [66], [72], [73], [76], [79], [95], [96], [97], [98], [99], [100], [101], [102], [103], [104], [105], [106], [107], [108], [109], [110], [111], [112], [114], [115], [116], [117], [118], [119], [120], [121], [122], [125], [126], [133], [134], [135], [136], [137], [138], [139], [140], [141], [143], [144] when compared to nonvascular [42], [44], [45], [50], [51], [52], [54], [55], [56], [57], [58], [59], [60], [61], [62], [67], [68], [69], [70], [71], [74], [75], [77], [78], [80], [81], [82], [83], [84], [85], [86], [87], [88], [89], [90], [91], [92], [93], [94], [113], [123], [124], [127], [128], [129], [130], [131], [132], [142], [145], [146], [147], [148], [153], [154], [161]. The UNet based paradigm was implied for the clinical settings for the vascular application, while it is lacking for the non-vascular applications. Similar traits for the vascular and non-vascular were convolution type i.e., ReLU, loss function types used (CE, DICE, Soft DICE, hybrid), optimization techniques (Adam, SGD) and bridge network types (skip connection). The PE parameters common for both vascular and non-vascular were sensitivity, specificity, accuracy, precision, F1 score, p -value, Dice similarity, Jaccard index, Mathew's correlation coefficient, statistical analysis, power analysis, and scientific validation.

2) VASCULAR UNET DESIGNS CHARACTERISTICS

David et al. [122] designed a UNet system where the authors used different scaled image patches for each contractual layer as input. The idea was to learn more multiscale data. To obtain more spatial features, the authors used dense blocks. The color retinal images were first preprocessed to create enhanced grey images. The image patches around the vessel pixels were then retrieved and reutilized for UNet architecture improvement. According to Du et al. [102], extracted features from an input image for inception multiscale convolution and dense block convolution, respectively, and then fused these features, which were then used in the subsequent network. The inception network enhanced the ability to extract features of the thin vessels. The DenseNet was introduced to enhance the reuse of extracted features through dense connectivity. It effectively reduced the gradient vanishing problem, enhanced the feature transfer, and reduced the loss of feature information. In another vascular network, Guo et al. [139] used structure dropout convolution to avoid overfitting problems, and spatial attention (SA-UNet). The spatial attention module (SAM) was introduced in the bottleneck as a part of the convolutional block attention module for classification and detection. Huang et al. [103] introduced SE block to promote useful features and suppresses less valuable features and also introduced dropout to avoid the overfitting problems. Jin et al. [186] proposed a (3AUNet) triple attention UNet combination of spatial attention, channel attention, and context attention. Spatial attention allows the segmentation network to find the blood vessel region that needs attention, thereby suppressing noise. Channel attention makes the expression of features more diverse and highlights the feature channels with key information while the context attention

helps in guiding the attention. Xiao et al. [105] introduced the ResNet weighted attention mechanism so that model only pays attention to the target ROI area and discards the irrelevant noisy background. The authors introduced the contrast limited adaptive histogram equalization (CLAHE) operation as a preprocessing step to enhance the image contrast. Zhang et al. [106] used multiscale pyramid blocks and a deep supervision concept. Pyramid scale aggregation blocks (PSAB) were used in both the encoder and decoder sections to the reduce loss of information during scaling. For using PSABs in the encoder, scaled input images were added as extra inputs. While using PSABs in the decoder, scaled intermediate outputs were supervised by the scaled segmentation labels. He et al. [187] proposed semi-supervised 3D fine renal artery segmentation framework, DPA-DenseBiasNet, which combines deep prior anatomy (DPA), dense biased network (DenseBiasNet) and hard region adaptation loss (HRA). Dense biased connection, the DenseBiasNet fuses multi-receptive field and multi-resolution feature maps for large intra-scale changes. This dense biased connection also obtains a dense information flow and dense gradient flow so that the training is accelerated and the accuracy is enhanced. DPA features extracted from an autoencoder (AE) are embedded in DenseBiasNet to cope with the challenge of large inter-anatomy variation and thin structures.

3) NON-VASCULAR UNET DESIGNS CHARACTERISTICS

Chahal et al. [88] proposed an automatic segmentation model based on UNet and Xception for the prostate regions in MRI scans. The authors used one convolution and 12 separable convolutions in the contractual path. Separable convolution gives similar performance while being much more efficient in terms of using much fewer parameters and fewer floating-point operations (FLOPs). In the decoder phase, the authors used residual and transpose convolution. Chen et al. [89] proposed a 2D bridge network with a combination of ReLU and e-ReLU functions for deeper networks. To bridge the networks, authors used a concatenation operation that guarantees the information flow or better feature fusion that merges the feature at a different encoder and decoder level. In skip connection, the authors used addition to avoid redundancy and combine low-level features with high-level semantic features. The authors introduced the concept of a combination of ReLU and e-ReLU functions to improve segmentation performance. He et al. [83] proposed the HF-UNet that had two complementary branches for two tasks, with the novel proposed attention-based task consistency learning block to communicate at each level between the two decoding branches. Therefore, HF-UNet had the ability to learn the shared representations hierarchically for different tasks and preserve the specificities of learned representations for different tasks simultaneously. Liu et al. [92] proposed an improved 2D UNet model that integrated the squeeze-and-excitation (SE) layer for prostate cancer segmentation. The SE layer was used to extract only the important features. A dropout block was used to avoid overfitting problems. Machireddy et al. [132]

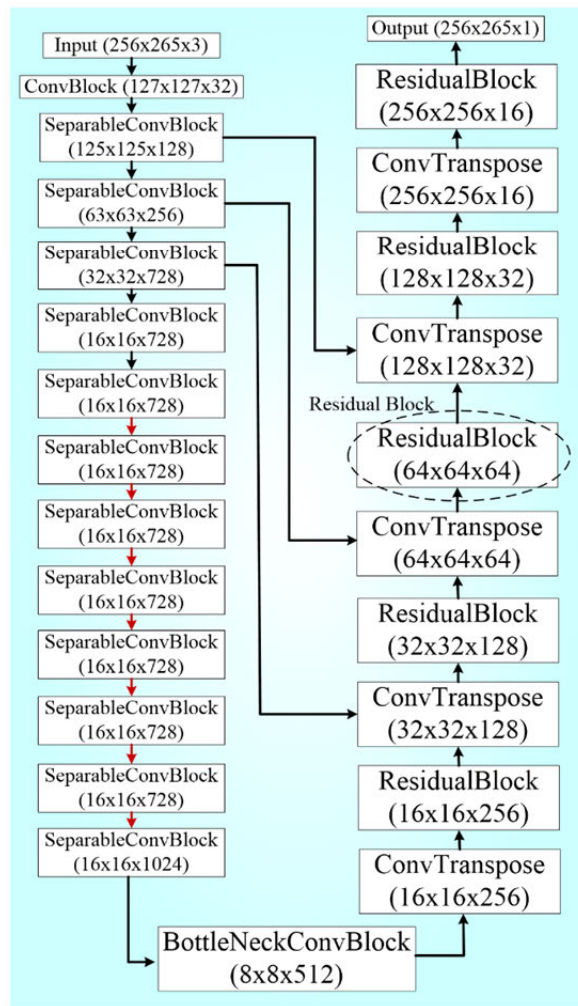
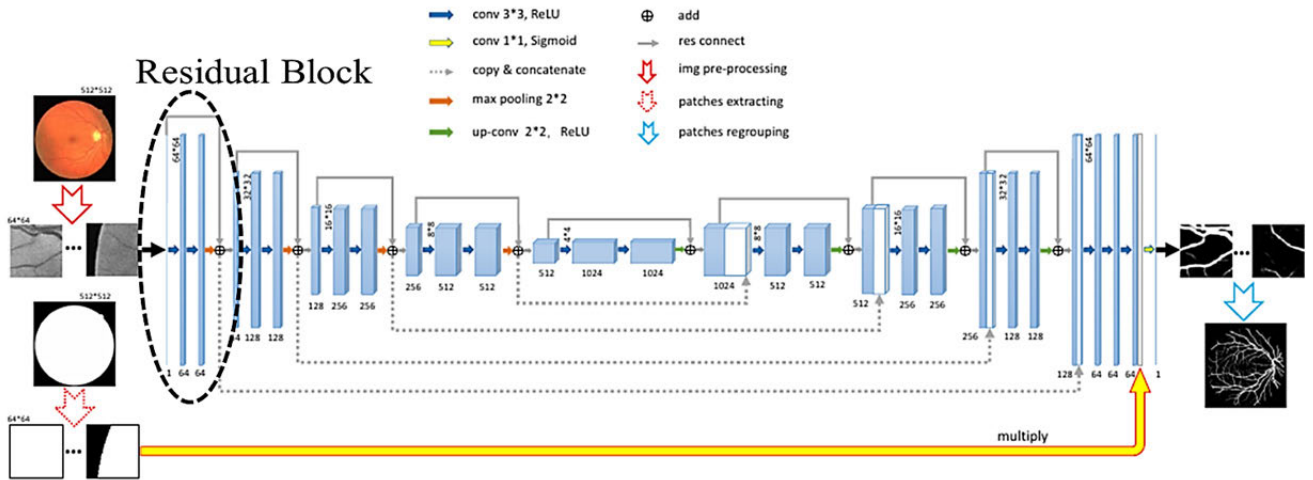


FIGURE 19. Similarity through residual block. Top: Vascular [105]; Bottom: Nonvascular [88].

proposed an attention-based UNet for prostate segmentation. The attention mechanism preserves only the regions of the feature maps relevant for malignancy detection. The attention

mechanism was incorporated in the form of attention gates integrated into the UNet architecture before feature concatenation. The attention gate takes input from the encoder via

skip connections and just below the layer information was also passed as input to the attention gate. Dropout rates of 50% were also introduced to avoid over fitting problems. Xiangxiang et al. [84] proposed a UNet with eight layers and a residual block for prostate segmentation. Residual blocks were used to solve the problem of degradation. Vacacela et al. [188] proposed prostate segmentation which was based on two UNet, one for global and another for local. Global UNet segmented the whole prostate gland while local UNet segmented the central gland. Umapathy et al. [189] proposed a cascaded multi-residual UNet (MRes-UNet) for prostate segmentation. The first MRes-UNET predicts the mask for the prostate gland. The detected prostate mask was concatenated to the input image. The second MRes-UNET CNN used this multi-channel data to predict the central gland within the prostate. The residual block was introduced to avoid the problem of vanishing gradients. In skip connection, instead of using concatenation, the authors introduced feature addition to avoid redundancies in feature maps.

Zhang et al. [85] proposed Z-Net, which contained five pairs of Z-block and decoder Z-block with different sizes and numbers of feature maps assembled in a way similar to that of UNet. The proposed architecture can capture more multi-level features by using concatenation and dense connectivity. Zhu et al. [93] proposed a cascading UNet for prostate segmentation. Step 1 consisted of segmentation of the whole prostate gland (WPG), while step 2 consisted of another identical network to segment the peripheral zone (PZ). According to the segmented result in step 1, an image that contains the WPG area was passed as an input to the next UNet (as part of the step 2), which segmented the PZ area. Based on the above discussions, we conclude the following similarities and dissimilarities broadly.

Zeng et al. [190] proposed a 3D UNet with Multi-level Deep Supervision because 3D-UNet allows segmentation of 3D volumes, with high accuracy and performance and multi-level deep supervision remove the problem of potential gradient vanishing problem during training.

4) SIMILARITIES BETWEEN VASCULAR AND NON-VASCULAR UNET PARADIGM

Architectures used in both vascular and nonvascular UNet paradigms are the different variations of UNet like UNet with dense block [122], parallel fusion, and serial embedding multiscale feature dense UNet [102], UNet with spatial attention [139], the combination of more than one UNet [186], weighted attention UNet [105], pyramid UNet [106] in the case of retinal vascular, 3D UNet for renal vascular [191] and in case of prostate nonvascular UNet variations like UNet with Xception [88], UNet with residual block [84], [189], 2D bridged UNet [89], UNet with SE block [92], UNet with attention gate [132], UNet with more layers (8) [84], UNet with task consistency learning [83], the combination of UNets (ZNet) [85], and cascaded UNet [93], [189], 3D UNet for proximal femur [187]; (ii) It is observed that dropout block [92], [103], [132], [139], residual block [84], [105], [189]

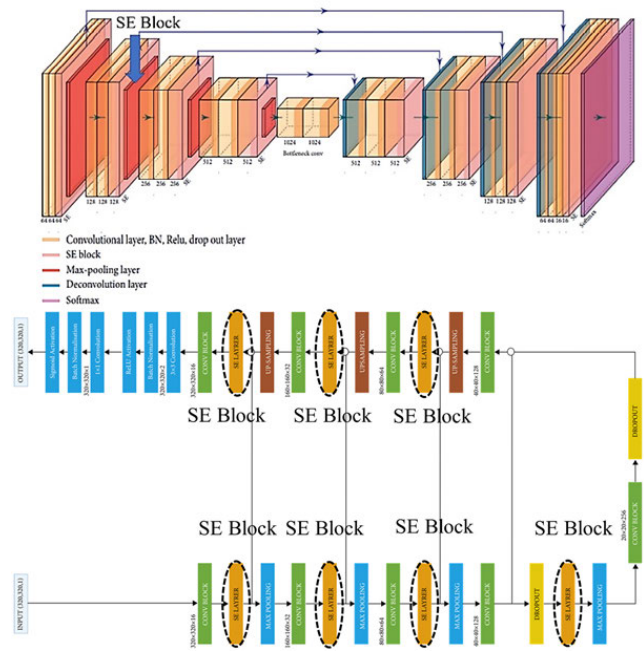


FIGURE 20. Similarity through squeeze-excitation block. Top: Vascular [103]; Bottom: Nonvascular [92].

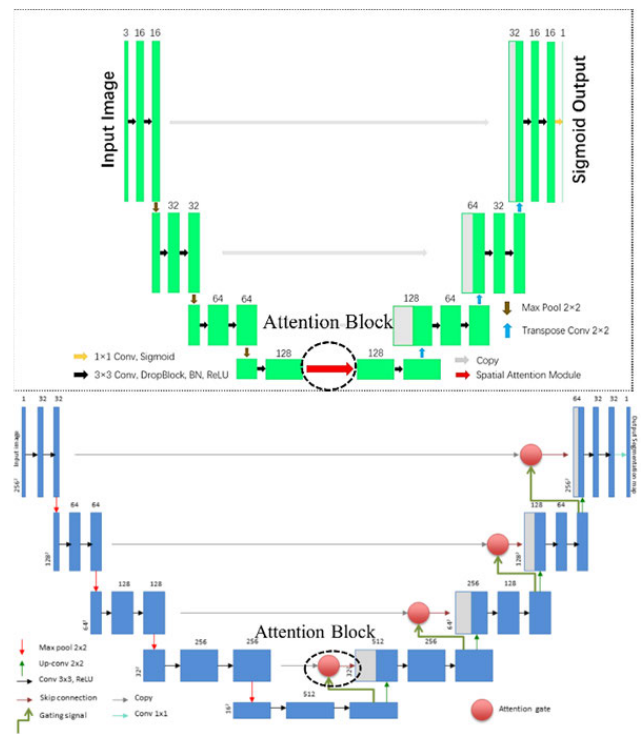


FIGURE 21. Similarity through attention block. Top: Vascular [139] Copyright © 2021, IEEE; Bottom: Nonvascular [132] Copyright © 2020, IEEE.

(Figure 19), SE block (Figure 20), attention gate block [103], [132], [186] (Figure 21), inception block [102], and dense block [102], [122] are common in both vascular and non-vascular UNet paradigms; (iii) The augmentation process is

TABLE 6. Vascular segmentation challenges and corresponding UNet solution.

SN	Problem Type	Architecture Used	Reference
1	(a) Complex structure and low contrast blood vessel (b) Thick and thin blood vessels	UNet with multiscale input and dense block	David <i>et al.</i> [122] Zhang <i>et al.</i> [106] Du <i>et al.</i> [102] He <i>et al.</i> [187]
2	(a) Presence of diseased area (b) Blood vessel centre reflection (c) Low contrast (d) Thin vessels	UNet with multiscale input, inception block (thin vessels) and dense block (reuse extracted features)	David <i>et al.</i> [122] Zhang <i>et al.</i> [106] Du <i>et al.</i> [102] He <i>et al.</i> [187]
3	(a) Small and fragile blood vessels (b) Blood vessel area and background (c) Uneven lighting and noise	UNet with spatial attention block	Guo <i>et al.</i> [139] Huang <i>et al.</i> [103] Xiao <i>et al.</i> [105] Pham <i>et al.</i> [49] Jin <i>et al.</i> [186]
4	(a) Complex structure of blood vessel (b) Low contrast between retinal target vessel and background image (c) Noise interference	UNet with SE block	Guo <i>et al.</i> [139] Huang <i>et al.</i> [103] Xiao <i>et al.</i> [105] Pham <i>et al.</i> [49] Jin <i>et al.</i> [186]
5	(a) Large noise content (b) Low distinction between vessel and environment (c) Uneven distribution of thick and thin blood vessels	UNet with attention gate	Guo <i>et al.</i> [139] Huang <i>et al.</i> [103] Xiao <i>et al.</i> [105] Pham <i>et al.</i> [49] Jin <i>et al.</i> [186]
6	(a) Extreme variation in the morphology of vessel against noisy background (b) Thin vessels (c) Low discriminative ability at the optic disk area	UNet with weighted attention	Guo <i>et al.</i> [139] Huang <i>et al.</i> [103] Xiao <i>et al.</i> [105] Pham <i>et al.</i> [49] Jin <i>et al.</i> [186]
7	(a) Thin capillaries from colour retinal image (b) Low contrast ambiguousness	UNet with pyramid scale aggregation block (multiscale input)	David <i>et al.</i> [122] Zhang <i>et al.</i> [106] Du <i>et al.</i> [102] He <i>et al.</i> [187]
8	(a) Large intra scale image (b) Large inter-anatomy variation (c) Thin Structure (d) Small volume ratio (e) Small labeled data set	UNet with dense block	David <i>et al.</i> [122] Zhang <i>et al.</i> [106] Du <i>et al.</i> [102] He <i>et al.</i> [187]
9	(a) The potential intensity ambiguity between coronary arteries and surrounding tissues or plaques. (b) Size of the coronary artery is relatively small in comparison with the surrounding tissues (c) Difficult to distinguish the coronary arteries from other tubular structures, e.g., the coronary veins	3D Multi channel UNet	Chen <i>et al.</i> [99]
10	High noise and low contrast in ultrasonic images	UNet with residual block	Rui wang <i>et al.</i> [108]
11	Small data set	Ensemble UNet++ (UNet with eight layers)	Zhou <i>et al.</i> [144]
12	In image principal lines, wrinkles and ridge is one palm (a) Principal lines change little over time (b) Wrinkles are thinner than principal lines and irregular (c) Low resolution image difficult to distinguish among these three.	UNet with context fusion module (attention mechanism)	Guo <i>et al.</i> [139] Huang <i>et al.</i> [103] Xiao <i>et al.</i> [105] Van <i>et al.</i> [49] Jin <i>et al.</i> [186]
13	(a) Relative complexity of IVUS images. (b) The IVUS images varied significantly from the intensity gradient of edge of lumen to the contour curvature of plaques	Eight layered UNet	Dong <i>et al.</i> [116]
14	(a) The coronary circulation has a complex structure with many branches of uneven thickness, and some of the branches are too thin to be segmented accurately (b) The morphology of the coronary artery tree may also vary significantly from person to person (c) There are other types of vascular organs with a similar appearance to the coronary arteries close to the heart, which tend to be mistakenly identified as coronary arteries (d) The coronary arteries only occupy a small volume of the total heart tissue, and this imbalance needs to be accounted for in the segmentation method	UNet with dense block (extract rich and representative features) and Residual block (feature rectification)	Song <i>et al.</i> [114] David <i>et al.</i> [122] Du <i>et al.</i> [102]

TABLE 7. Nonvascular segmentation challenges and corresponding UNet solutions.

SN	Problem Type	Architecture Used	Reference
1	(a) Noise (b) Blurred boundaries (c) Scale variation	Cascaded dense UNet	Li <i>et al.</i> [91] Vacacela <i>et al.</i> [188] Chen <i>et al.</i> [89] Zhang <i>et al.</i> [85] Zhu <i>et al.</i> [86]
2	(a) Noise present in medical image (b) Voxel intensity variation (c) Finite image resolution (d) Anatomy variation of prostate among different individuals	Local and Global UNet	Li <i>et al.</i> [91] Vacacela <i>et al.</i> [188] Chen <i>et al.</i> [89] Zhang <i>et al.</i> [85] Zhu <i>et al.</i> [86]
3	(a) Small Data set (b) Shape, size and location of prostate (depends on different image modality like MRI, CT, mpMR, etc)	2D Bridge-UNet	Li <i>et al.</i> [91] Vacacela <i>et al.</i> [188] Chen <i>et al.</i> [89] Zhang <i>et al.</i> [85] Zhu <i>et al.</i> [86]
4	(a) Unclear prostate boundary in CT image (b) Large background noise (c) Prostate located in small region of CT image	Attention based HF-UNet	He <i>et al.</i> [83] Liu <i>et al.</i> [92]
5	Segmentation of prostate gland and peripheral zone in one pass	Cascaded MRes-UNet	Umapathy <i>et al.</i> [189] Xiangxiang <i>et al.</i> [84]
6	(a) The effective area of the prostate is only a small part of the whole image, and it has some troubles to obtain more effective information (b) The contrast between the prostate tissue and the surrounding tissue is low, and the edge region is hard to distinguish	UNet with residual block	Xiangxiang <i>et al.</i> [84] Umapathy <i>et al.</i> [189]
7	(a) Inter and intra variability (b) variations in terms of dynamic range, voxel size, position, field of view as well as anatomical appearance	ZNet	Li <i>et al.</i> [91] Vacacela <i>et al.</i> [188] Chen <i>et al.</i> [89] Zhang <i>et al.</i> [85] Zhu <i>et al.</i> [86]
8	(a) The heterogeneous anatomic structure of the prostate and its surrounding tissue (b) Wide variation in size and shape among different subjects adds to the difficulty in the determination of prostate boundaries	Cascaded UNet	Li <i>et al.</i> [91] Vacacela <i>et al.</i> [188] Chen <i>et al.</i> [89] Zhang <i>et al.</i> [85] Zhu <i>et al.</i> [86]
9	(a) Size and shape of liver under different scanning parameters. For different people, it is different (b) Low intensity contrast between liver and its neighbouring organ (c) Noise inside the image	UNet with convolutional neural network	Liu <i>et al.</i> [267]
10	(a) Localization of prostate cancer (b) Detection of malignancy	UNet with SE block	He <i>et al.</i> [83] Liu <i>et al.</i> [92]

also common in both vascular and non-vascular paradigms; and 3D UNet (Figure 22).

5) DIFFERENCES BETWEEN VASCULAR AND NONVASCULAR UNET PARADIGMS

It is observed that in the case of retinal vascular, multi-scale input was preferred [102], [122], but in the prostate, nonvascular multiscale input was not preferred (Figure 23, Figure 24, Figure 25, Figure 26); (ii) It is observed that the bottleneck used different mechanisms in the case of vascular like David et al. [122] introduced dense block

in the bottleneck, Guo et al. [139] introduced spatial attention, Jin et al. introduced context aggregation block, Zhang et al. [106] introduced PSAB block. In the case of nonvascular, was observed that bottleneck, there was no such change (Figure 21, Figure 22, Figure 23, and Figure 24). Visualization of UNet classification results in the vascular and non-vascular application are detailed in the Figure 27 and Figure 28.

The visual superiority of the proposed framework (DPA-DenseBiasNet). The blue boxes indicate the high segmentation quality of artery endings via our DenseBiasNet

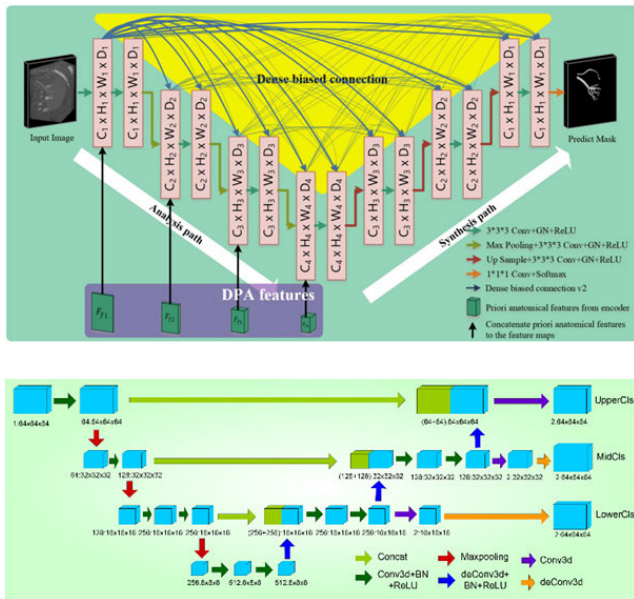


FIGURE 22. Similarity through 3D UNet. *Top*: Vascular [187], [191]; *Bottom*: Nonvascular [190].

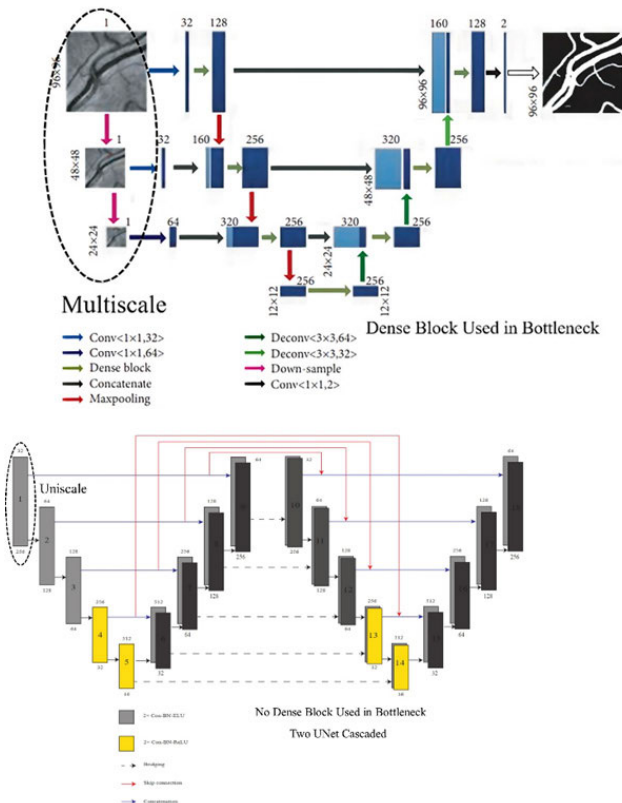


FIGURE 23. Difference through dense block & scale. *Top*: Vascular [122]; *Bottom*: Nonvascular [89] Copyright © 2019, IEEE.

and the yellow boxes indicate the high segmentation quality of the singular regions brought by our DAP strategy. The visualization was depicted in the Figure 29.

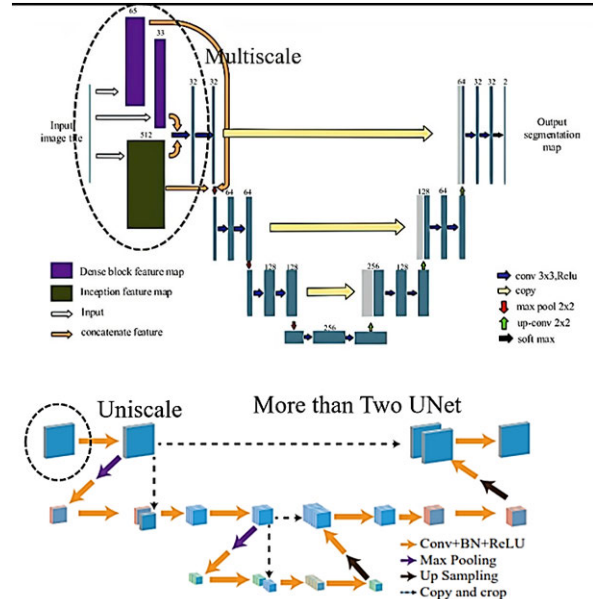


FIGURE 24. Difference through scale. *Top*: Vascular [102]; *Bottom*: Nonvascular [85] Copyright © 2019, IEEE.

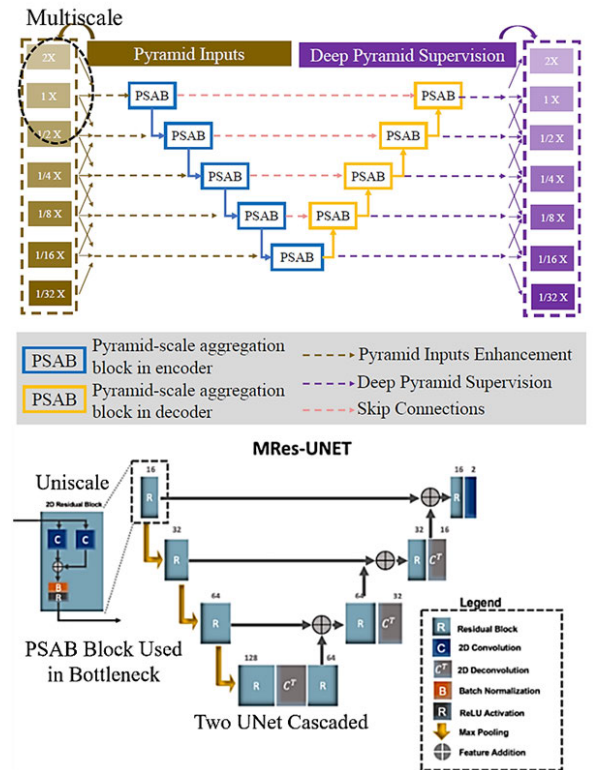


FIGURE 25. Difference through scale & PSAB block. *Top*: Vascular [106] Copyright © 2021, IEEE; *Bottom*: Nonvascular [189].

6) SEGMENTATION CHALLENGES: ARCHITECTURE SOLUTIONS-KEY

a: VASCULAR PROBLEMS AND CORRESPONDING UNET VARIATIONS AS A SOLUTION

Table 6 below shows the relationship between the “vascular problem type” and “UNet architecture solution” along

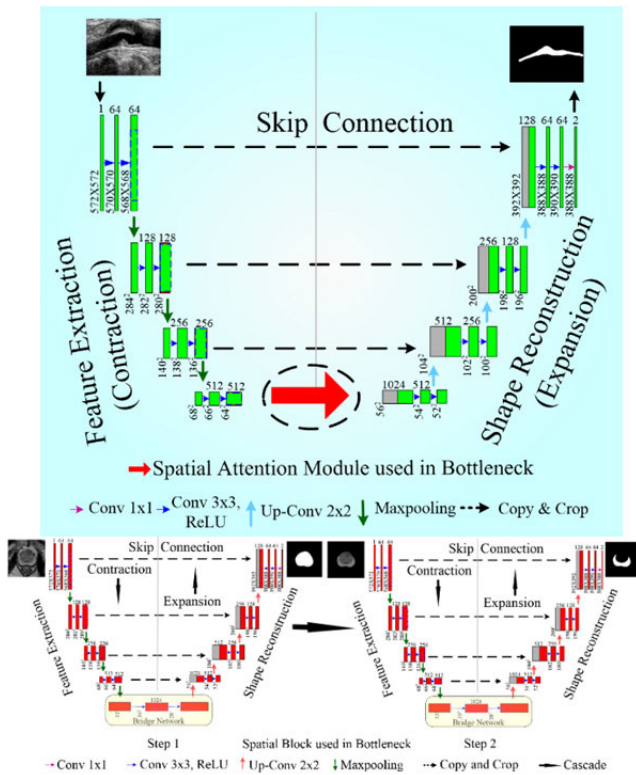


FIGURE 26. Difference through attention block. Top: Vascular [139]; Bottom: Nonvascular [93].

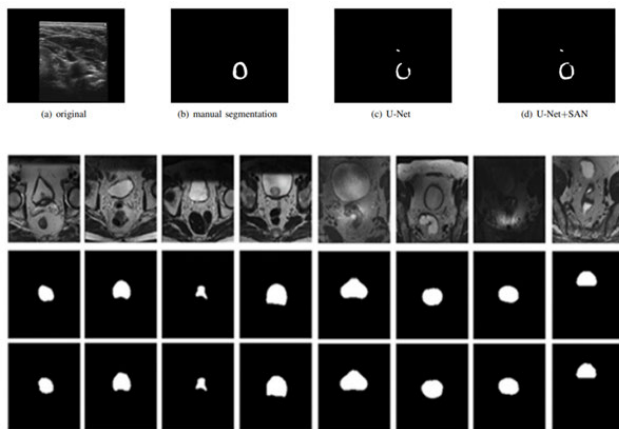


FIGURE 27. Visualization of classification results in vascular (top) [112] (Copyright © 2020, IEEE) and nonvascular (bottom) [144] (Reproduced with permission) applications [88].

with the “reference type”. We conclude that when we have large intra-scale image, large inter-anatomy variation, and thin structure, then dense network can we used [102], [106], [114], [122], [187]. This is because dense network fuses multi receptive field and multi-resolution feature map. If an image contains lots of noise, then we can use attention-based UNet because attention gate chooses the relevant part and suppresses the irrelevant part [49], [102], [139], [186]. If the image contains thin blood vessels, then we can use UNet

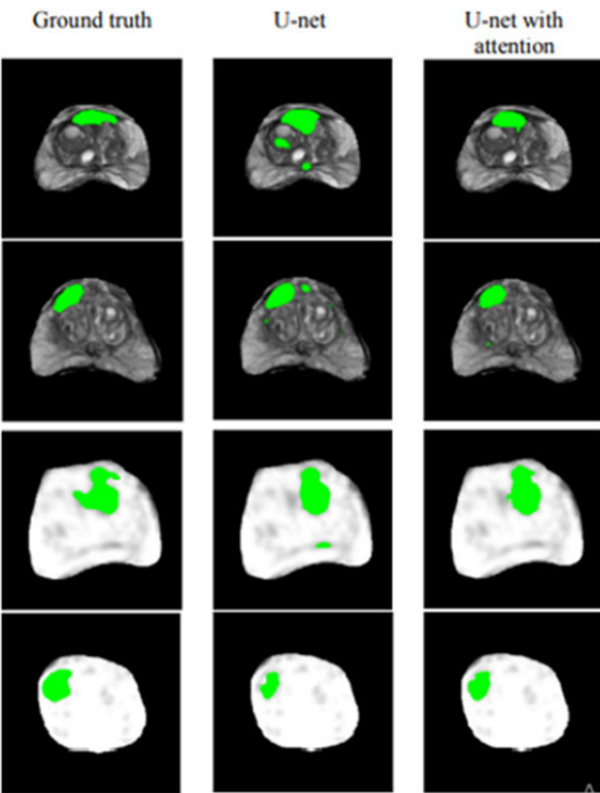
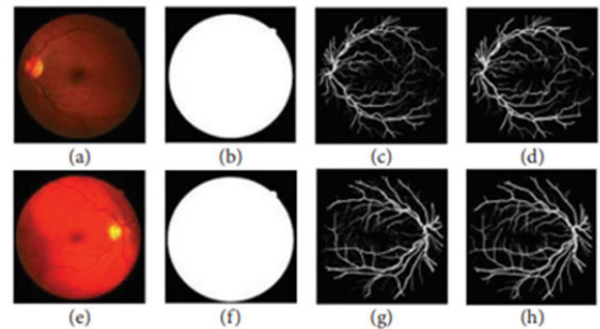


FIGURE 28. Visualization of classification results in vascular (top); Retinal images’ segmentation: (a, e) retinal images in color; (b, f) result from masking; (c, g) human reference; (d, h) result of the proposed U-Net architecture [122] and nonvascular (bottom) [144] (Copyright © 2020, IEEE) applications [132].

with the inception block because inception block has multiple scale or size of convolution so it extracts more features and also uses less number of parameters [102]. If image contains thin blood vessels, then we can UNet with multiscale input because multiscale input provides a way to learn more multiscale data [102], [106], [122]. If the image contains low contrast, then residual block can also be used, as in order to extract more features. This is because residual block helps in deepening the network and therefore better feature extraction [108]. But at a certain point, while going to deeper into network saturation occurs due to which further increase of layers cannot be made as it causes degradation due to gradient loss. The residual UNet [53] overcome this problem

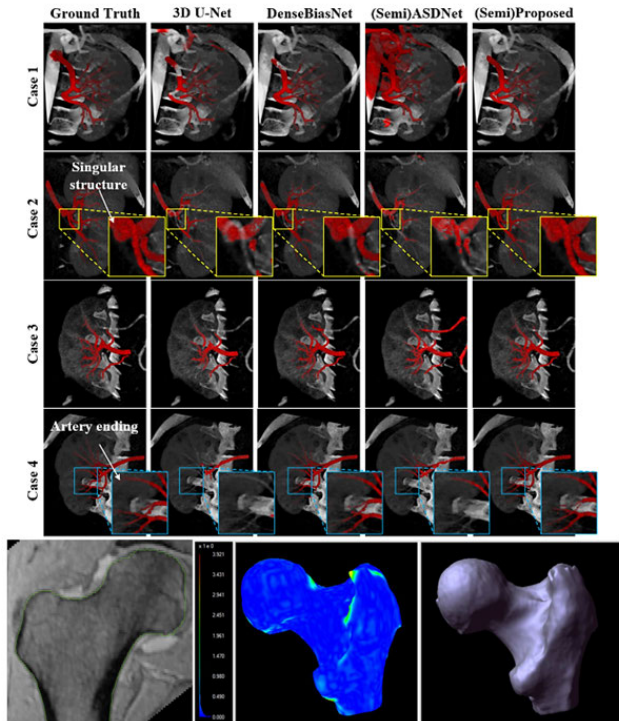


FIGURE 29. Visualization results of 3D. *Top: Vascular [187]; and Bottom: Non-vascular [190].*

and are good at low contrast as it adds the skip connection. By skip connection, the feature map is passes from previous layer into next layer. This process allows to preserve better feature map and improved performance when going deeper into network”.

Li et al. [192] proposed, a deep learning network framework based on the low-order residual network is to detect low contrast defects. Especially, a low-order feature extraction module is designed in order to effectively extract target features with low contrast and small size. The size of the convolution kernel directly affects the receptive field of the model. The kernel size used in the AlexNet is very large, in 2012, for example 11×11 and 5×5 . At first, it was considered that the receptive field increases with the enlargement of the convolution kernel, so that more picture information and better features can be acquired. However, large convolution kernels would lead to a huge increase in computational complexity, which is not conducive to the increase of model depth, and reduces the computational performance. Therefore, in VGG and Inception Networks, the combination of two 3×3 convolution kernels is better than one 5×5 convolution kernels, and the parameters are reduced from 26 ($5 \times 5 \times 1 + 1$) to 19 ($3 \times 3 \times 2 + 1$). Thus, 3×3 kernels are widely used in various models. The receptive field of 1×1 convolution kernel is 0, so it is generally not used for feature extraction. However, as for low-contrast features, 3×3 convolution kernel may inhibit the expression of some features at the beginning of training. Therefore, the convolution kernels with

size 3×3 are used as feature extraction part, while low-order residual blocks with convolution kernels size of 1×1 are used to enrich the features to be extracted. Although the receptive field of a 1×1 kernel is 0, it can effectively retain the feature information for the defective target with low-contrast and only one pixel size, and is not disturbed by the neighborhood pixels.

b: NON-VASCULAR PROBLEMS AND CORRESPONDING UNET SOLUTIONS

Table 7 below shows the challenges in the segmentation of non-vascular type and the corresponding UNet-based solution. We conclude that if variations in terms of dynamic range, voxel size, position, field-of-view as well as anatomical appearance are present, then more than one UNet [85], [89], [91], [188] with dense block is suitable. For example, the ZNet (Zhang et al. [85]) is capable of capturing more features in a multi-level fashion by using concatenation and dense connection. Attention-based UNet [83], [92] was suitable when image contains large background noise as the attention gate is capable of extracting relevant parts and ignoring irrelevant ones. When we need segmentation of the prostate gland and peripheral zone in one pass, then we can use cascaded MRes-UNet [189], as the first MRes-UNet predicts the mask for the prostate gland. The detected prostate mask is then concatenated to the input image. The second MRes-UNet CNN uses this multi-channel data to predict the central gland within the prostate. The peripheral zone is identified using the central gland prediction as an exclusion mask within the prostate prediction.

VII. EXPLAINABLE AI IN VASCULAR AND NON-VASCULAR PARADIGM

DL has dominated the field of image segmentation in both vascular and non-vascular areas. Our study has shown the role of five kinds of UNet in both categories, filled with innovative designs demonstrating superior performance against the conventional models. While the engineering mission of design and performance meets the objectives, but the black box nature of DL possesses unanswerable “Wh” questions like what or why or even how the DL systems performed and met the objectives. Such challenges are categorized as a subfield of AI, called “explainable AI (XAI)” [193], [194]. Several studies have been published in XAI, but are limited in the field of vascular and non-vascular applications for segmentation utilizing UNet variations. The need XAI is even more important when building a relationship or correlations or links between the quantified vascular segments of different kinds of clinical outcomes [16], [195], [197]. There are two reasons, (a) XAI started around the corner less than *seven* years ago (2015), and (b) some of the tools like Shapley Additive Explanations (SHAP) [198], [199] and UMAP [200] are not integrated with DL packages, which are typically adapted in the computer vision industry. The European general data protection regulation (GDPR) has elaborated on the role of fairness, privacy, transparency, and

explainability in DL paradigm [201]. Since XAI incorporates the feedback loop, the customized seven steps of DL can be exhibited in Figure 30, consisting of DL training, quality assurance (QA), installation/deployment, prediction, and cross-validation-based testing (A/B test), monitoring, and debugging. The few limited UNet-XAI systems are briefly summarized here [202], [203], [204]. The Heatmap produced by Grad-CAM have been used for XAI in several applications (Figure 31-32) [205], where, the generated heatmaps are the threshold to compute the lesions, which are then compared against the gold standard [179], [202], [206], [207].

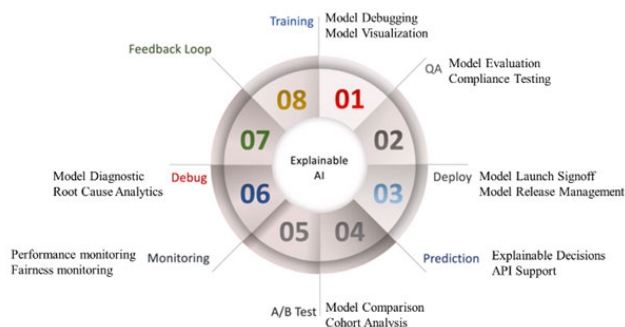


FIGURE 30. Eight aspects of Explainable AI [201].

A. A NOTE ON EXPLAINABLE ARTIFICIAL INTELLIGENCE

Since DL applications have outperformed humans in many tasks, including picture and speech recognition, and recommendation systems, they have attracted a lot of attention. These applications, however, are not reliable or comprehensible. DL models are frequently viewed as opaque, difficult-to-understand black boxes with complicated underlying mechanisms. People can't trust them because they don't provide reasons for their choices or predictions. On the other hand, depending on the application, errors made by artificial intelligence algorithms could be fatal. More specifically, a mistake in an autonomous vehicle's computer vision system could cause a collision, while in the medical field, patient lives depend on these choices. Explainable AI (XAI) enters the scene to address the aforementioned problems. Machine learning models perform as a black box (Figure 33 (a)) i.e. model predicts the results only but not able to explain "wh family" like why do you do that?, why can I trust you?, why not something else?, when do you success?, when do you fail? and many more.

Figure 33 (b) shows comparison between deep learning model and explainable model with the help of example. In the figure w1b, want to predict the particular object is car or not. In the deep learning model (2D convolutional neural network used), gives the prediction 0.89 percent for particular object is car but not explain why is this a car? how did you predict that? In explainable model, model explain it has wheels, lights and also visual features obtained from the model so that user understands why the particular object is car.

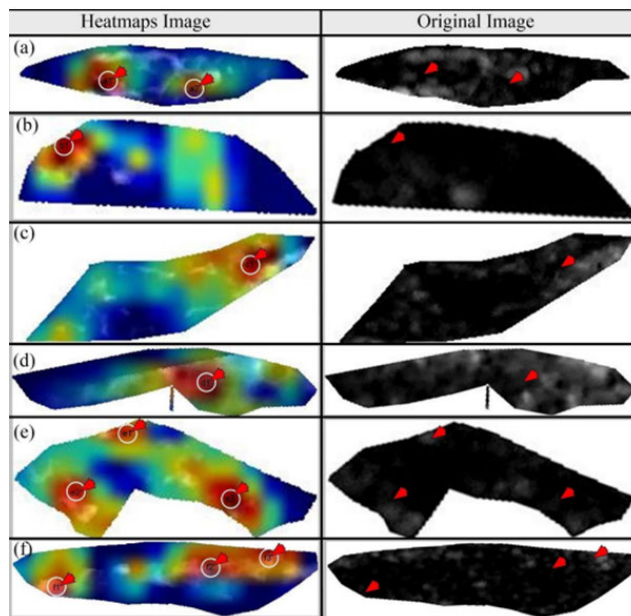


FIGURE 31. Demonstration of heatmaps demonstrating the symptomatic lesions in carotid artery. Red zones are vulnerable zones, while green blue regions are low-risk regions [206].

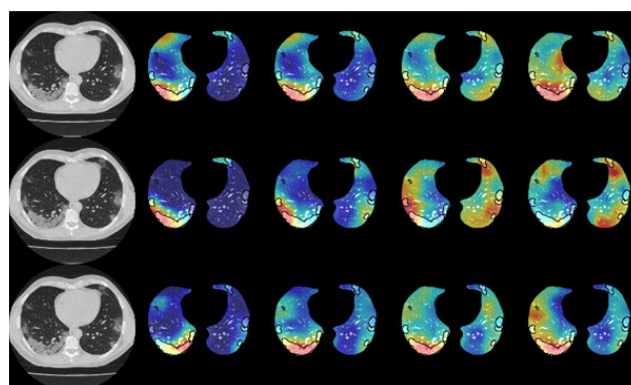


FIGURE 32. Superposition of heatmaps (representing lesions) with gold standard (black border regions) for COVID-19 lesions for XAI demonstration [179].

B. IMAGE SEGMENTATION USING UNET WITH XAI MODEL

There are some deep learning models like GPU-Net [208], CA-Net [113] are trying to provide explanations of their predicted outcome, however, most of UNet require explanations. Chatterjee et al. [209] proposed a unified, flexible and scalable interpretability and explainability pipeline named TorchEseGeta (Figure 34). The proposed architecture provided posthoc interpretability and explainability methods and incorporates all libraries related to interpretability and explainability like LIME, SHAP and TorchRay and extended to apply on 2D and 3D deep learning models for images. Authors used the segmentation model from DS6 [210] paper and the models were UNet, UNet-MSS(multi-scale supervision) and UNet-MSS with deformation. In order to evaluate proposed architecture for segmentation model, vessel segmentation was chosen.

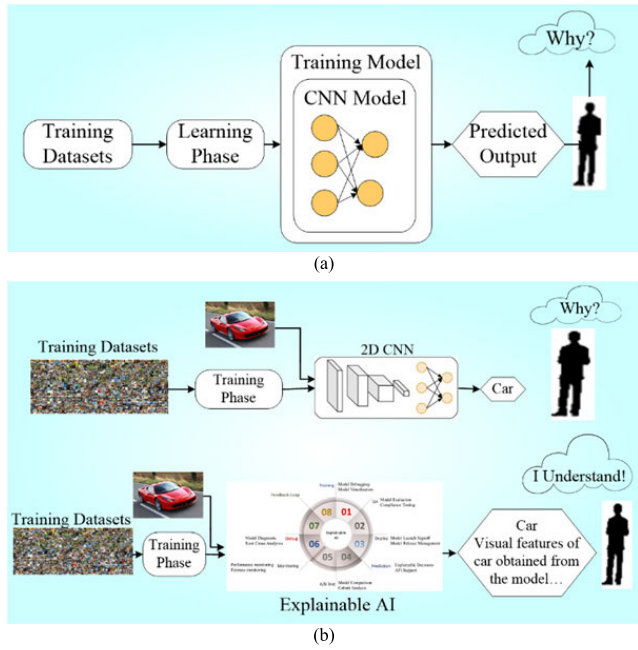


FIGURE 33. (a). Machine learning models perform as a black box. (b). Comparison of a deep learning and an explainable model.

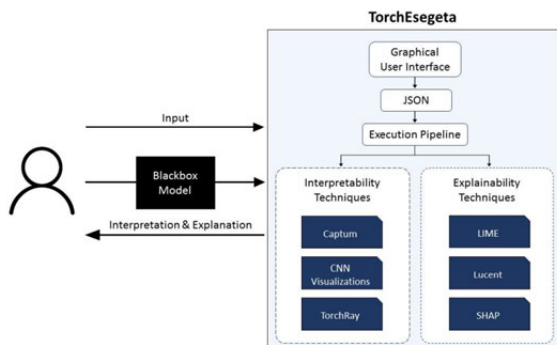


FIGURE 34. Torchesegeta pipeline architecture [209].

Dasanayka et al. [211] proposed an architecture (Figure 35) for brain tumor analysis using MRI and whole slide images [WSI]. Proposed architecture divided into three steps. The first step was MRI segmentation module in which variational AutoEncoder (VAE) 3DUNet [212] was used. Input for this step was 3D MRI volumes and output was segmented 3D MRI volumes. Second step was MRI classification module for this DenseNet was used because DenseNet classify the problem accurately with less number of parameters. For the interpretability Grad-CAM was included in this step. The third step WSI classification module. Feature extraction was carried out by already train ResNet50 model. The output of ResNet50 model was a feature vector of size 1024×1 for each patch which later send to classification phase carried out by a model which was composed by densely connected layers. Melching et al. [213] proposed a model ParallelNet which was shown in Figure 36 (a). In ParallelNets architecture original UNet was fused with fully connected neural

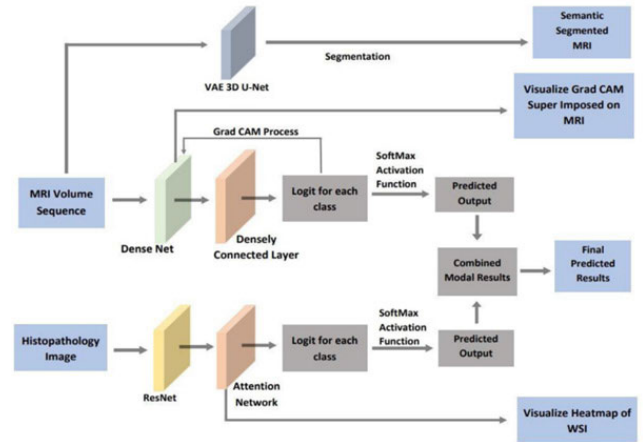


FIGURE 35. High level design of web application [211].

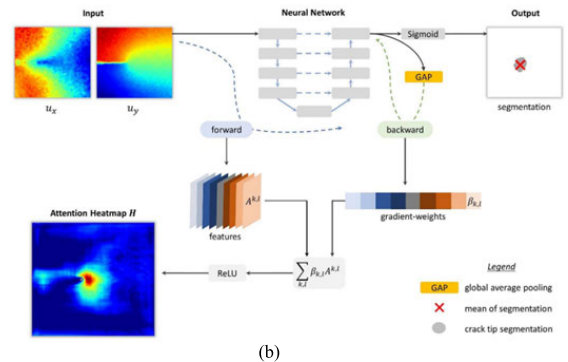
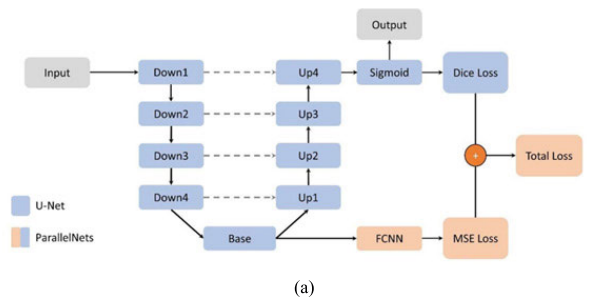


FIGURE 36. (a). ParallelNets Architecture (Blue color original UNet and orange color is added part) [213]. (b). GradCAM method for visualization of deep neural networks [213].

network (FCNN) at bottleneck. Crack tip segmentation was performed by UNet and crack tip position perform by FCNN regressor. Authors employed the Grad-CAM interpretability approach, as illustrated in Figure 36 (b), to test interpretability. The neural network's internal features were gathered during the forward pass of input data and aggregated by weighting the average pooled gradients computed during the backward pass.

Poudel et al. [214] proposed a novel architecture which was based on Eff-UNet [176] and focusing on precise segmentation of polyps. The architecture shown in Figure 37.

The architecture divided into two modules. First module was UNet encoder that uses Efficient-Net as a backbone that provides different semantic level details at different stage, in second module decoder combined all spatial information from multiple stage and finally predict the segmentation mask. Zhang et al. [215] proposed an attention UNet, an interpretable classification model that can generate high resolution localization feature maps for predicted class. This model adopt up-sampling-concatenation-convolution structure to create fine grained segmentation map and use attention pooling over the prior mask for bridging segmentation with classification. Authors integrate this model with GradCAM for explainability. The structure shown in Figure 38.

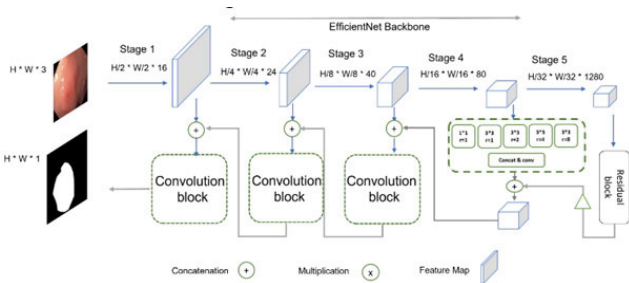


FIGURE 37. Overview of proposed architecture [214].

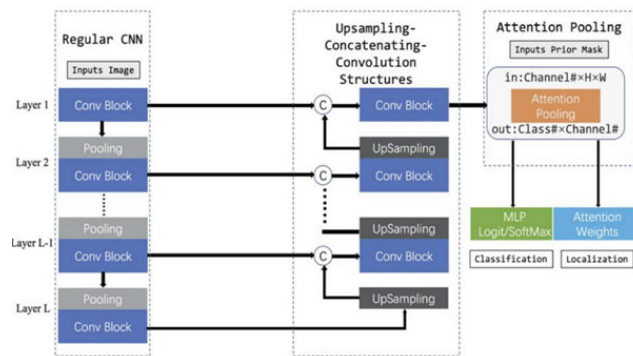
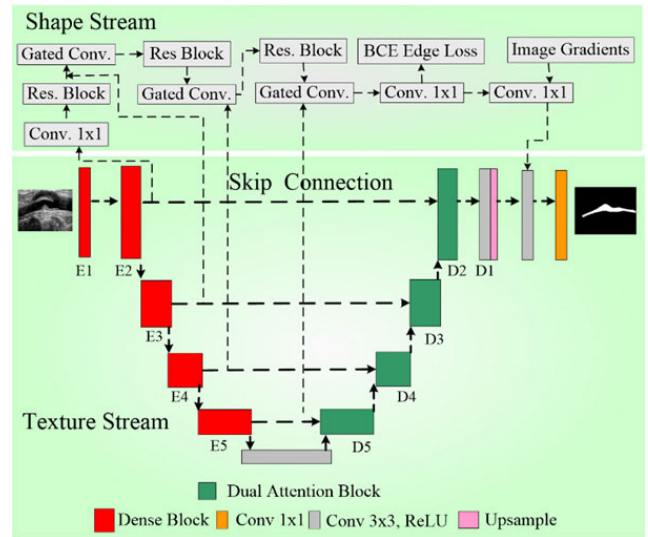


FIGURE 38. Architecture of attention UNet [215] (Copyright ©2020, IEEE).

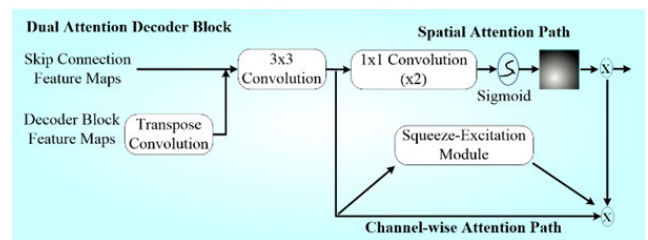
Sun et al. [216] proposed a novel architecture SAUNet: shape attentive UNet for interpretable medical image segmentation, shown in Figure 39 (a). Proposed architecture comprises two streams. First one is texture stream, which had similar structure as UNet but encoders was replaced by dense blocks and decoders are replaced by proposed dual attention decoder block as shown in figure 39 (b). The second stream was shape stream, which had gated convolutional layers and residual layers. The gated convolutional layer used to fused shape features with texture features and the use of residual layer was to fine tune the shape features as shown in Figure 39 (a).

C. APPLICATION

All medical image applications need explainability and interpretability either vascular or non-vascular applications.



(a)



(b)

FIGURE 39. (a). Proposed architecture of Attentive UNet [216]. (b). Dual attention decoder block [216].

In lieu of this UNet with explainability (XAI) gives a new horizon in medical field both vascular and non-vascular.

VIII. PRUNING STRATEGIES IN UNET-BASED DEEP LEARNING

While the UNet-based DL has provided a gold mine for segmentation solutions, the inherent “deep approach” in neural networks has created a bottleneck in the model generation. Due to many epochs and a large number of training iterations per epoch, besides the heavy weightlifting of several layers in UNet during encoder and decoder phases, there is an increase in both storage space and time during the training paradigm of UNet-based DL. It poses a threat to real-time processing, especially in healthcare frameworks. The computer vision industry has provided alternatives, such as the introduction of graphical processing units (GPU) and supercomputers; however, this is a game in which the “rich get the highest,” and several good talents are starving to get their hands on it. Thus, the computer vision field has now started looking into methods that can improve training model storage and speed. This strategy banks on the optimization of hyperparameters during the deep learning process, where the objective is to “shave” the unlikeable weights in deep neural networks as the deep cycles churn. Analytical methods cannot be used to determine a neural network’s weights. Instead, the weights

must be found using the stochastic gradient descent empirical optimization method. The optimization problem for neural networks that stochastic gradient descent attempts to solve is difficult, and the space of solutions (sets of weights) may contain both many excellent answers (known as global optima) and simple, low-skill ones that are also easy to find (called local optima). The “learning rate”—also known as the step size—is the measure of how much the model is altered throughout each phase of this search process. It is possibly the most crucial hyperparameter to adjust for your neural network in order to get optimal performance on your challenge. The learning rate will interact with many other aspects of the optimization process, and the interactions may be nonlinear. Nevertheless, in general, smaller learning rates will require more training epochs. Conversely, larger learning rates will require fewer training epochs. Further, smaller batch sizes are better suited to smaller learning rates given the noisy estimate of the error gradient. A robust strategy may be to first evaluate the performance of a model with a modern version of stochastic gradient descent with adaptive learning rates, such as Adam, and use the result as a baseline. Then, if time permits, explore whether improvements can be achieved with a carefully selected learning rate or simpler learning rate schedule. Here optimization of hyper-parameters means optimization of stochastic gradient descent and Adam optimizer. The computer vision industry has now started using “evolutionary algorithms” to optimize these hyperparameters, such as (i) differential evolution (DE), (ii) genetic algorithm (GA), (iii) particle swarm optimization algorithm (PSO), and (iv) whale optimization algorithm (WO) [207, 217]. It has been shown recently that such optimization methods can be embedded in deep learning frameworks such as (i) Fully connected network (FCN) and (ii) SegNet. There has been no attempt to fuse such evolutionary methods with UNet-based DL for vascular applications, but we foresee this in the near future. Therefore, we have attempted to summarize the pruning methods into the following categories. The current pruning literature has been classified into three categories: (i) channel pruning (so-called filter pruning), (ii) network pruning, and (iii) hybrid pruning. The main principle of channel pruning is to cut down the filters at an early stage of the AI model design [122], [123], [124], [125], [126], [218], [219], [220], [221], [227]. We also call it as early pruning. In the network pruning, we remove the neurons of the network that are low in weight [228], [229], [230], [231], [232], [233], while in hybrid pruning, we fuse the process of weight reduction using temporal and spatial information [234], [235], [236].

A. CHANNEL PRUNING METHOD

Channel pruning (Figure 40), sometimes referred to as filter pruning, makes use of certain algorithms to identify the crucial and superfluous filters in the model [237]. The model’s redundant filters are eliminated without compromising quality. There are two types of filters pruning techniques. One is unstructured, which means that individual weights have been removed, and the other is structured, which means that

convolutional channels have been removed [227]. Channel weights from all layers are reduced to their smallest sums when non-sequential layers are assessed [238]. Convolutional inputs are removed from the network through other methods, such as channel pruning, which have the least influence on the model output [227].

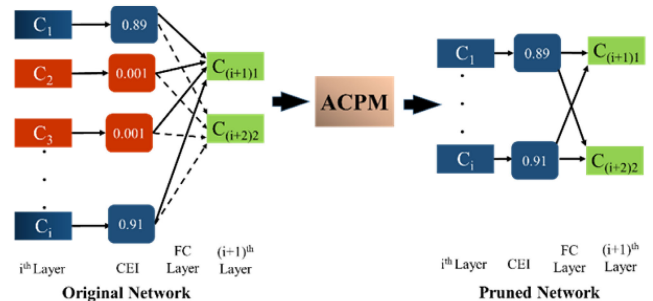


FIGURE 40. Adaptive channel pruning model [239]. FC: fully connected network.

B. NETWORK PRUNING METHOD

Network (weight) pruning methods provide condensed representation and seek to create a small and faster model. This pruning strategy’s fundamental tenet is to trim weights using lp-norm regularization. Additionally, if the weights are not essential, the model’s accuracy can be maintained without them [240]. In order to find the low-contributing weights that may be either trimmed or fine-tuned, a specified threshold is taken into consideration.

C. HYBRID PRUNING METHOD

Hybrid pruning (Figure 41) is a combination of more than one pruning technique, either (a) weight pruning with filter pruning or (b) coarse-grained channel pruning with fine-grained weight pruning [241].



FIGURE 41. Hybrid pruning architecture of convolution neural network [241].

IX. BIAS IN UNET-BASED DESIGNS FOR VASCULAR AND NON-VASCULAR APPLICATIONS

A. RANKING-BASED RISK OF BIAS SCORE METHOD

There were 54 vascular and 56 non-vascular studies in our cohort that used UNet-based architecture. For each study, 35 AI-based attributes were created; for a total of 1,890 attributes and 1,960 attributes corresponding to vascular and non-vascular diseases, respectively. These UNet-based features were initially qualitative and then quantified by assigning a score between 0 and 5 based on the nature of attributes by AI scientists with 10 years’ experience [33], [34], [242], [243], [244], [245]. The study’s aggregate score

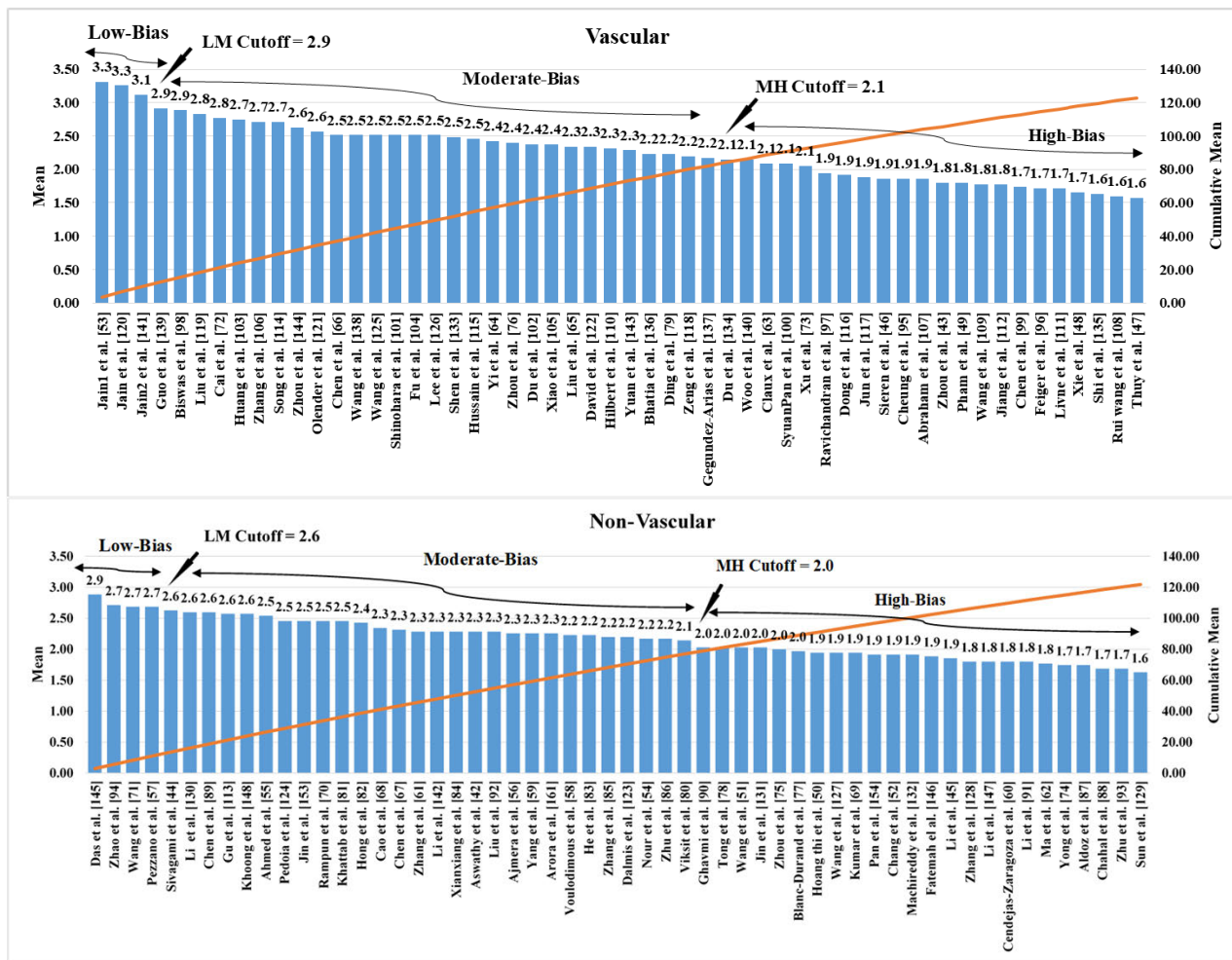


FIGURE 42. Plots for the ranking-bias scores; Top: Vascular studies; Bottom: Non-vascular studies.

is the sum of all attribute values for that selected study. Using the ranking method, the mean values (Table 8 and Table 9) of the 110 UNet-based investigations ranged from 2.7 (left) to 1.1 (right) for the vascular and 2.0 (left) to 1.1 (right) for non-vascular studies, respectively. The higher the mean value, the lower is the risk-of-bias (RoB). Hence, the studies were arranged in the order of low-, moderate-, and high-bias, according to the decreasing order of their aggregate scores. The *low-moderate* (LM) cutoff was 2.6, and the *moderate-high* (MH) cutoff was 2.0 determined for the non-vascular UNet-based studies for RoB by using the intersection of the “cumulative plot and the mean plot curve of the studies” (Figure 42 (bottom)). Similarly, the LM cutoff for the vascular was 3.1 and MH cutoff of 1.9 was determined (Figure 42 (top)). According to the ranking score graph, most of the studies had a *moderate-bias* (ranging from 1.8 to 1.3, in decreasing order left to right, and this accounted for 35 studies (59%) in the non-vascular framework and similarly for the vascular, it ranged from 1.9 to 1.5, with 30 studies (46%).

Note that the studies with higher normalized mean values in the AI attributes were considered as *low-bias*. These low-bias studies showed more innovation in the design for vascular diagnosis. On the contrary, the tail-enders showed low AI attribute mean scores (*high-bias*) and were not clinically substantial compared to *low-bias* or *moderate-bias* studies. We will discuss the analysis of the studies between the three quantitative and innovation methods in next section.

B. RADIAL-BIAS MAP METHOD

Since the UNet technology applied for vascular and non-vascular diagnosis prevails in different stages such as demographics, architecture, performance evaluation, and clinical application, the strengths of different DL attributes were determined (A1 to A35 in Table 10) in these stages (called clusters). The DL attributes in each cluster was 9, 7, 12, and 7, respectively. For estimating the strengths of AI attributes, we used a pictorial representation of the “spokes and wheel model” in 360 directions, where each spoke represents the product of the weight of the attribute times the radius of

TABLE 8. Ranking table for non-vascular studies.

Author	Mean	Cumulative Mean	Rank
Das et al. [145]	2.81	2.81	1
Zhao et al. [94]	2.64	5.44	2
Wang et al. [71]	2.61	8.06	3
Pezzano et al. [57]	2.61	10.67	4
Sivagami et al. [44]	2.56	13.22	5
Li et al. [130]	2.53	15.75	6
Chen et al. [89]	2.53	18.28	7
Gu et al. [113]	2.50	20.78	8
Khoong et al. [148]	2.50	23.28	9
Ahmed et al. [55]	2.47	25.75	10
Pedoia et al. [124]	2.39	28.14	11
Jin et al. [153]	2.39	30.53	12
Rampun et al. [70]	2.39	32.92	13
Khattab et al. [81]	2.39	35.31	14
Hong et al. [82]	2.36	37.67	15
Cao et al. [68]	2.28	39.94	16
Chen et al. [67]	2.25	42.19	17
Zhang et al. [61]	2.22	44.42	18
Li et al. [142]	2.22	46.64	19
Xianxiang et al. [84]	2.22	48.86	20
Aswathy et al. [42]	2.22	51.08	21
Liu et al. [92]	2.22	53.31	22
Ajmera et al. [56]	2.19	55.50	23
Yang et al. [59]	2.19	57.69	24
Arora et al. [161]	2.19	59.89	25
Voulodimos et al. [58]	2.17	62.06	26
He et al. [83]	2.17	64.22	27
Zhang et al. [85]	2.14	66.36	28
Dalmis et al. [123]	2.14	68.50	29
Nour et al. [54]	2.11	70.61	30
Zhu et al. [86]	2.11	72.72	31
Viksit et al. [80]	2.08	74.81	32
Ghavmi et al. [90]	1.97	76.78	33
Tong et al. [78]	1.97	78.75	34
Wang et al. [51]	1.97	80.72	35
Jin et al. [131]	1.97	82.69	36
Zhou et al. [75]	1.94	84.64	37
Blanc-Durand et al. [77]	1.92	86.56	38
Hoang thi et al. [50]	1.89	88.44	39
Wang et al. [127]	1.89	90.33	40
Kumar et al. [69]	1.89	92.22	41
Pan et al. [154]	1.86	94.08	42
Chang et al. [52]	1.86	95.94	43
Machireddy et al. [132]	1.86	97.81	44
Fatemah el al. [146]	1.83	99.64	45
Li et al. [45]	1.81	101.44	46
Zhang et al. [128]	1.75	103.19	47
Li et al. [147]	1.75	104.94	48
Cendejas-Zaragoza et al. [60]	1.75	106.69	49
Li et al. [91]	1.75	108.44	50
Ma et al. [62]	1.72	110.17	51
Yong et al. [74]	1.69	111.86	52
Aldoz et al. [87]	1.69	113.56	53
Chahal et al. [88]	1.64	115.19	54
Zhu et al. [93]	1.64	116.83	55
Sun et al. [129]	1.58	118.42	56

TABLE 9. Ranking table for vascular studies.

Authors	Mean	Cumulative Mean	Rank
Jain1 et al. [53]	3.31	3.31	1
Jain et al. [120]	3.26	6.57	2
Jain2 et al. [141]	3.11	9.69	3
Guo et al. [139]	2.91	12.6	4
Biswas et al. [98]	2.89	15.49	5
Liu et al. [119]	2.83	18.31	6
Cai et al. [72]	2.77	21.09	7
Huang et al. [103]	2.74	23.83	8
Zhang et al. [106]	2.71	26.54	9
Song et al. [114]	2.71	29.26	10
Zhou et al. [144]	2.63	31.89	11
Olender et al. [121]	2.57	34.46	12
Chen et al. [66]	2.51	36.97	13
Wang et al. [138]	2.51	39.49	14
Wang et al. [125]	2.51	42	15
Shinohara et al. [101]	2.51	44.51	16
Fu et al. [104]	2.51	47.03	17
Lee et al. [126]	2.51	49.54	18
Shen et al. [133]	2.49	52.03	19
Hussain et al. [115]	2.46	54.49	20
Yi et al. [64]	2.43	56.91	21
Zhou et al. [76]	2.4	59.31	22
Du et al. [102]	2.37	61.69	23
Xiao et al. [105]	2.37	64.06	24
Liu et al. [65]	2.34	66.4	25
David et al. [122]	2.34	68.74	26
Hilbert et al. [110]	2.31	71.06	27
Yuan et al. [143]	2.29	73.34	28
Bhatia et al. [136]	2.23	75.57	29
Ding et al. [79]	2.23	77.8	30
Zeng et al. [118]	2.2	80	31
Gegundez-Arias et al. [137]	2.17	82.17	32
Du et al. [134]	2.14	84.31	33
Woo et al. [140]	2.14	86.46	34
Claux et al. [63]	2.09	88.54	35
SyuanPan et al. [100]	2.09	90.63	36
Xu et al. [73]	2.06	92.69	37
Ravichandran et al. [97]	1.94	94.63	38
Dong et al. [116]	1.91	96.54	39
Jun et al. [117]	1.89	98.43	40
Sieren et al. [46]	1.86	100.29	41
Cheung et al. [95]	1.86	102.14	42
Abraham et al. [107]	1.86	104	43
Zhou et al. [43]	1.8	105.8	44
Pham et al. [49]	1.8	107.6	45
Wang et al. [109]	1.77	109.37	46
Jiang et al. [112]	1.77	111.14	47
Chen et al. [99]	1.74	112.89	48
Feiger et al. [96]	1.71	114.6	49
Livne et al. [111]	1.71	116.31	50
Xie et al. [48]	1.66	117.97	51
Shi et al. [135]	1.63	119.6	52
Rui wang et al. [108]	1.6	121.2	53
Thuy et al. [47]	1.57	122.77	54

the spoke. The *bias value* ($\mathfrak{F}_{\text{radial}}$) measurement pseudo algorithm is summarized as follows: (i) Divide the AI attributes into four clusters (design, optimization, performance evaluation, and clinical validation) based on the UNet-based DL pipeline. (ii) Compute the spoke length of each AI attribute (weight \times 80% of half the image size (256)). (iii) Calculate the sum of spoke lengths corresponding to four clusters (say Σ_{C1} , Σ_{C2} , Σ_{C3} , and Σ_{C4}). (iv) Calculate the sum of the top two and bottom two clusters (say Σ_A and Σ_B). (v) Compute the $\mathfrak{F}_{\text{radial}} = |\Sigma_A - \Sigma_B|$, as the absolute difference between Σ_A and Σ_B . (vi) The normalized bias value ($\mathfrak{F}_{\text{radial}}^{\text{norm}}$) = ($\frac{\mathfrak{F}_{\text{radial}}}{\alpha}$), where α is the total number of AI attributes. The weight matrix (Tables 10 and 11) presents the weights of the AI attributes based on the experience and judgment of AI professionals. In all, each study has 49 attributes corresponding to every 7.3 ($\sim 360/49$) degrees. The Bezier spline curve is then fitted through the endpoint of each spoke to represent the smooth curve.

Since the curve has four sectors (corresponding to four clusters), the *radial-bias* map resembles butterfly wings, as shown in Figure 43 (right), laid out in 8×7 grid, representing 56 non-vascular UNet-based DL studies and 54 studies for vascular UNet-based DL paradigm, laid in 9×6 grid shown in Figure 43 (left). These studies are arranged from *low* to *high-bias*, where the bias of each study is in the corner of the *radial-bias* map (where the name of the bias map is: “Sn-Name: BiasValue”, for example, “S18-Che:10”, where “18” represents the study number, “Che” is the first three letter of the last name of the first author in the study, and “10” represents the normalized value of the bias). Note that the following is the sequence of AI attributes for each of the four clusters (A1 to A35 in Tables 10 and 11). The AI *demographic cluster* (A1-A9) consisted of (i) total patients, (ii) family history, (iii) type of risk factors, (iv) body mass index, (v) ethnicity, (vi) hypertension, (vii) smoking, (viii) data type, (ix) magnetic resonance imaging, (x) CT, (xi) X-ray, (xii) PET, (xiii) US, (xiv) multicenter, (xv) application, (xvi) field of view (FOV), and (xvii) UNet type. The *second cluster* (A10-A16) of AI-based attributes are the *nine architecture parameters* used in the DL study. These are the (i) encoder layer, (ii) decoder layer, (iii) convolution type, (iv) maxpooling type, (v) loss function (LF) was done or not, (vi) LF type, (vii) optimizer type, (viii) filter size, and (ix) bridge network type. The *third cluster* (A17-A28) of attributes includes the *performance evaluation parameters* such as (i) number of PE parameters, (ii) sensitivity, (iii) specificity, (iv) accuracy, (v) precision, (vi) F1-score, (vii) P-value, (viii) hamming loss, (ix) Dice coefficient, (x) Jaccard-index, (xi) Mathew’s correlation coefficient (MCC), (xii) positive predictive value (PPV), and (xiii) Hausdorff surface distance (HSD). The *last and fourth cluster* (A29-A35) consists of ten *benchmarking and clinical validation parameter* attributes. These include the (i) statistical analysis, (ii) power analysis, (iii) scientific validation, (iv) benchmarking, (v) hazard analysis, (vi) survival analysis,

(vii) paired t-test, (viii) Kruskal-Wallis test, and (ix) FDA approval.

C. REGIONAL-BIAS AREA METHOD

The regional-bias area (RBA) was estimated by evaluating the difference in the area of the best DL performing attributes and the worst performing DL attributes. Figure 44 (left) displays the RBA for every vascular study, while Figure 44 (right) shows for the non-vascular studies in the increasing order of the area of bias (white region). In each of the studies bias is depicted as: “Sn-Name: BiasValue”. For example, in the non-vascular application, “S18-Che:149”, where “18” represents the study number, “Che” is the first three letters of the last name of the first author in the study, and “149” represents the normalized value of the bias. The greater white shaded area, the grater the area corresponding to bias.

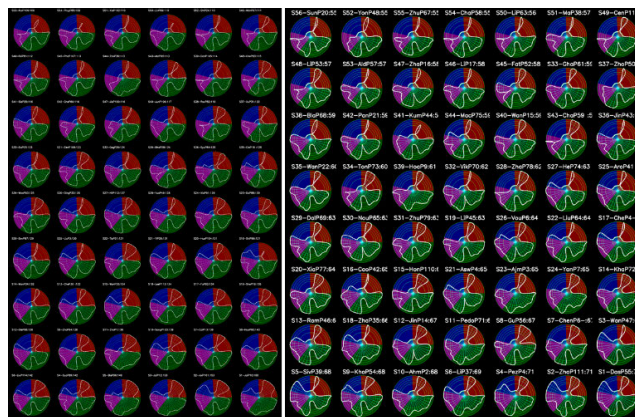


FIGURE 43. Radial-bias Map; Left: Vascular studies; Right: Non-vascular studies.

D. ROBINS-I

This bias estimation approach aims to imitate non-randomized trials’ randomization. RoB is studied using three intervention components namely, “Pre-Intervention,” “During Intervention,” and “post-Intervention. These three components are further spanned to seven distinct aspects, namely, (i) bias due to confounding (total patients, risk factor, and demographic), (ii) bias in selection of participants (image modality, multicenter, and data type), (iii) bias in classification of interventions (UNet type, model layers, conv. type, loss type, and optimizer), (iv) bias due to deviations from intended interventions (application, and benchmarking), (v) bias due to missing data (FOV Application),” (vi) bias in measurement of outcomes (accuracy, Dice, Jaccard, MCC, and HSD), and (vii) bias in selection of the reported result (statistical analysis, scientific validation, and XAI) (Table 12 and 13). We used the ROBINS-I tool on a total of 54 and 56 studies of the vascular and non-vascular domains, respectively. Using the low bias cut-off of 3.1 and 2.9, the moderate-high bias cut-off of 2.6 and 2.6 for vascular and non-vascular, respectively. We found that 29.62%

TABLE 10. Non-vascular radial and area.

		S1-DusP55	S2-ZhaP111	S3-WanP47	S4-PezP4	S5-SivP39	S6-LiP3	S7-ChenP60	S8-GuP56	S9-KhoP54	S10-AhmP2	S11-PedoP71	S12-JinP14	S13-RamP46	S14-KhaP72	S15-HonP110	S16-CaoP42	S17-CheP4	S18-ZhaP35	S19-LiP45	S20-XiaP77
A1	TP	1	0.6	1	0.6	1	1	1	1	1	1	1	0.8	0.6	1	1	1	1	0.6	1	0.6
A2	RF	0.25	0.25	0.25	0.6	0.25	0.6	0.25	0.25	0.25	0.7	0.8	0.8	0.25	0.25	0.25	0.25	0.25	0.6	0.25	0.25
A3	Demo	0.25	0.25	0.25	0.25	0.25	0.6	0.25	0.25	0.25	0.9	0.6	0.25	0.25	0.25	0.25	0.25	0.25	0.6	0.25	0.25
A4	DT	0.9	0.9	0.9	0.9	0.9	0.9	0.9	0.9	0.9	0.9	0.9	0.9	0.9	0.9	0.9	0.9	0.9	0.9	0.9	0.9
A5	IM	0.8	0.8	0.8	0.8	0.8	0.8	0.8	0.8	0.8	0.8	0.8	0.8	0.8	0.8	0.8	0.8	0.8	0.8	0.8	0.8
A6	Multicentre	0.8	0.8	1	0.8	0.8	0.8	0.8	1	0.8	0.8	0.8	0.8	0.8	0.8	0.8	0.8	0.8	0.8	0.8	1
A7	Application	0.9	0.9	0.9	0.9	0.9	0.9	0.9	0.9	0.9	0.9	0.9	0.9	0.9	0.9	0.9	0.9	0.9	0.9	0.9	0.9
A8	FOV (Application)	0.8	0.8	0.8	0.8	0.8	0.8	0.8	0.8	0.8	0.8	0.8	0.8	0.8	0.8	0.8	0.8	0.8	0.8	0.8	0.8
A9	UNet Type	1	0.9	1	0.9	0.7	0.8	0.9	1	1	0.9	0.9	0.9	1	1	0.9	1	0.9	0.9	1	0.9
A10	Encoder layer	0.8	1	0.9	0.8	0.8	0.8	1	1	1	0.8	0.9	0.8	1	0.9	0.9	1	0.8	0.8	0.9	1
A11	Decoder layer	0.8	1	0.9	0.8	0.8	0.8	1	1	1	0.8	0.9	0.8	1	0.9	0.9	1	0.8	0.8	0.9	1
A12	Convolution Type	0.8	0.8	0.8	0.8	0.8	0.8	0.8	0.8	0.8	0.8	0.8	0.8	0.8	0.8	0.8	0.9	0.8	0.8	0.8	0.8
A13	Loss Type	1	0.6	0.9	1	0.9	1	1	1	0.6	0.9	0.9	0.9	1	1	0.9	1	0.9	0.9	0.9	0.9
A14	Optimizer	1	0.6	1	1	1	1	1	1	0.6	1	1	1	1	1	0.6	1	1	1	1	1
A15	Filter Size	0.8	0.7	0.9	0.9	0.7	0.9	0.8	0.8	0.7	0.7	0.7	0.8	0.8	0.7	0.9	0.9	0.8	0.8	0.9	0.7
A16	Br NW Type	0.8	0.8	0.8	0.8	0.8	0.8	0.8	0.8	0.8	0.8	0.8	0.8	0.8	0.8	0.9	0.8	0.8	0.8	0.8	0.8
A17	# PE	1	1	1	1	1	1	0.9	1	0.7	1	0.8	0.8	0.8	0.9	0.8	1	1	0.9	1	0.7
A18	SEN	1	0.25	1	0.8	1	0.25	0.25	0.25	0.9	1	0.9	0.25	1	0.25	0.25	0.7	0.25	0.25	0.25	0.25
A19	SPEC (%)	1	0.25	1	1	1	0.25	0.25	0.25	1	1	0.9	0.25	0.25	0.25	0.25	0.25	1	0.25	0.25	0.25
A20	ACC (%)	1	1	1	1	1	0.25	0.9	0.25	1	1	0.9	0.25	0.25	1	1	0.25	0.25	0.9	0.25	0.25
A21	PREC (%)	1	1	0.25	0.8	1	1	0.25	0.25	1	0.25	0.25	0.25	0.25	0.25	0.25	0.8	1	0.9	0.25	0.25
A22	F1-Score (%)	0.25	1	0.25	0.8	1	1	0.25	0.25	0.9	0.25	0.25	0.25	0.25	0.25	0.25	0.25	0.25	0.25	0.25	0.25
A23	P-value	0.25	0.25	0.25	0.25	0.25	0.25	0.25	0.25	0.25	0.25	0.25	1	0.25	0.25	0.25	0.25	0.25	0.25	0.25	0.25
A25	DICE (%)	0.25	1	1	1	1	1	0.9	1	0.25	0.25	0.25	0.9	0.9	1	1	0.7	1	0.9	1	0.9
A26	Jaccard	0.25	1	1	0.25	0.25	1	0.25	0.25	0.25	0.25	0.25	0.9	0.8	0.7	0.25	0.6	1	0.8	0.25	0.25
A27	MCC	1	0.25	0.25	0.25	0.25	0.25	0.25	0.25	0.25	0.25	0.25	0.25	0.25	0.25	0.25	0.25	0.25	0.25	0.25	0.25
A28	PPV	1	0.25	0.25	0.25	0.25	0.25	0.25	0.25	0.25	0.25	0.25	0.25	0.25	0.25	0.25	0.25	0.25	0.25	0.25	0.25
A29	Hausdorff S. Distance (HSD)	0.25	1	0.25	0.25	0.25	0.25	1	1	0.25	0.25	0.25	0.25	1	0.25	0.25	1	0.25	0.25	1	1
A30	Statistical Analysis	1	1	1	1	1	1	1	1	1	1	1	1	1	1	1	1	1	1	1	1
A31	Power Analysis	0.25	0.25	0.25	1	0.25	0.25	0.25	0.25	1	0.25	0.25	0.25	0.25	0.25	0.25	0.25	0.25	0.25	0.25	0.25
A32	Sci. Validation	1	1	0.25	1	0.25	1	1	1	1	1	1	1	1	1	1	0.25	0.25	0.25	1	1
A33	Benchmarking	0.9	0.8	0.8	0.6	0.9	0.9	0.8	0.6	1	0.6	0.6	0.9	0.8	0.8	1	0.6	0.7	0.8	0.7	0.6
A34	Paired t-test	0.25	0.25	0.25	0.25	0.25	0.25	0.25	0.25	0.25	0.25	0.25	1	0.25	0.25	0.25	0.25	0.25	0.25	0.25	0.25
A35	XAI	0.25	1	0.25	0.25	0.25	0.25	1	1	0.25	0.25	1	0.25	0.25	1	1	0.25	0.25	0.25	0.25	1
A36	Clinical Setting	0.25	0.25	0.25	0.25	0.25	0.25	0.25	1	0.25	0.25	0.25	0.25	0.25	0.25	0.25	0.25	0.25	0.25	0.25	0.25

TABLE 10. (Continued.) Non-vascular radial and area.

S21-AsvP4	S22-LiuP6	S23-AjnpP3	S24-YanP7	S25-AroP4	S26-VouP6	S27-HepP7	S28-ZhaP8	S29-DaiP9	S30-NouP5	S31-ZhuP7	S32-VikP7	S33-GhaP6	S34-TomP7	S35-WanP2	S36-JinP4	S37-ZhoP5	S38-BlaP6	S39-HoaP9	S40-WanP5	S41-KunP4	S42-PanP2	S43-ChaP5	S44-MacP7	S45-FatP5	S46-LiP17	S47-ZhaP6	S48-LiP3	S49-CenP1	S50-LiP6	S51-MaP3	S52-YouP4	S53-AldP5	S54-ChaP5	S55-ZhuP6	S56-SunP2				
0.6	1	1	0.7	0.6	0.6	0.6	0.6	0.6	0.7	0.6	1	0.6	0.9	0.7	0.6	1	1	0.6	0.6	1	0.7	0.6	0.6	0.6	0.6	0.6	0.6	0.6	0.6	0.6	0.6	0.6	0.6	0.6	0.6	0.6	0.6		
0.6	0.25	0.7	0.6	0.25	0.6	0.25	0.25	0.25	0.25	0.25	0.25	0.25	0.25	0.25	0.25	0.25	0.6	0.25	0.25	0.25	0.25	0.25	0.25	0.25	0.25	0.25	0.25	0.25	0.25	0.25	0.25	0.25	0.25	0.25	0.25	0.25	0.25		
0.9	0.9	0.9	0.9	0.9	0.9	0.9	0.9	0.9	0.9	0.9	0.9	0.9	0.9	0.9	0.9	0.9	0.9	0.9	0.9	0.9	0.9	0.9	0.9	0.9	0.9	0.9	0.9	0.9	0.9	0.9	0.9	0.9	0.9	0.9	0.9	0.9	0.9		
0.9	0.8	0.8	0.8	0.8	0.8	0.8	0.8	0.8	0.8	0.8	0.8	0.8	0.8	0.8	0.8	0.8	0.8	0.8	0.8	0.8	0.8	0.8	0.8	0.8	0.8	0.8	0.8	0.8	0.8	0.8	0.8	0.8	0.8	0.8	0.8	0.8	0.8	0.8	
0.8	0.8	0.8	1	1	0.8	0.8	0.8	0.8	0.8	0.8	0.8	0.8	0.8	0.8	0.8	1	0.8	0.8	0.8	0.8	0.8	0.8	0.8	0.8	1	0.8	0.8	0.8	0.8	0.8	0.8	0.8	0.8	0.8	0.8	0.8	0.8	0.8	
0.9	0.9	0.9	0.9	0.9	0.9	0.9	0.9	0.9	0.9	0.9	0.9	0.9	0.9	0.9	0.9	0.9	0.9	0.9	0.9	0.9	0.9	0.9	0.9	0.9	0.9	0.9	0.9	0.9	0.9	0.9	0.9	0.9	0.9	0.9	0.9	0.9	0.9	0.9	
0.8	0.8	0.8	0.8	0.8	0.8	0.8	0.8	0.8	0.8	0.8	0.8	0.8	0.8	0.8	0.8	0.8	0.8	0.8	0.8	0.8	0.8	0.8	0.8	0.8	0.8	0.8	0.8	0.8	0.8	0.8	0.8	0.8	0.8	0.8	0.8	0.8	0.8	0.8	
0.7	0.9	0.9	0.8	0.9	0.9	0.9	1	0.8	0.9	0.9	0.9	0.7	1	1	0.9	0.7	0.8	1	0.9	0.8	0.8	0.8	0.8	0.8	1	0.7	0.8	1	0.9	0.9	1	0.9	0.9	1	0.9	0.9	1	0.8	
0.8	0.9	0.8	0.8	1	0.8	0.8	1	0.9	0.9	0.9	0.9	0.9	0.9	0.8	1	0.9	0.7	0.8	0.8	0.9	0.8	0.8	0.9	0.25	0.9	0.9	0.8	0.8	0.8	0.8	0.8	0.8	0.9	0.8	1	0.9	0.8	0.8	
0.8	0.8	0.8	0.8	1	0.8	0.8	1	0.9	0.9	0.9	0.9	0.9	0.8	1	0.9	0.7	0.8	0.8	0.9	0.8	0.8	0.9	0.25	0.9	0.9	0.8	0.8	0.8	0.8	0.8	0.8	0.9	0.8	1	0.9	0.8	0.8	0.8	
0.8	0.8	0.8	0.8	0.8	0.8	0.8	0.8	0.8	0.8	0.8	0.8	0.8	0.8	0.8	0.8	0.8	0.8	0.8	0.8	0.8	0.8	0.8	0.8	0.8	0.8	0.8	0.8	0.8	0.8	0.8	0.8	0.8	0.8	0.8	0.8	0.8	0.8	0.8	0.8
0.9	0.9	0.9	0.9	0.9	0.9	0.9	1	0.9	0.9	0.9	0.9	0.9	0.9	0.9	0.9	0.9	0.9	0.9	0.9	0.9	0.9	0.9	0.9	0.9	0.9	0.9	0.9	0.9	0.9	0.9	0.9	0.9	0.9	0.9	0.9	0.9	0.9	0.9	
1	1	1	1	1	1	1	1	1	0.6	1	1	1	1	1	0.6	1	1																						

TABLE 12. Vascular ROBINS-I.

SN	Author	P.No	Pre-Intervention		At-intervention	Post-intervention				Total	Mean	Cumm	Rank
			Bias due to confounding	Bias in selection of participants into the study	Bias in classification of interventions	Bias due to deviations from intended interventions	Bias due to missing data	Bias in measurement of outcomes	Bias in selection of the reported result				
1	Jain1 et al.	P10	3.3	4.0	4.2	3.5	5.0	2.0	3.3	25.4	3.6	3.62	1
2	Jain2 et al.	P12	3.0	3.3	4.6	3.5	5.0	2.4	3.3	25.2	3.6	7.22	2
3	Zhou et al.	P1	2.7	3.3	4.2	3.0	5.0	1.8	5.0	25.0	3.6	10.79	3
4	Guo et al.	P89	1.7	4.0	3.8	4.0	4.0	1.8	5.0	24.3	3.5	14.26	4
5	Liu et al.	P114	1.7	4.0	4.0	4.5	4.0	1.0	5.0	24.2	3.5	17.71	5
6	Song et al.	P103	1.7	2.3	3.8	4.5	4.0	2.8	5.0	24.1	3.4	21.15	6
7	Biswas et al.	P96	2.3	3.3	4.2	4.0	4.0	1.0	5.0	23.9	3.4	24.56	7
8	Huang et al.	P90	1.7	4.0	4.2	4.0	4.0	1.0	5.0	23.9	3.4	27.97	7
9	Zhang et al.	P94	1.7	4.0	4.6	3.5	4.0	1.0	5.0	23.8	3.4	31.37	9
10	Jain et al.	P101	1.3	2.3	4.0	4.5	4.0	2.4	5.0	23.6	3.4	34.73	10
11	Fu et al.	P92	1.7	4.0	4.0	3.0	4.0	1.6	5.0	23.3	3.3	38.06	11
12	Cai et al.	P13	1.7	4.3	4.2	2.0	4.0	1.8	5.0	23.0	3.3	41.34	12
13	Tianshu Zhou et al.	P51	0.3	3.3	4.4	2.5	5.0	1.8	5.0	22.4	3.2	44.54	13
14	Lee et al.	P113	1.7	2.3	3.0	4.5	4.0	1.8	5.0	22.3	3.2	47.72	14
15	Xiao et al.	P91	1.7	4.0	4.0	2.5	4.0	1.0	5.0	22.2	3.2	50.89	15
16	Wang et al.	P32	0.3	3.3	4.0	3.5	5.0	3.8	1.7	21.6	3.1	53.98	16
17	Shen et al.	P19	1.7	4.0	2.8	2.5	4.0	1.0	5.0	21.0	3.0	56.98	17
18	Yi et al.	P26	1.7	3.3	4.0	3.5	4.0	2.8	1.7	21.0	3.0	59.97	17
19	Woo et al.	P93	1.7	4.0	3.2	2.5	4.0	0.6	5.0	21.0	3.0	62.97	17
20	Chen et al.	P30	1.7	4.0	4.0	4.5	4.0	1.0	1.7	20.8	3.0	65.94	20
21	Du et al.	P88	1.7	4.0	4.0	2.5	4.0	1.0	3.3	20.5	2.9	68.87	21
22	Wang et al.	P34	1.7	4.0	4.0	4.0	4.0	1.0	1.7	20.3	2.9	71.78	22
23	Hussain et al.	P104	1.7	2.3	4.2	3.0	4.0	1.8	3.3	20.3	2.9	74.68	23
24	Yuan et al.	P49	0.3	4.0	4.2	3.5	4.0	2.6	1.7	20.3	2.9	77.58	24
25	Xu et al.	P31	2.0	3.3	3.6	4.0	4.0	1.6	1.7	20.2	2.9	80.47	25
26	Olender et al.	P98	0.3	3.3	4.0	2.5	4.0	1.0	5.0	20.2	2.9	83.35	26
27	Ravichandran et al.	P82	0.3	3.3	3.4	3.5	4.0	0.6	5.0	20.2	2.9	86.23	27
28	Hilbert et al.	P112	0.3	2.3	4.2	3.5	4.0	2.0	3.3	19.7	2.8	89.04	28
29	David et al.	P87	1.7	4.0	3.8	2.5	4.0	2.0	1.7	19.6	2.8	91.85	29
30	Zhou et al.	P36	2.7	3.3	3.6	3.0	5.0	0.0	1.7	19.3	2.8	94.60	30
31	Zeng et al.	P108	0.3	2.3	3.2	3.5	4.0	0.8	5.0	19.2	2.7	97.34	31
32	Liu et al.	P3	2.0	4.0	3.8	2.5	4.0	1.0	1.7	19.0	2.7	100.05	32
33	Dong et al.	P105	1.7	2.3	4.2	4.0	4.0	1.0	1.7	18.9	2.7	102.74	33
34	Chen et al.	P83	0.3	3.3	2.8	2.5	4.0	0.8	5.0	18.8	2.7	105.42	34
35	Abraham et al.	P95	1.7	2.3	4.2	4.0	4.0	0.8	1.7	18.7	2.7	108.09	35
36	Gegundez-Arias et al.	P29	1.7	4.0	3.8	2.5	4.0	1.0	1.7	18.6	2.7	110.75	36
37	Du et al.	P23	1.7	4.0	3.8	2.5	4.0	1.0	1.7	18.6	2.7	113.41	36
38	Cheung et al.	P80	0.3	3.3	4.2	2.5	5.0	1.4	1.7	18.4	2.6	116.05	38
39	SyuanPan et al.	P84	0.3	3.3	3.4	2.5	4.0	1.4	3.3	18.3	2.6	118.66	39
40	Wang et al.	P97	1.7	2.3	4.2	4.0	4.0	0.4	1.7	18.3	2.6	121.27	40
41	Bhatia et al.	P28	1.7	4.0	3.2	2.5	4.0	1.0	1.7	18.0	2.6	123.85	41
42	Shinohara et al.	P86	1.7	3.3	4.2	2.5	4.0	2.2	0.0	17.9	2.6	126.40	42
43	Ding et al.	P33	1.7	3.3	3.4	2.5	4.0	1.0	1.7	17.6	2.5	128.91	43
44	Pham et al.	P107	1.7	2.3	3.6	3.5	4.0	0.2	1.7	17.0	2.4	131.34	44
45	Feiger et al.	P81	0.3	3.3	4.0	2.5	4.0	1.0	1.7	16.8	2.4	133.74	45
46	Claux et al.	P18	0.7	3.3	3.8	2.5	4.0	0.6	1.7	16.6	2.4	136.11	46
47	Jiang et al.	P100	1.3	2.3	4.0	2.5	4.0	0.6	1.7	16.4	2.3	138.46	47
48	Sieren et al.	P25	0.3	3.3	2.8	2.0	4.0	2.0	1.7	16.1	2.3	140.76	48
49	Shi et al.	P24	0.3	3.3	2.8	3.0	4.0	1.0	1.7	16.1	2.3	143.07	48
50	Rui wang et al.	P109	1.7	2.3	4.0	3.5	4.0	0.6	0.0	16.1	2.3	145.37	50
51	Jun et al.	P106	0.3	2.3	4.0	2.5	4.0	0.8	1.7	15.6	2.2	147.60	51
52	Xie et al.	P102	0.3	2.3	2.8	2.5	4.0	1.8	1.7	15.4	2.2	149.80	52
53	Livne et al.	P99	0.3	2.3	4.0	2.5	4.0	1.8	0.0	15.0	2.1	151.94	53
54	Thuy et al.	P85	0.3	3.3	2.8	2.5	4.0	2.0	0.0	15.0	2.1	154.08	54

TABLE 13. Non-vascular ROBINS-I.

SN	Author	P.No	Pre-intervention		At-intervention	Post-intervention				Total	Mean	Cumm	Rank
			Bias due to confounding	Bias in selection of participants into the study	Bias in classification of interventions	Bias due to deviations from intended interventions	Bias due to missing data	Bias in measurement of outcomes	Bias in selection of the reported result				
1	Chen <i>et al.</i>	P60	1.7	3.3	4.4	3.5	3.0	2.6	5.0	23.5	3.4	3.36	1
2	Khattab <i>et al.</i>	P72	1.7	3.3	4.4	3.5	3.0	2.4	5.0	23.3	3.3	6.69	2
3	Hong <i>et al.</i>	P110	1.7	3.3	3.2	4.5	3.0	2.0	5.0	22.7	3.2	9.93	3
4	Gu <i>et al.</i>	P56	1.7	4.0	4.4	2.5	3.0	2.0	5.0	22.6	3.2	13.15	4
5	Zhao <i>et al.</i>	P111	0.3	3.3	2.8	3.5	3.0	4.0	5.0	22.0	3.1	16.29	5
6	Li <i>et al.</i>	P37	2.3	3.3	3.8	4.0	3.0	2.0	3.3	21.8	3.1	19.40	6
7	Pedoia <i>et al.</i>	P71	3.0	3.3	4.0	2.5	3.0	0.8	5.0	21.6	3.1	22.50	7
8	Das <i>et al.</i>	P55	1.7	3.3	4.2	4.0	3.0	2.0	3.3	21.5	3.1	25.57	8
9	Li <i>et al.</i>	P45	1.7	4.0	4.2	3.0	3.0	2.0	3.3	21.2	3.0	28.60	9
10	Jin <i>et al.</i>	P14	2.0	3.3	3.8	4.0	3.0	1.6	3.3	21.1	3.0	31.61	10
11	Wang <i>et al.</i>	P47	1.7	4.0	4.2	3.5	3.0	3.0	1.7	21.0	3.0	34.61	11
12	Xianxiang <i>et al.</i>	P77	0.3	4.0	4.2	2.5	3.0	1.8	5.0	20.8	3.0	37.59	12
13	Ahmed <i>et al.</i>	P2	3.7	3.3	3.8	2.5	3.0	1.0	3.3	20.6	2.9	40.54	13
14	Rampun <i>et al.</i>	P46	0.3	3.3	4.6	3.5	3.0	2.4	3.3	20.5	2.9	43.47	14
15	Zhu <i>et al.</i>	P79	0.3	3.3	4.0	3.0	3.0	1.8	5.0	20.5	2.9	46.39	15
16	Arora <i>et al.</i>	P41	0.3	4.0	4.0	4.0	3.0	3.0	1.7	20.0	2.9	49.25	16
17	Zhang <i>et al.</i>	P78	0.3	3.3	4.2	3.0	3.0	1.0	5.0	19.9	2.8	52.09	17
18	Khoong <i>et al.</i>	P54	1.7	3.3	3.0	4.5	3.0	1.0	3.3	19.8	2.8	54.92	18
19	Tong <i>et al.</i>	P73	1.3	3.3	4.0	2.5	3.0	0.6	5.0	19.8	2.8	57.74	19
20	Nour <i>et al.</i>	P65	1.0	3.3	3.0	4.5	3.0	3.2	1.7	19.7	2.8	60.56	20
21	Sivagami <i>et al.</i>	P39	1.7	3.7	3.4	4.0	3.0	2.0	1.7	19.4	2.8	63.33	21
22	Liu <i>et al.</i>	P64	1.7	3.3	4.0	3.5	3.0	2.2	1.7	19.4	2.8	66.10	22
23	Yang <i>et al.</i>	P7	1.3	4.0	3.8	3.5	3.0	0.4	3.3	19.4	2.8	68.86	23
24	Ghavmi <i>et al.</i>	P61	0.3	3.7	4.0	4.5	3.0	1.8	1.7	19.0	2.7	71.57	24
25	Ajmera <i>et al.</i>	P3	3.0	3.3	3.8	2.5	3.0	0.0	3.3	19.0	2.7	74.28	25
26	Wang <i>et al.</i>	P15	0.3	4.0	2.8	3.5	3.0	2.0	3.3	19.0	2.7	76.99	25
27	Pezzano <i>et al.</i>	P4	0.7	3.3	4.0	2.5	3.0	2.0	3.3	18.8	2.7	79.68	27
28	Chang <i>et al.</i>	P59	0.3	3.3	3.6	2.5	3.0	1.0	5.0	18.8	2.7	82.36	28
29	Hoang thi <i>et al.</i>	P9	1.0	4.0	3.4	2.5	4.0	0.4	3.3	18.6	2.7	85.02	29
30	Cao <i>et al.</i>	P42	1.7	3.3	4.8	2.5	3.0	1.6	1.7	18.6	2.7	87.68	30
31	Zhang <i>et al.</i>	P35	1.0	3.3	3.8	3.5	3.0	2.2	1.7	18.5	2.6	90.32	31
32	Chen <i>et al.</i>	P40	1.7	3.3	3.8	3.0	3.0	2.0	1.7	18.5	2.6	92.96	32
33	Aswathy <i>et al.</i>	P4	0.7	3.7	3.4	2.5	3.0	1.8	3.3	18.4	2.6	95.58	33
34	Voulodimos <i>et al.</i>	P6	0.7	3.3	3.8	2.5	3.0	1.6	3.3	18.2	2.6	98.19	34
35	Wang <i>et al.</i>	P22	0.7	3.3	3.4	4.5	3.0	1.4	1.7	18.0	2.6	100.75	35
36	Zhou <i>et al.</i>	P50	1.7	3.3	4.4	3.5	3.0	0.4	1.7	18.0	2.6	103.32	35
37	Li <i>et al.</i>	P63	1.7	3.3	3.8	3.5	3.0	0.8	1.7	17.8	2.5	105.86	37
38	Li <i>et al.</i>	P53	0.3	4.0	4.0	2.5	3.0	0.6	3.3	17.8	2.5	108.40	38
39	He <i>et al.</i>	P74	0.3	3.3	4.0	3.5	3.0	1.8	1.7	17.6	2.5	110.91	39
40	Jin <i>et al.</i>	P43	0.3	3.3	3.6	2.5	3.0	3.0	1.7	17.4	2.5	113.40	40
41	Cendejas-Zaragoza <i>et al.</i>	P11	0.7	3.3	4.0	2.0	3.0	1.0	3.3	17.3	2.5	115.88	41
42	Viksit <i>et al.</i>	P70	2.0	3.3	4.0	2.5	3.0	0.8	1.7	17.3	2.5	118.35	42
43	Fatemah <i>et al.</i>	P52	0.3	3.3	3.4	2.5	3.0	0.8	3.3	16.7	2.4	120.74	43
45	Li <i>et al.</i>	P17	0.3	4.0	3.6	3.0	3.0	0.8	1.7	16.4	2.3	123.08	44
46	Kumar <i>et al.</i>	P44	1.7	3.3	4.4	3.5	3.0	0.4	0.0	16.3	2.3	125.41	45
47	Pan <i>et al.</i>	P21	1.0	3.3	3.8	2.5	3.0	1.0	1.7	16.3	2.3	127.74	45
48	Blanc-Durand <i>et al.</i>	P68	1.7	3.3	3.6	2.0	3.0	0.8	1.7	16.1	2.3	130.03	47
49	Aldoz <i>et al.</i>	P57	0.3	3.3	3.2	2.5	3.0	2.0	1.7	16.0	2.3	132.32	48
50	Sun <i>et al.</i>	P20	0.3	4.0	3.0	3.0	3.0	1.0	1.7	16.0	2.3	134.61	49
51	Yong <i>et al.</i>	P48	1.3	3.3	4.4	2.0	3.0	0.2	1.7	15.9	2.3	136.89	50
52	Ma <i>et al.</i>	P38	0.3	3.3	3.2	2.5	3.0	1.8	1.7	15.8	2.3	139.15	51
53	Dalmis <i>et al.</i>	P69	0.3	3.3	4.2	3.0	3.0	0.0	1.7	15.5	2.2	141.37	52
54	Chahal <i>et al.</i>	P58	0.3	3.3	3.4	2.5	3.0	1.0	1.7	15.2	2.2	143.54	53
55	Zhang <i>et al.</i>	P16	0.7	3.3	3.0	3.5	3.0	0.0	1.7	15.2	2.2	145.71	54
56	Zhu <i>et al.</i>	P67	0.3	3.3	3.4	2.5	3.0	0.8	1.7	15.0	2.1	147.86	55
57	Machireddy <i>et al.</i>	P75	0.3	3.3	3.0	2.0	3.0	0.6	1.7	13.9	2.0	149.85	56

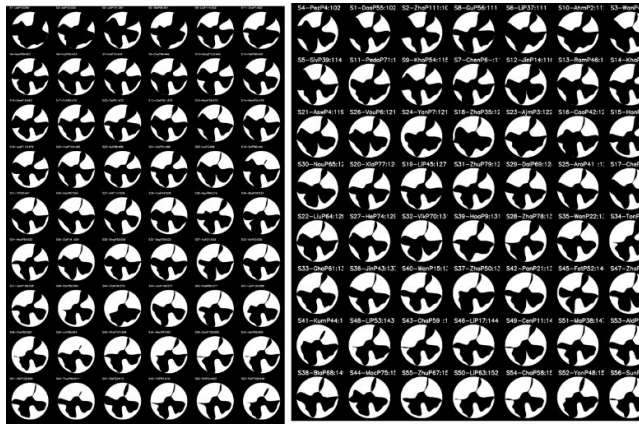


FIGURE 44. Regional-bias Area; Left: Vascular studies; Right: Non-vascular studies.

ROBINS-I were 36 (66.67%), 47 (87.03%), 37 (65.85%), 42 (77.78%), and 38 (70.37%), respectively. The studies that fall under the intersection of *low-bias 0* and *moderate-high-bias 17* for the five innovative methods.

In the non-vascular paradigm, the number of studies in *low-bias* for RBS, RBM, RBA, PROCAST, and ROBINS-I were 5 (8.9%), 16 (28.57%), 13 (23.21%), 14 (25%), and 16 (28.57%) respectively, the remaining studies under *moderate-high-bias* for RBS, RBM, RBA, PROCAST, and ROBINS-I were 51 (91.1), 40 (71.42%), 43 (76.78%), 42 (75%), and 40 (71.42%), respectively. The studies that fall under the intersection of *low-bias 0* and *moderate-high-bias 16* for the three innovative methods.

X. CRITICAL DISCUSSION

A. PRINCIPAL FINDINGS

In particular, medical imaging has undergone a wave of revolution in the last five years in the field of segmentation. Since the introduction of cUNet, there have been nearly 1000 UNet publications. However, the understanding of such black boxes is still not felt to the level where the physicians are comfortable and confident to adopting them in clinical settings. We therefore took one level deeper, offering the following novelties: (i) understanding the statistical distribution post PRISMA-based study selection, (ii) segregating the UNet and its variations into *five* clear classes (cUNet, sUNet, acUNet, hUNet and eUNet), giving their distinguishing characteristics along with the applications. (iii) The latest and most powerful features of deep learning, such as convolution, max/average pooling, and 81 critical modifications in encoder, decoder, skip connection, and classification frameworks to get the best low-level and high-level features, are now better explained. (iv) Also, segmentation challenges-architecture solutions-key were provided. Further, we link these UNet extraction paradigms with the novel AI necessities such as (v) pruning, (vi) explainable AI, and (vii) AI bias, which are also our novel and unique contributions. (viii) our review covers the state-of-the-art references with powerful vascular and non-vascular applications.

B. BENCHMARKING

The main coverage of 2020 was the modification of basic cUNet, invented in 2015. Since then, we have had inventions related to the UNet series leading to into UNet+, UNet++, UNet+ + +, ZNet, TNet, and WNet (UNet+UNet) [85], [144], [157]. There are five major components in this small segmentation structure: encoder, decoder, skip connection, bridge network, and termination layer for ensuring either accomplishing segmentation or classification. Such a UNet structure can be changed using a bag of tools such as filter deck (channels), convolution, max pooling, ReLU, and fusion of classifiers for handling the spatial and temporal information to compensate for handling scale, space, position, and size in 2D/3D. Keeping the above paradigms in mind, we have only taken the critical UNet reviews from 2020, 2021, and 2022 (Table 16). Note that there was no review of UNet between 2015 and 2020. One reason was due to “Inertia of Education”, which there was a lag of five years since UNet was first invented in 2015. Note, Liu et al. [177], Siddique et al. [246], and Du et al. [247] were the only first three UNet reviews in 2020, and since then, the problem-solving tools have evolved along with the challenges. Furthermore, the previous methods like level sets, and classifiers were either user-interactive or computationally expensive and still not fully automated.

Even though the cUNet took a sophisticated turn by undergoing modifications in the five components, we would like to emphasize that the black box nature of AI is unaddressed. Further, in the spirit of generality AI training models are typically larger in size and storage, which makes them nearly impossible to install on edge devices like the RaspberryPi or JetsonNano, and these are the devices of the future. The third aspect of AI models is susceptible to bias due to data size, balance of classes, inconsistencies and missing values in data, image acquisition protocol variations, and architecture compatibility with the input data sets, cross-validation protocols in seen and unseen AI models. All the three major components of AI models are not discussed in the above reviews and therefore offer limitations of the above reviews. We have taken special care to address the above issues in our review. Note that, besides addressing the above issues, we classify the UNet series into five categories, namely cUNet, sUNet, acUNet, hUNet, and eUNet, in a special way by studying all types of applications, modalities, and architectures. The importance of these changes is discussed along with their origin.

In comparison to the UNet reviews published in 2021, these were specifically focused on (i) radiation therapy planning [248], (ii) breast tumor cell nuclei segmentation [249], and (iii) detection and segmentation of tumors in orthopedics applications [250]. Thus, these reviews do not offer strong comparisons with other techniques due to lack of generalization. In 2022, the following review articles were published, namely, Punn et al. [251], Yin et al. [252], He et al. [253], and Wu et al. [254]. Punn et al. [251] covered the same set of UNets (inception, ensemble, attention) for all the different

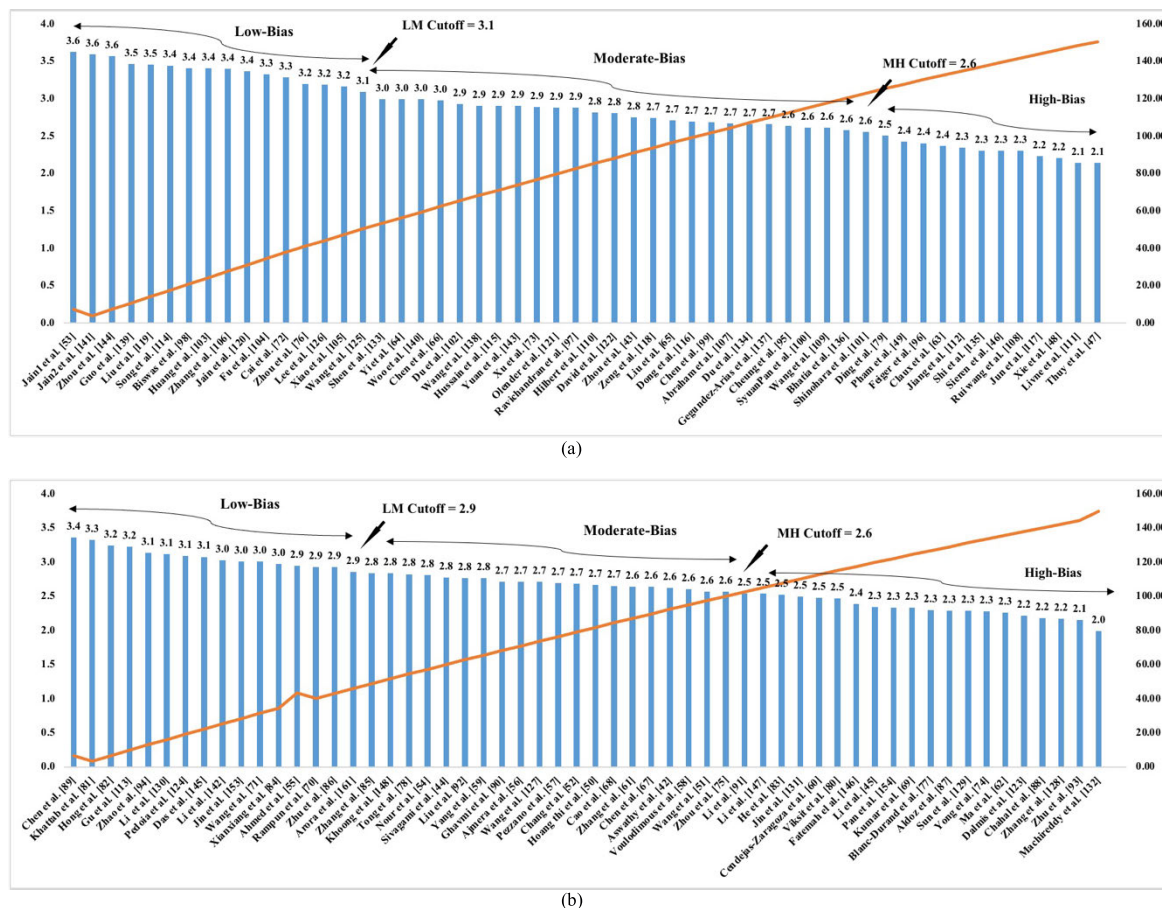


FIGURE 45. (a). Vascular ROBINs-I (3.1 and 2.6). (b). Non-Vascular ROBINs-I (2.9 and 2.6).

modalities, which does not offer design variations, but problems specific to imaging modality and organ segmentation. In Yin et al. [252], the focus was also on the UNet. However, the authors introduced the variety due to transformer based UNet, where the encoder changed to CNN cascaded with the 12 layers of the transformer. Regarding He et al. [253], the authors offered a hybrid UNet unlike reviews in UNet.

This includes the integration of *conditional generative adversarial networks* (Seg-cGAN) with UNet+. Thus, their innovation was to use cGAN for pattern enhancement and introduction of regularization paradigm for capturing context-based image features for segmentation. Wu et al. [254] summarize different developed methods of UNet for microscopic image analysis along with the comparison of UNet techniques used in other studies.

C. RECOMMENDATION

The study offers the following set of recommendations: **(i) Segmentation complexity and UNet selection:** The segmentation complexity and image dimensionality should be considered when selecting a UNet type. Based on scale, shape, position, size, and the noise characteristics, it is recommended to choose an architecture where the UNet

components are altered by several different attention mechanisms; **(ii) UNet hyperparameters optimization:** The choice of hyperparameters plays an important role in UNet optimization. Therefore, it is recommended to optimize the UNet architecture in an iterative paradigm. The hyperparameters include a number of layers in the UNet, filter size during convolution, learning rate, batch normalization, and number of epochs, number of iterations per epoch, and the design of the loss functions; **(iii) Explainability of UNet-based AI system:** All clinical systems using UNet should be explainable or interpretable based on standardized paradigm such as Grad-CAM [179], LIME, and SHAPLEY [255], [256]; **(iv) Clinical Evaluation and Scientific Validation:** The UNet architecture should be clinically evaluated and scientifically validated using previously unseen AI paradigms. This requires the model to be trained on data different from the test data; **(v) Reduction of AI-bias:** For the low bias design of AI system using UNet, all the attributes such as data demographics, architecture components, optimization parameter, and scientific/clinical validation must be taken into account for reduction [32], [34], [242], [243], [244], [257]; **(vi) Generalization vs. Memorization:** The UNet-based design must be generalizable both in terms of data size, and the variability

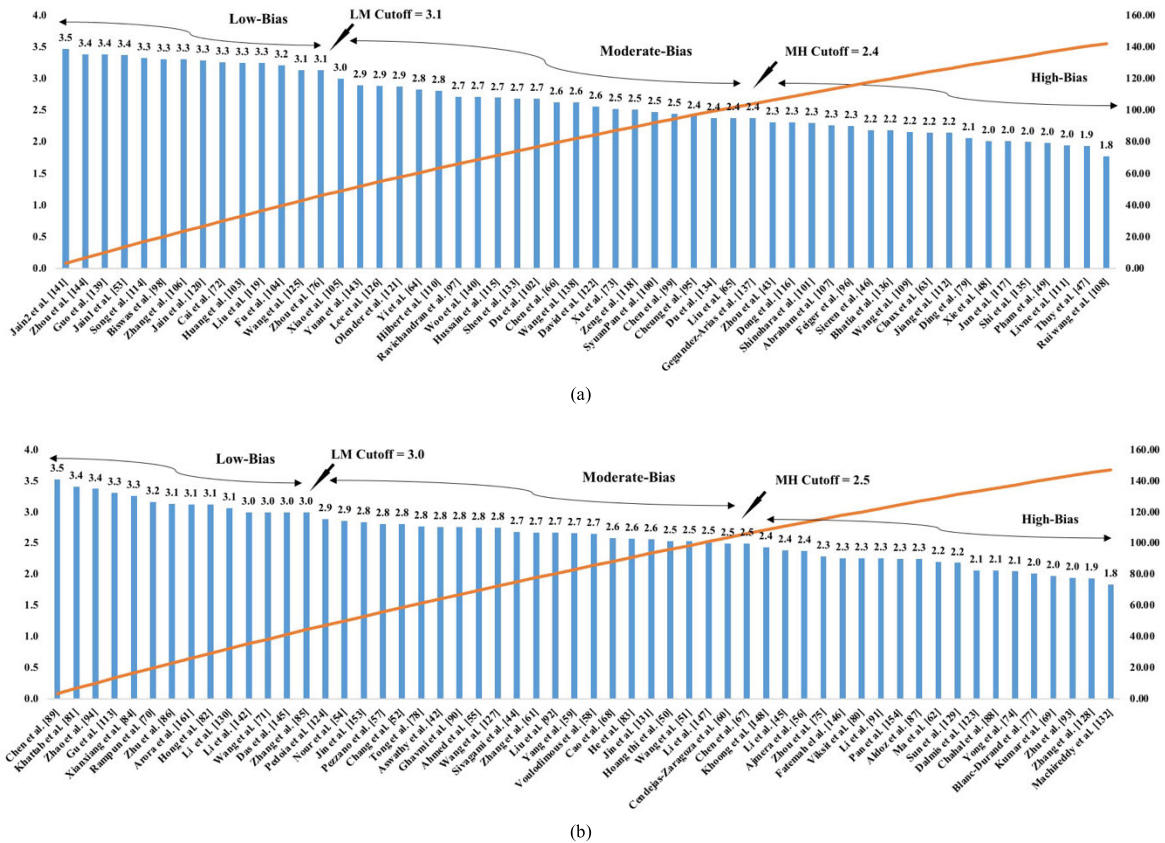


FIGURE 46. (a). Vascular PROBAST (3.1 and 2.4). (b). Non-Vascular PROBAST (3.0 and 2.5).

in the data type. Big data framework can be adapted during training having diversity in the database with best gold standard during supervised learning; (vii) *Miscellaneous*: In healthcare databases, demographics such as comorbidity, and data acquisition must be carefully designed to have the least impact on AI bias and performance.

D. SHORT NOTE ON UNSUPERVISED UNET PARADIGM

Although, the focus of this study was purely and squarely on supervised UNet frameworks, one cannot ignore the upcoming wave and innovation in unsupervised learning or self-learning techniques [258], [259], [260], [261], [262]. The fundamental difference between a supervised and unsupervised paradigms is the incorporation of pseudo gold standard in the form of another observation which is similar to original datasets whose segmentation needs to be determined. Such a pseudo-observation is typically adapted for training the model, exactly the way the gold standard does [164], [263], [264], [265], [266].

E. STRENGTH, WEAKNESS, AND EXTENSION

The system allows selection of the appropriate UNet, given the segmentation challenge. The study provided a set of five types of UNet (cUNet, sUNet, acUNet, hUNet, and eUNet) based on the evolution in the components of the UNet to

handle the complexities of the segmentation process. Thus, the selected UNet is able to appropriately configure the components of the UNet, given the change in shape, size, scale, and position in the images. Further, the study exclusively studied 81 configurations which altered the cUNet, leading to a powerful UNet system for vascular and non-vascular applications. The strength of the system was to study similarities and differences between the vascular and non-vascular UNet-based applications. The review also provides a comparison between the vascular and non-vascular segmentation frameworks. Furthermore, the review also gives an insight into pruning, interpretability, and bias. This was the first time such a UNet paradigm was demonstrated.

Even though, UNet has opened the door for most segmentation challenges, there is a price to pay when it comes to speed, storage, portability on edge devices (Raspberry pi and JetsonNano), and time complexity. As the number of layers in the UNet increases, encoder paradigms change from conventional to residual or dilated convolutions, skip connections are embedded with classifiers such as LSTM or RNN, decoder alterations for fusing the output led to complex loss functions – all these affect the computation time demanding a higher processor such as GPU or multithreaded architecture.

While we have seen nearly 300 UNet variations (some not included in this review) in a very short span of less than

TABLE 14. Vascular PROBAST.

SN	Author	Participants	Predictors	Outcomes	Analysis	Total	Mean	Cumm	Rank
1	Jain2 <i>et al.</i>	3.75	4.5	2.4	3.25	13.9	3.5	3.48	1
2	Guo <i>et al.</i>	3	4	1.8	4.75	13.55	3.4	6.86	2
3	Zhou <i>et al.</i>	3.5	4	1.8	4.25	13.55	3.4	10.25	2
4	Jain1 <i>et al.</i>	4.25	4	2	3.25	13.5	3.4	13.63	4
5	Song <i>et al.</i>	1.75	3.75	2.8	5	13.3	3.3	16.95	5
6	Biswas <i>et al.</i>	3.25	4.25	1	4.75	13.25	3.3	20.26	6
7	Zhang <i>et al.</i>	3	4.75	1	4.5	13.25	3.3	23.58	6
8	Jain3 <i>et al.</i>	1.75	4	2.4	5	13.15	3.3	26.86	8
9	Cai <i>et al.</i>	3.25	4.25	1.8	3.75	13.05	3.3	30.13	9
10	Liu <i>et al.</i>	3	4	1	5	13	3.3	33.38	10
11	Huang <i>et al.</i>	3	4.25	1	4.75	13	3.3	36.63	10
12	Fu <i>et al.</i>	3	4	1.6	4.25	12.85	3.2	39.84	12
13	Wang <i>et al.</i>	2.5	4.25	3.8	2	12.55	3.1	42.98	13
14	Tianshu Zhou <i>et al.</i>	2.5	4.25	1.8	4	12.55	3.1	46.11	13
15	Xiao <i>et al.</i>	3	4	1	4	12	3.0	49.11	15
16	Yuan <i>et al.</i>	3	4	2.6	2	11.6	2.9	52.01	16
17	Lee Aorta	1.75	3	1.8	5	11.55	2.9	54.90	17
18	Olender <i>et al.</i>	2.5	4	1	4	11.5	2.9	57.78	18
19	Yi <i>et al.</i>	2.5	4	2.8	2	11.3	2.8	60.60	19
20	Hilbert <i>et al.</i>	1.75	4.25	2	3.25	11.25	2.8	63.41	20
21	Woo <i>et al.</i>	3	3.25	0.6	4	10.85	2.7	66.13	21
22	Ravichandran <i>et al.</i>	2.5	3.25	0.6	4.5	10.85	2.7	68.84	21
23	Hussain <i>et al.</i>	1.75	4.25	1.8	3	10.8	2.7	71.54	23
24	Shen <i>et al.</i>	3	2.75	1	4	10.75	2.7	74.23	24
25	Du <i>et al.</i>	3	4	1	2.75	10.75	2.7	76.91	24
26	Chen <i>et al.</i>	3	4	1	2.5	10.5	2.6	79.54	26
27	Wang <i>et al.</i>	3	4.25	1	2.25	10.5	2.6	82.16	26
28	David <i>et al.</i>	3	3.75	2	1.5	10.25	2.6	84.73	28
29	Xu <i>et al.</i>	2.75	3.5	1.6	2.25	10.1	2.5	87.25	29
30	Zeng <i>et al.</i>	1.75	3	0.8	4.5	10.05	2.5	89.76	30
31	SyuanPan <i>et al.</i>	2.5	3.25	1.4	2.75	9.9	2.5	92.24	31
32	Chen <i>et al.</i>	2.5	2.5	0.8	4	9.8	2.5	94.69	32
33	Cheung <i>et al.</i>	2.5	4.25	1.4	1.5	9.65	2.4	97.10	33
34	Liu <i>et al.</i>	3.25	3.75	1	1.5	9.5	2.4	99.48	34
35	Gegundez-Arias <i>et al.</i>	3	4	1	1.5	9.5	2.4	101.85	34
36	Du <i>et al.</i>	3	4	1	1.5	9.5	2.4	104.23	34
37	Dong <i>et al.</i>	1.75	4.25	1	2.25	9.25	2.3	106.54	37
38	Zhou <i>et al.</i>	3.5	4	0	1.75	9.25	2.3	108.85	37
39	Shinohara <i>et al.</i>	2.5	4.25	2.2	0.25	9.2	2.3	111.15	39
40	Abraham <i>et al.</i>	1.75	4.25	0.8	2.25	9.05	2.3	113.41	40
41	Feiger <i>et al.</i>	2.5	4	1	1.5	9	2.3	115.66	41
42	Bhatia <i>et al.</i>	3	3.25	1	1.5	8.75	2.2	117.85	42
43	Sieren <i>et al.</i>	2.5	3	2	1.25	8.75	2.2	120.04	42
44	Wang <i>et al.</i>	1.75	4.25	0.4	2.25	8.65	2.2	122.20	44
45	Claux <i>et al.</i>	2.75	3.75	0.6	1.5	8.6	2.2	124.35	45
46	Jiang <i>et al.</i>	2.5	4	0.6	1.5	8.6	2.2	126.50	45
47	Ding <i>et al.</i>	2.5	3.25	1	1.5	8.25	2.1	128.56	47
48	Jun <i>et al.</i>	1.75	4	0.8	1.5	8.05	2.0	130.58	48
49	Xie <i>et al.</i>	1.75	3	1.8	1.5	8.05	2.0	132.59	48
50	Shi <i>et al.</i>	2.5	2.75	1	1.75	8	2.0	134.59	50
51	Pham <i>et al.</i>	1.75	4	0.2	2	7.95	2.0	136.58	51
52	Livne <i>et al.</i>	1.75	4	1.8	0.25	7.8	2.0	138.53	52
53	Thuy <i>et al.</i>	2.5	3	2	0.25	7.75	1.9	140.46	53
54	Rui wang <i>et al.</i>	1.75	4	0.6	0.75	7.1	1.8	142.24	54

Participants: Demographic, Image Modality, Multicenter, and Data Type); Predictors: Model Layers, Conv. type, Loss type, and Optimizer; Outcome: Accuracy, Dice, Jaccard, MCC, and HSD; Analysis: Scientific Validation, Statistical Analysis, Benchmarking, and XAI.

TABLE 15. Non-vascular PROBAST.

SN	Author	Participants	Predictors	Outcomes	Analysis	Total	Mean	Cumm	Rank
1	Chen <i>et al.</i>	2.5	4.5	2.6	4.5	14.1	3.5	3.53	1
2	Khattab <i>et al.</i>	2.5	4.25	2.4	4.5	13.65	3.4	6.94	2
3	Zhao <i>et al.</i>	2.5	2.5	4	4.5	13.5	3.4	10.31	3
4	Gu <i>et al.</i>	3	4.25	2	4	13.25	3.3	13.63	4
5	Xianxiang <i>et al.</i>	3	4.25	1.8	4	13.05	3.3	16.89	5
6	Rampun <i>et al.</i>	2.5	4.5	2.4	3.25	12.65	3.2	20.05	6
7	Zhu <i>et al.</i>	2.5	4	1.8	4.25	12.55	3.1	23.19	7
8	Hong <i>et al.</i>	2.5	3	2	5	12.5	3.1	26.31	8
9	Arora <i>et al.</i>	3	4.25	3	2.25	12.5	3.1	29.44	8
10	Li <i>et al.</i>	2.75	4	2	3.5	12.25	3.1	32.50	10
11	Das <i>et al.</i>	2.5	4	2	3.5	12	3.0	35.50	11
12	Wang <i>et al.</i>	3	4	3	2	12	3.0	38.50	11
13	Li <i>et al.</i>	3	4	2	3	12	3.0	41.50	11
14	Zhang <i>et al.</i>	2.5	4.25	1	4.25	12	3.0	44.50	11
15	Pedoia <i>et al.</i>	2.75	4	0.8	4	11.55	2.9	47.39	15
16	Nour <i>et al.</i>	2.75	3	3.2	2.5	11.45	2.9	50.25	16
17	Jin <i>et al.</i>	2.5	3.75	1.6	3.5	11.35	2.8	53.09	17
18	Pezzano <i>et al.</i>	2.5	4	2	2.75	11.25	2.8	55.90	18
19	Chang <i>et al.</i>	2.5	3.75	1	4	11.25	2.8	58.71	18
20	Tong <i>et al.</i>	2.5	4	0.6	4	11.1	2.8	61.49	20
21	Aswathy <i>et al.</i>	2.75	3.75	1.8	2.75	11.05	2.8	64.25	21
22	Ghavmi <i>et al.</i>	2.75	4	1.8	2.5	11.05	2.8	67.01	21
23	Ahmed <i>et al.</i>	3.5	3.75	1	2.75	11	2.8	69.76	23
24	Wang <i>et al.</i>	3	2.75	2	3.25	11	2.8	72.51	23
25	Sivagami <i>et al.</i>	2.75	3.75	2	2.25	10.75	2.7	75.20	25
26	Zhang <i>et al.</i>	2.75	3.75	2.2	2	10.7	2.7	77.88	26
27	Liu <i>et al.</i>	2.5	4	2.2	2	10.7	2.7	80.55	26
28	Yang <i>et al.</i>	3.25	3.75	0.4	3.25	10.65	2.7	83.21	28
29	Voulodimos <i>et al.</i>	2.5	3.75	1.6	2.75	10.6	2.7	85.86	29
30	Cao <i>et al.</i>	2.5	4.75	1.6	1.5	10.35	2.6	88.45	30
31	He <i>et al.</i>	2.5	4	1.8	2	10.3	2.6	91.03	31
32	Jin <i>et al.</i>	2.5	3.25	3	1.5	10.25	2.6	93.59	32
33	Wang <i>et al.</i>	2.5	3.75	1.4	2.5	10.15	2.5	96.13	33
34	Hoang thi <i>et al.</i>	3.25	3.75	0.4	2.75	10.15	2.5	98.66	33
35	Li <i>et al.</i>	3	3.75	0.6	2.75	10.1	2.5	101.19	35
36	Chen <i>et al.</i>	2.5	3.75	2	1.75	10	2.5	103.69	36
37	Cendejas-Zaragoza <i>et al.</i>	2.5	4	1	2.5	10	2.5	106.19	36
38	Khoong <i>et al.</i>	2.5	2.5	1	3.75	9.75	2.4	108.63	38
39	Li <i>et al.</i>	3	4	0.8	1.75	9.55	2.4	111.01	39
40	Ajmera <i>et al.</i>	3	3.75	0	2.75	9.5	2.4	113.39	40
41	Zhou <i>et al.</i>	2.5	4.25	0.4	2	9.15	2.3	115.68	41
42	Viksit <i>et al.</i>	2.75	4	0.8	1.5	9.05	2.3	117.94	42
43	Fatemah el al.	2.5	3	0.8	2.75	9.05	2.3	120.20	42
44	Li <i>et al.</i>	2.5	3.75	0.8	2	9.05	2.3	122.46	42
45	Pan <i>et al.</i>	2.75	3.75	1	1.5	9	2.3	124.71	45
46	Aldoz <i>et al.</i>	2.5	3	2	1.5	9	2.3	126.96	45
47	Ma <i>et al.</i>	2.5	3	1.8	1.5	8.8	2.2	129.16	47
49	Sun <i>et al.</i>	3	3	1	1.75	8.75	2.2	131.35	48
50	Dalmis <i>et al.</i>	2.5	4	0	1.75	8.25	2.1	133.41	49
51	Chahal <i>et al.</i>	2.5	3.25	1	1.5	8.25	2.1	135.48	49
52	Yong <i>et al.</i>	2.5	4.25	0.2	1.25	8.2	2.1	137.53	51
53	Blanc-Durand <i>et al.</i>	2.5	3.5	0.8	1.25	8.05	2.0	139.54	52
54	Kumar <i>et al.</i>	2.5	4.25	0.4	0.75	7.9	2.0	141.51	53
55	Zhu <i>et al.</i>	2.5	3	0.8	1.5	7.8	2.0	143.46	54
56	Zhang <i>et al.</i>	2.75	3	0	2	7.75	1.9	145.40	55
57	Machireddy <i>et al.</i>	2.5	3	0.6	1.25	7.35	1.8	147.24	56

Participants: Demographic, Image Modality, Multicenter, and Data Type); Predictors: Model Layers, Conv. type, Loss type, and Optimizer; Outcome: Accuracy, Dice, Jaccard, MCC, and HSD; Analysis: Scientific Validation, Statistical Analysis, Benchmarking, and XAI.

TABLE 16. Benchmarking table.

S N	Author	Year	# Ref	#App.	App. Type	LF	UT	Pruning	XAI	Bias	PISMA	SoA	Cascaded/3D UNet
1	Liu et al. [177]	2020	157	9	A1	✗	✓	✗	✗	✗	✗	✓	Cascaded, 3D
2	Du et al. [247]	2020	63	15	A2	✗	✗	✗	✗	✗	✓	✗	✗
3	Siddique et al. [246]	2021	387	2	Brain tumor, Cancer, Retinal	✗	✓	✗	✗	✗	✗	✗	Cascaded, 3D
4	Samarasinghe et al. [248]	2021	92	3	Thorax, Neck, Abdomen	✗	✗	✗	✗	✗	✓	✗	✗
5	Lagree et al. [249]	2021	89	1	Breast Cancer	✓	✗	✗	✗	✗	✗	✗	✗
6	Saadi et al. [250]	2021	107	1	Orthopaedic	✓	✗	✗	✗	✗	✗	✗	✗
7	He et al. [253]	2022	56	1	Thyroid tissue	✓	✗	✗	✗	✗	✗	✗	✗
8	Punn et al. [251]	2022	195	1	COVID-19	✗	✓	✗	✗	✗	✗	✗	✗
9	Yin et al. [252]	2022	80	3	COVID-19, Retina, Vessel	✓	✗	✗	✗	✗	✗	✗	Cascaded
10	Wu et al. [254]	2022	155	1	Microscopic Images	✗	✓	✗	✗	✗	✓	✗	Cascaded, 3D
11	Suri et al. (Proposed)	2022	267	11	A3	✓	✓	✓	✓	✓	✓	✓	Cascaded, 3D

Ref: Number of references; #App: Number of applications; App.: Application; LF: Loss function; SoA: State of the Art; A1: Brain tumor, Stroke, White matter hyperintensities (WMHs), Eye, Cardiac, Liver, Musculoskeletal, Skin cancer, and Neuronal pathology; A2: Cardiac images, Cardiac MRI, left ventricle cavity, Left ventricle, Hippocampus, Rectal tumors, Cartilage and meniscus, Colorectal tumors, Colorectal tumor, Brain extraction, Knee, Lung, Proximal femur, Liver vessel, Prostate; A3: Pulmonary, Immunology, Urology, Neurology, Orthopaedic, Gastroenterology, Dental, Ophthalmology, Skin, Cardiology, Carotid.

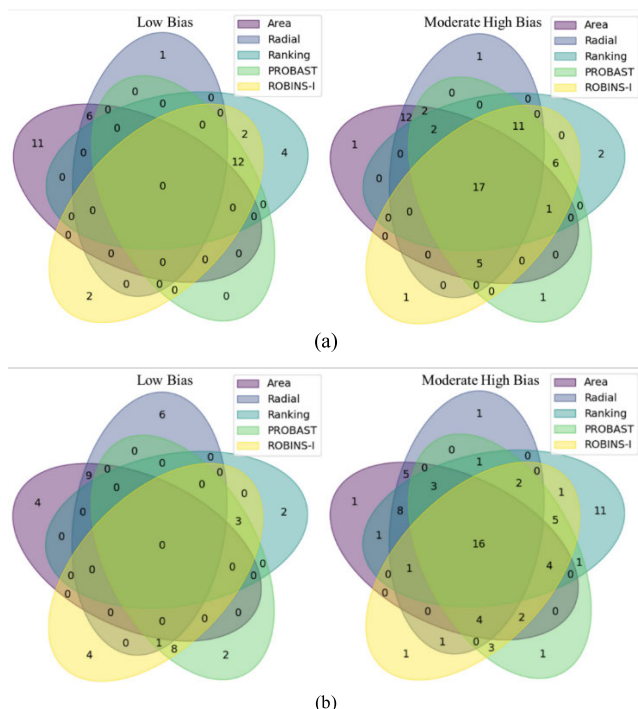


FIGURE 47. (a). Venn diagram for vascular studies. (b). Venn diagram for non-vascular studies.

half a decade, the process of innovation has just begun in the computer vision field comprising segmentation and classification. By modifying UNet components with stochastic image processing infrastructure, such dynamic growth has a high potential [17].

XI. CONCLUSION

The need for UNet-based stratification into several unique classes was deemed necessary, and this study demonstrated five unique paradigms, namely cUNet, sUNet, acUNet, hUNet, and eUNet. sUNet was the superior UNet which underwent several waves of iterations to handle, position, shape, and object scales in 2-D and 3-D image segmentation. The focus of the study was purely on vascular vs. non-vascular applications. A thorough investigation was conducted to study certain attention blocks that modified the conventional UNet architectures, leading to stable and superior performances. Further, this is the only study of its kind that introduces explainable AI, pruning and evaluates AP(ai)Bias 2.0-UNet, further benchmarking with (i) ranking, (ii) butterfly, (iii) regional area, (iv) PROBAST, and (v) ROBIN’s methods. Most of the studies suffered from poor attention in XAI and pruning strategies. Also, segmentation challenges-architecture solutions-key were provided. While the UNet-based strategy has dominated the field of image segmentation, more practical aspects of the UNet from paper-to-practice need to be the focus for better clinical setting applications.

REFERENCES

- [1] J. S. Suri, “Computer vision, pattern recognition and image processing in left ventricle segmentation: The last 50 years,” *Pattern Anal. Appl.*, vol. 3, no. 3, pp. 209–242, Sep. 2000.
- [2] V. K. Shrivastava, N. D. Londhe, R. S. Sonawane, and J. S. Suri, “A novel and robust Bayesian approach for segmentation of psoriasis lesions and its risk stratification,” *Comput. Methods Programs Biomed.*, vol. 150, pp. 9–22, Oct. 2017.
- [3] M. Kass, A. Witkin, and D. Terzopoulos, “Snakes: Active contour models,” *Int. J. Comput. Vis.*, vol. 1, no. 4, pp. 321–331, Jan. 1987.

- [4] J. A. Sethian, *Level Set Methods and Fast Marching Methods: Evolving Interfaces in Computational Geometry, Fluid Mechanics, Computer Vision, and Materials Science*. Cambridge, U.K.: Cambridge Univ. Press, 1999.
- [5] J. S. Suri, S. Singh, and L. Reden, "Fusion of region and boundary/surface-based computer vision and pattern recognition techniques for 2-D and 3-D MR cerebral cortical segmentation (Part-II): A state-of-the-art review," *Pattern Anal. Appl.*, vol. 5, no. 1, pp. 77–98, May 2002.
- [6] L. Saba, "The present and future of deep learning in radiology," *Eur. J. Radiol.*, vol. 114, pp. 14–24, May 2019.
- [7] B. Mainak, "State-of-the-art review on deep learning in medical imaging," *Frontiers Biosci. Landmark*, vol. 24, no. 3, pp. 380–406, 2019.
- [8] J. A. Sethian, "A fast marching level set method for monotonically advancing fronts," *Proc. Nat. Acad. Sci. USA*, vol. 93, no. 4, pp. 1591–1595, 1996.
- [9] L. Saba, H. Gao, U. R. Acharya, S. Sannia, G. Ledda, and J. S. Suri, "Analysis of carotid artery plaque and wall boundaries on CT images by using a semi-automatic method based on level set model," *Neuroradiology*, vol. 54, no. 11, pp. 1207–1214, Nov. 2012.
- [10] J. S. Suri and S. Laxminarayan, *PDE and Level Sets*. Cham, Switzerland: Springer, 2002.
- [11] J. S. Suri, K. Liu, S. Singh, S. N. Laxminarayan, X. Zeng, and L. Reden, "Shape recovery algorithms using level sets in 2-D/3-D medical imagery: A state-of-the-art review," *IEEE Trans. Inf. Technol. Biomed.*, vol. 6, no. 1, pp. 8–28, Mar. 2002.
- [12] A. Rodtook, K. Kirimasthong, W. Lohitvisate, and S. S. Makhanov, "Automatic initialization of active contours and level set method in ultrasound images of breast abnormalities," *Pattern Recognit.*, vol. 79, pp. 172–182, Jul. 2018.
- [13] A. El-Baz and J. S. Suri, *Level Set Method in Medical Imaging Segmentation*. Boca Raton, FL, USA: CRC Press, 2019.
- [14] J. S. Suri, "White matter/gray matter boundary segmentation using geometric snakes: A fuzzy deformable model," in *Proc. Int. Conf. Adv. Pattern Recognit.*, Cham, Switzerland: Springer, 2001, pp. 333–340.
- [15] V. Kuppili, M. Biswas, A. Sreekumar, H. S. Suri, L. Saba, D. R. Edla, R. T. Marinhoe, J. M. Sanches, and J. S. Suri, "Extreme learning machine framework for risk stratification of fatty liver disease using ultrasound tissue characterization," *J. Med. Syst.*, vol. 41, no. 10, pp. 1–20, Oct. 2017.
- [16] U. R. Acharya, O. Faust, A. P. C. Alvin, G. Krishnamurthi, J. C. R. Seabra, J. Sanches, and J. S. Suri, "Understanding symptomatology of atherosclerotic plaque by image-based tissue characterization," *Comput. Methods Programs Biomed.*, vol. 110, no. 1, pp. 66–75, Apr. 2013.
- [17] A. El-Baz, G. Gimel'farb, and J. S. Suri, *Stochastic Modeling for Medical Image Analysis*. Boca Raton, FL, USA: CRC Press, 2015.
- [18] J. S. Suri and R. M. Rangayyan, *Breast Imaging, Mammography, and Computer-Aided Diagnosis of Breast Cancer*. Bellingham, WA, USA: SPIE, 2006.
- [19] V. K. Shrivastava, N. D. Londhe, R. S. Sonawane, and J. S. Suri, "Reliable and accurate psoriasis disease classification in dermatology images using comprehensive feature space in machine learning paradigm," *Expert Syst. Appl.*, vol. 42, nos. 15–16, pp. 6184–6195, Sep. 2015.
- [20] A. S. El-Baz, R. Acharya, M. Mirmehdi, and J. S. Suri, *Multi Modality State-of-the-Art Medical Image Segmentation and Registration Methodologies*, vol. 1. Cham, Switzerland: Springer, 2011.
- [21] R. H. Hashemi, W. G. Bradley, and C. J. Lisanti, *MRI: The Basics: The Basics*. Philadelphia, PA, USA: Lippincott Williams & Wilkins, 2012.
- [22] L. Saba and J. S. Suri, *Multi-Detector CT Imaging Handbook, Two Volume Set*. Boca Raton, FL, USA: CRC Press, 2022.
- [23] J. M. Sanches, A. F. Laine, and J. S. Suri, *Ultrasound Imaging*. Cham, Switzerland: Springer, 2012.
- [24] A. D. Jamthikar, D. Gupta, L. E. Mantella, L. Saba, J. R. Laird, A. M. Johri, and J. S. Suri, "Multiclass machine learning vs. conventional calculators for stroke/CVD risk assessment using carotid plaque predictors with coronary angiography scores as gold standard: A 500 participants study," *Int. J. Cardiovascular Imag.*, vol. 37, no. 4, pp. 1171–1187, Apr. 2021.
- [25] O. Ronneberger, P. Fischer, and T. Brox, "U-Net: Convolutional networks for biomedical image segmentation," in *Proc. Int. Conf. Med. Image Comput. Comput. Assist. Intervent*, 2015, pp. 234–241.
- [26] J. S. Suri and S. Laxminarayan, *Angiography and Plaque Imaging: Advanced Segmentation Techniques*. Boca Raton, FL, USA: CRC Press, 2003.
- [27] B. Jena, S. Saxena, G. K. Nayak, A. Balestrieri, N. Gupta, N. N. Khanna, J. R. Laird, M. K. Kalra, M. M. Fouda, L. Saba, and J. S. Suri, "Brain tumor characterization using radiogenomics in artificial intelligence framework," *Cancers*, vol. 14, no. 16, p. 4052, Aug. 2022.
- [28] N. N. Khanna, "Vascular implications of COVID-19: Role of radiological imaging, artificial intelligence, and tissue characterization: A special report," *J. Cardiovascular Develop. Disease*, vol. 9, no. 8, p. 268, Aug. 2022.
- [29] S. Saxena, B. Jena, N. Gupta, S. Das, D. Sarmah, P. Bhattacharya, T. Nath, S. Paul, M. M. Fouda, M. Kalra, L. Saba, G. Pareek, and J. S. Suri, "Role of artificial intelligence in radiogenomics for cancers in the era of precision medicine," *Cancers*, vol. 14, no. 12, p. 2860, Jun. 2022.
- [30] S. Munjral, "Cardiovascular risk stratification in diabetic retinopathy via atherosclerotic pathway in COVID-19/non-COVID-19 frameworks using artificial intelligence paradigm: A narrative review," *Diagnostics*, vol. 12, no. 5, p. 1234, May 2022.
- [31] J. S. Suri, S. Paul, M. A. Maingdarkar, A. Puvvula, S. Saxena, L. Saba, M. Turk, J. R. Laird, N. N. Khanna, K. Viskovic, I. M. Singh, M. Kalra, P. R. Krishnan, A. Johri, and K. I. Paraskevas, "Cardiovascular/stroke risk stratification in Parkinson's disease patients using atherosclerosis pathway and artificial intelligence paradigm: A systematic review," *Metabolites*, vol. 12, no. 4, p. 312, Mar. 2022.
- [32] J. S. Suri, M. Bhagawati, S. Paul, A. D. Protogerou, P. P. Sfrikakis, G. D. Kitas, N. N. Khanna, Z. Ruzsa, A. M. Sharma, S. Saxena, G. Faa, J. R. Laird, A. M. Johri, M. K. Kalra, K. I. Paraskevas, and L. Saba, "A powerful paradigm for cardiovascular risk stratification using multiclass, multi-label, and ensemble-based machine learning paradigms: A narrative review," *Diagnostics*, vol. 12, no. 3, p. 722, Mar. 2022.
- [33] S. Das, G. K. Nayak, L. Saba, M. Kalra, J. S. Suri, and S. Saxena, "An artificial intelligence framework and its bias for brain tumor segmentation: A narrative review," *Comput. Biol. Med.*, vol. 143, Apr. 2022, Art. no. 105273.
- [34] J. S. Suri, M. Bhagawati, S. Paul, A. Protogerou, P. P. Sfrikakis, G. D. Kitas, N. N. Khanna, Z. Ruzsa, A. M. Sharma, S. Saxena, G. Faa, K. I. Paraskevas, J. R. Laird, A. M. Johri, L. Saba, and M. Kalra, "Understanding the bias in machine learning systems for cardiovascular disease risk assessment: The first of its kind review," *Comput. Biol. Med.*, vol. 142, Mar. 2022, Art. no. 105204.
- [35] D. Moher, A. Liberati, J. Tetzlaff, D. G. Altman, and G. Prisma, "Preferred reporting items for systematic reviews and meta-analyses: The PRISMA statement," *Ann. Internal Med.*, vol. 151, no. 4, pp. 264–269, 2009.
- [36] R. Cau, A. Pacielli, H. Fatemeh, P. Vaudano, C. Arru, P. Crivelli, G. Stranieri, J. S. Suri, L. Mannelli, M. Conti, A. Mahammedi, M. Kalra, and L. Saba, "Complications in COVID-19 patients: Characteristics of pulmonary embolism," *Clin. Imag.*, vol. 77, pp. 244–249, Sep. 2021.
- [37] J. S. Suri, "COVID-19 pathways for brain and heart injury in comorbidity patients: A role of medical imaging and artificial intelligence-based COVID severity classification: A review," *Comput. Biol. Med.*, vol. 124, Sep. 2020, Art. no. 103960.
- [38] R. Cau, P. P. Bassareo, L. Mannelli, J. S. Suri, and L. Saba, "Imaging in COVID-19-related myocardial injury," *Int. J. Cardiovascular Imag.*, vol. 37, no. 4, pp. 1349–1360, Apr. 2021.
- [39] L. Saba, "Molecular pathways triggered by COVID-19 in different organs: ACE2 receptor-expressing cells under attack? A review," *Eur. Rev. Med. Pharmacol. Sci.*, vol. 24, no. 23, pp. 12609–12622, Dec. 2020.
- [40] J. S. Suri, "Integration of cardiovascular risk assessment with COVID-19 using artificial intelligence," *Rev. Cardiovascular Med.*, vol. 21, no. 4, pp. 541–560, 2020.
- [41] V. Viswanathan, "Bidirectional link between diabetes mellitus and coronavirus disease 2019 leading to cardiovascular disease: A narrative review," *World J. Diabetes*, vol. 12, no. 3, p. 215, 2021.
- [42] A. A. L. and V. C. Ss, "Cascaded 3D UNet architecture for segmenting the COVID-19 infection from lung CT volume," *Sci. Rep.*, vol. 12, no. 1, p. 3090, Feb. 2022.
- [43] R. Zhou, M. R. Azarpazhooh, J. D. Spence, S. Hashemi, W. Ma, X. Cheng, H. Gan, M. Ding, and A. Fenster, "Deep learning-based carotid plaque segmentation from B-mode ultrasound images," *Ultrasound Med. Biol.*, vol. 47, no. 9, pp. 2723–2733, Sep. 2021.
- [44] S. Sivagami, P. Chitra, G. S. R. Kailash, and S. R. Muralidharan, "UNet architecture based dental panoramic image segmentation," in *Proc. Int. Conf. Wireless Commun. Signal Process. Netw. (WiSPNET)*, Aug. 2020, pp. 187–191.

- [45] S. Li, J. Liu, and Z. Song, "Brain tumor segmentation based on region of interest-aided localization and segmentation U-Net," *Int. J. Mach. Learn. Cybern.*, vol. 13, pp. 2435–2445, 2022, doi: [10.1007/s13042-022-01536-4](https://doi.org/10.1007/s13042-022-01536-4).
- [46] M. M. Sieren, C. Widmann, N. Weiss, J. H. Moltz, F. Link, F. Wegner, E. Stahlberg, M. Horn, T. H. Oecherting, J. P. Goltz, J. Barkhausen, and A. Frydrychowicz, "Automated segmentation and quantification of the healthy and diseased aorta in CT angiographies using a dedicated deep learning approach," *Eur. Radiol.*, vol. 32, no. 1, pp. 690–701, Jan. 2022.
- [47] L. N. L. Thuy, T. D. Trinh, L. H. Anh, J. Y. Kim, H. T. Hieu, and P. T. Bao, "Coronary vessel segmentation by coarse-to-fine strategy using U-nets," *BioMed Res. Int.*, vol. 2021, pp. 1–10, Apr. 2021.
- [48] M. Xie, Y. Li, Y. Xue, L. Huntress, W. Beckerman, S. A. Rahimi, J. W. Ady, and U. W. Roshan, "Two-stage and dual-decoder convolutional U-Net ensembles for reliable vessel and plaque segmentation in carotid ultrasound images," in *Proc. 19th IEEE Int. Conf. Mach. Learn. Appl. (ICMLA)*, Dec. 2020, pp. 1376–1381.
- [49] T. P. Van, S. T. Nguyen, L. B. Doan, N. N. Tran, and T. M. Thanh, "Efficient palm-line segmentation with U-Net context fusion module," in *Proc. Int. Conf. Adv. Comput. Appl. (ACOMP)*, Nov. 2020, pp. 23–28.
- [50] T.-N. Hoang-Thi, M. Vakalopoulou, S. Christodoulidis, N. Paragios, M.-P. Revel, and G. Chassagnon, "Deep learning for lung disease segmentation on CT: Which reconstruction kernel should be used?" *Diagnostic Interventional Imag.*, vol. 102, no. 11, pp. 691–695, Nov. 2021.
- [51] Y.-P. Wang, Y.-C. Jheng, K.-Y. Sung, H.-E. Lin, I.-F. Hsin, P.-H. Chen, Y.-C. Chu, D. Lu, Y.-J. Wang, M.-C. Hou, F.-Y. Lee, and C.-L. Lu, "Use of U-Net convolutional neural networks for automated segmentation of fecal material for objective evaluation of bowel preparation quality in colonoscopy," *Diagnostics*, vol. 12, no. 3, p. 613, Mar. 2022.
- [52] A. Ushinsky, M. Bardis, J. Glavis-Bloom, E. Uchio, C. Chantaduly, M. Nguyentat, D. Chow, P. D. Chang, and R. Houshyar, "A 3D-2D hybrid U-Net convolutional neural network approach to prostate organ segmentation of multiparametric MRI," *Amer. J. Roentgenol.*, vol. 216, no. 1, pp. 111–116, Jan. 2021.
- [53] P. K. Jain, N. Sharma, L. Saba, K. I. Paraskevas, M. K. Kalra, A. Johri, A. N. Nicolaides, and J. S. Suri, "Automated deep learning-based paradigm for high-risk plaque detection in B-mode common carotid ultrasound scans: An asymptomatic Japanese cohort study," *Int. Angiol.*, vol. 41, no. 1, pp. 9–23, Feb. 2022.
- [54] A. Nour, S. Saad, and B. Boufama, "Prostate biomedical images segmentation and classification by using U-NET CNN model," in *Proc. 12th ACM Conf. Bioinf., Comput. Biol., Health Informat.*, Aug. 2021, pp. 1–7.
- [55] S. Ahmed, T. Hossain, O. B. Hoque, S. Sarker, S. Rahman, and F. M. Shah, "Automated COVID-19 detection from chest X-ray images: A high-resolution network (HRNet) approach," *Social Netw. Comput. Sci.*, vol. 2, no. 4, pp. 1–17, Jul. 2021.
- [56] P. Ajmera, A. Kharat, S. Dhirawani, S. M. Khaladkar, V. Kulkarni, V. Duddalwar, P. Lamghare, and S. Rathi, "Evaluating the association between comorbidities and COVID-19 severity scoring on chest CT examinations between the two waves of COVID-19: An imaging study using artificial intelligence," *Cureus*, vol. 14, no. 1, pp. 1–17, Jan. 2022.
- [57] G. Pezzano, O. Díaz, V. R. Ripoll, and P. Radeva, "CoLe-CNN+: Context learning–convolutional neural network for COVID-19-ground-glass-opacities detection and segmentation," *Comput. Biol. Med.*, vol. 136, Sep. 2021, Art. no. 104689.
- [58] A. Voulodimos, E. Protopapadakis, I. Katsamenis, A. Doulamis, and N. Doulamis, "A few-shot U-Net deep learning model for COVID-19 infected area segmentation in CT images," *Sensors*, vol. 21, no. 6, p. 2215, Mar. 2021.
- [59] J. Yang, B. Wu, L. Li, P. Cao, and O. Zaiane, "MSDS-UNet: A multi-scale deeply supervised 3D U-Net for automatic segmentation of lung tumor in CT," *Computerized Med. Imag. Graph.*, vol. 92, Sep. 2021, Art. no. 101957.
- [60] L. Cendejas-Zaragoza, D. E. Rodriguez-Obregon, A. R. Mejia-Rodriguez, E. R. Arce-Santana, and A. Santos-Diaz, "COVID-19 volumetric pulmonary lesion estimation on CT images using a U-NET and probabilistic active contour segmentation," in *Proc. 43rd Annu. Int. Conf. IEEE Eng. Med. Biol. Soc. (EMBC)*, Nov. 2021, pp. 3850–3853.
- [61] X. Zhang, X. Liu, B. Zhang, J. Dong, B. Zhang, S. Zhao, and S. Li, "Accurate segmentation for different types of lung nodules on CT images using improved U-Net convolutional network," *Medicine*, vol. 100, no. 40, 2021, Art. no. e27491.
- [62] X. Ma, L. M. Hadjiiski, J. Wei, H. Chan, K. H. Cha, R. H. Cohan, E. M. Cacioli, R. Samala, C. Zhou, and Y. Lu, "U-Net based deep learning bladder segmentation in CT urography," *Med. Phys.*, vol. 46, no. 4, pp. 1752–1765, Apr. 2019.
- [63] F. Claux, M. Baudouin, C. Bogey, and A. Rouchaud, "Dense, deep learning-based intracranial aneurysm detection on TOF MRI using two-stage regularized U-Net," *J. Neuroradiol.*, to be published. [Online]. Available: <https://www.sciencedirect.com/science/article/pii/S0150986122001018?via%3Dihub>
- [64] M. Yi, L.-C. Wu, Q.-Y. Du, C.-Z. Guan, M.-D. Liu, X.-S. Li, H.-L. Xiong, H.-S. Tan, X.-H. Wang, J.-P. Zhong, D.-A. Han, M.-Y. Wang, and Y.-G. Zeng, "Spatiotemporal absorption fluctuation imaging based on U-Net," *J. Biomed. Opt.*, vol. 27, no. 2, Feb. 2022, Art. no. 026002.
- [65] C. Liu, P. Gu, and Z. Xiao, "Multiscale U-Net with spatial positional attention for retinal vessel segmentation," *J. Healthcare Eng.*, vol. 2022, pp. 1–10, Jan. 2022.
- [66] D. Chen, W. Yang, L. Wang, S. Tan, J. Lin, and W. Bu, "PCAT-UNet: UNet-like network fused convolution and transformer for retinal vessel segmentation," *PLoS ONE*, vol. 17, no. 1, Jan. 2022, Art. no. e0262689.
- [67] K.-B. Chen, Y. Xuan, A.-J. Lin, and S.-H. Guo, "Lung computed tomography image segmentation based on U-Net network fused with dilated convolution," *Comput. Methods Programs Biomed.*, vol. 207, Aug. 2021, Art. no. 106170.
- [68] X. Cao, H. Chen, Y. Li, Y. Peng, S. Wang, and L. Cheng, "Dilated densely connected U-Net with uncertainty focus loss for 3D ABUS mass segmentation," *Comput. Methods Programs Biomed.*, vol. 209, Sep. 2021, Art. no. 106313.
- [69] A. Kumar, N. Upadhyay, P. Ghosal, T. Chowdhury, D. Das, A. Mukherjee, and D. Nandi, "CSNet: A new DeepNet framework for ischemic stroke lesion segmentation," *Comput. Methods Programs Biomed.*, vol. 193, Sep. 2020, Art. no. 105524.
- [70] A. Rampun, D. Jarvis, P. D. Griffiths, R. Zwiggelaar, B. W. Scotney, and P. A. Armitage, "Single-input multi-output U-Net for automated 2D foetal brain segmentation of MR images," *J. Imag.*, vol. 7, no. 10, p. 200, Oct. 2021.
- [71] Z. Wang, Y. Zou, and P. X. Liu, "Hybrid dilation and attention residual U-Net for medical image segmentation," *Comput. Biol. Med.*, vol. 134, Jul. 2021, Art. no. 104449.
- [72] S. Cai, Y. Wu, and G. Chen, "A novel elastomeric UNet for medical image segmentation," *Frontiers Aging Neurosci.*, vol. 14, Mar. 2022, Art. no. 841297.
- [73] S. Xu, Z. Zhang, Q. Zhou, W. Shao, and W. Tan, "A pulmonary vascular extraction algorithm from chest CT/CTA images," *J. Healthcare Eng.*, vol. 2021, pp. 1–7, Nov. 2021.
- [74] T.-H. Yong, S. Yang, S.-J. Lee, C. Park, J.-E. Kim, K.-H. Huh, S.-S. Lee, M.-S. Heo, and W.-J. Yi, "QCBCT-NET for direct measurement of bone mineral density from quantitative cone-beam CT: A human skull phantom study," *Sci. Rep.*, vol. 11, no. 1, pp. 1–13, Jul. 2021.
- [75] X. Zhao, P. Zhang, F. Song, G. Fan, Y. Sun, Y. Wang, Z. Tian, L. Zhang, and G. Zhang, "D2A U-Net: Automatic segmentation of COVID-19 CT slices based on dual attention and hybrid dilated convolution," *Comput. Biol. Med.*, vol. 135, Aug. 2021, Art. no. 104526.
- [76] T. Zhou, T. Tan, X. Pan, H. Tang, and J. Li, "Fully automatic deep learning trained on limited data for carotid artery segmentation from large image, volumes," *Quant. Imag. Med. Surg.*, vol. 11, no. 1, p. 67, 2021.
- [77] P. Blanc-Durand, A. Van Der Gucht, N. Schaefer, E. Itti, and J. O. Prior, "Automatic lesion detection and segmentation of 18F-FET PET in gliomas: A full 3D U-Net convolutional neural network study," *PLoS ONE*, vol. 13, no. 4, Apr. 2018, Art. no. e0195798.
- [78] G. Tong, Y. Li, H. Chen, Q. Zhang, and H. Jiang, "Improved U-Net network for pulmonary nodules segmentation," *Optik*, vol. 174, pp. 460–469, Dec. 2018.
- [79] J. Ding, Z. Zhang, J. Tang, and F. Guo, "A multichannel deep neural network for retina vessel segmentation via a fusion mechanism," *Frontiers Bioeng. Biotechnol.*, vol. 9, p. 663, Aug. 2021.
- [80] V. Kumar, J. M. Webb, A. Gregory, M. Denis, D. D. Meixner, M. Bayat, D. H. Whaley, M. Fatemi, and A. Alizad, "Automated and real-time segmentation of suspicious breast masses using convolutional neural network," *PLoS ONE*, vol. 13, no. 5, May 2018, Art. no. e0195816.
- [81] M. A. Khattab, I. Y. Liao, E. H. Ooi, and S. Y. Chong, "Compound W-Net with fully accumulative residual connections for liver segmentation using CT images," *Comput. Math. Methods Med.*, vol. 2022, pp. 1–11, Feb. 2022.
- [82] L. Hong, R. Wang, T. Lei, X. Du, and Y. Wan, "Qau-Net: Quartet attention U-Net for liver and liver-tumor segmentation," in *Proc. IEEE Int. Conf. Multimedia Expo. (ICME)*, Jul. 2021, pp. 1–6.

- [83] K. He, "HF-UNet: Learning hierarchically inter-task relevance in multi-task U-Net for accurate prostate segmentation in CT images," *IEEE Trans. Med. Imag.*, vol. 40, no. 8, pp. 2118–2128, Aug. 2021.
- [84] Q. Xiangxiang, Z. Yu, and Z. Bingbing, "Automated segmentation based on residual U-Net model for MR prostate images," in *Proc. 11th Int. Congr. Image Signal Process., Biomed. Eng. Informat. (CISP-BMEI)*, Oct. 2018, pp. 1–6.
- [85] Y. Zhang, J. Wu, W. Chen, Y. Chen, and X. Tang, "Prostate segmentation using Z-Net," in *Proc. IEEE 16th Int. Symp. Biomed. Imag. (ISBI)*, Apr. 2019, pp. 11–14.
- [86] Q. Zhu, B. Du, B. Turkbey, P. L. Choyke, and P. Yan, "Deeply-supervised CNN for prostate segmentation," in *Proc. Int. Joint Conf. Neural Netw. (IJCNN)*, May 2017, pp. 178–184.
- [87] N. Aldojo, F. Biavati, F. Michallek, S. Stober, and M. Dewey, "Automatic prostate and prostate zones segmentation of magnetic resonance images using DenseNet-like U-Net," *Sci. Rep.*, vol. 10, no. 1, pp. 1–17, Aug. 2020.
- [88] E. S. Chahal, A. Patel, A. Gupta, and A. Purwar, "Unet based xception model for prostate cancer segmentation from MRI images," *Multimedia Tools Appl.*, vol. 81, pp. 37333–37349, Nov. 2021.
- [89] W. Chen, Y. Zhang, J. He, Y. Qiao, Y. Chen, H. Shi, E. X. Wu, and X. Tang, "Prostate segmentation using 2D bridged U-Net," in *Proc. Int. Joint Conf. Neural Netw. (IJCNN)*, Jul. 2019, pp. 1–7.
- [90] N. Ghavami, Y. Hu, E. Gibson, E. Bonmati, M. Emberton, C. M. Moore, and D. C. Barratt, "Automatic segmentation of prostate MRI using convolutional neural networks: Investigating the impact of network architecture on the accuracy of volume measurement and MRI-ultrasound registration," *Med. Image Anal.*, vol. 58, Dec. 2019, Art. no. 101558.
- [91] S. Li, Y. Chen, S. Yang, and W. Luo, "Cascade dense-UNet for prostate segmentation in MR images," in *Proc. Int. Conf. Intell. Comput.*, Cham, Switzerland: Springer, 2019, pp. 481–490.
- [92] B. Liu, J. Zheng, H. Zhang, P. Chen, S. Li, and Y. Wen, "An improved 2D U-Net model integrated squeeze-and-excitation layer for prostate cancer segmentation," *Sci. Program.*, vol. 2021, pp. 1–8, Dec. 2021.
- [93] Y. Zhu, R. Wei, G. Gao, L. Ding, X. Zhang, X. Wang, and J. Zhang, "Fully automatic segmentation on prostate MR images based on cascaded fully convolution network," *J. Magn. Reson. Imag.*, vol. 49, no. 4, pp. 1149–1156, Apr. 2019.
- [94] W. Zhao, D. Jiang, J. Peña Queralt, and T. Westerlund, "MSS U-Net: 3D segmentation of kidneys and tumors from CT images with a multi-scale supervised U-Net," *Informat. Med. Unlocked*, vol. 19, Jan. 2020, Art. no. 100357.
- [95] W. K. Cheung, R. Bell, A. Nair, L. J. Menezes, R. Patel, S. Wan, K. Chou, J. Chen, R. Torii, R. H. Davies, J. C. Moon, D. C. Alexander, and J. Jacob, "A computationally efficient approach to segmentation of the aorta and coronary arteries using deep learning," *IEEE Access*, vol. 9, pp. 108873–108888, 2021.
- [96] B. Feiger, E. Lorenzana-Saldivar, C. Cooke, R. Horstmeyer, M. Bishawi, J. Doberne, G. C. Hughes, D. Ranney, S. Voigt, and A. Randles, "Evaluation of U-Net based architectures for automatic aortic dissection segmentation," *ACM Trans. Comput. Healthcare*, vol. 3, no. 1, pp. 1–16, Jan. 2022.
- [97] S. R. Ravichandran, B. Nataraj, S. Huang, Z. Qin, Z. Lu, A. Katsuki, W. Huang, and Z. Zeng, "3D inception U-Net for aorta segmentation using computed tomography cardiac angiography," in *Proc. IEEE EMBS Int. Conf. Biomed. Health Informat. (BHI)*, May 2019, pp. 1–4.
- [98] M. Biswas, L. Saba, S. Chakrabarty, N. N. Khanna, H. Song, H. S. Suri, P. P. Sfikakis, S. Mavrogeni, K. Viskovic, J. R. Laird, E. Cuadrado-Godia, A. Nicolaides, A. Sharma, V. Viswanathan, A. Protogerou, G. Kitas, G. Pareek, M. Miner, and J. S. Suri, "Two-stage artificial intelligence model for jointly measurement of atherosclerotic wall thickness and plaque burden in carotid ultrasound: A screening tool for cardiovascular/stroke risk assessment," *Comput. Biol. Med.*, vol. 123, Aug. 2020, Art. no. 103847.
- [99] Y.-C. Chen, Y.-C. Lin, C.-P. Wang, C.-Y. Lee, W.-J. Lee, T.-D. Wang, and C.-M. Chen, "Coronary artery segmentation in cardiac CT angiography using 3D multi-channel U-Net," 2019, *arXiv:1907.12246*.
- [100] L.-S. Pan, C.-W. Li, S.-F. Su, S.-Y. Tay, Q.-V. Tran, and W. P. Chan, "Coronary artery segmentation under class imbalance using a U-Net based architecture on computed tomography angiography images," *Sci. Rep.*, vol. 11, no. 1, pp. 1–7, Jul. 2021.
- [101] H. Shinohara, S. Kodera, K. Ninomiya, M. Nakamoto, S. Katsushika, A. Saito, S. Minatsuki, H. Kikuchi, A. Kiyosue, Y. Higashikuni, N. Takeda, K. Fujiu, J. Ando, H. Akazawa, H. Morita, and I. Komuro, "Automatic detection of vessel structure by deep learning using intravascular ultrasound images of the coronary arteries," *PLoS ONE*, vol. 16, no. 8, Aug. 2021, Art. no. e0255577.
- [102] X. Du, J. Wang, and W. Sun, "Densely connected U-Net retinal vessel segmentation algorithm based on multi-scale feature convolution extraction," *Med. Phys.*, vol. 48, no. 7, pp. 3827–3841, Jul. 2021.
- [103] Z. Huang, Y. Fang, H. Huang, X. Xu, J. Wang, and X. Lai, "Automatic retinal vessel segmentation based on an improved U-Net approach," *Sci. Program.*, vol. 2021, pp. 1–15, Apr. 2021.
- [104] H. Fu, J. Cheng, Y. Xu, D. W. K. Wong, J. Liu, and X. Cao, "Joint optic disc and cup segmentation based on multi-label deep network and polar transformation," *IEEE Trans. Med. Imag.*, vol. 37, no. 7, pp. 1597–1605, Jul. 2018.
- [105] X. Xiao, S. Lian, Z. Luo, and S. Li, "Weighted res-UNet for high-quality retina vessel segmentation," in *Proc. 9th Int. Conf. Inf. Technol. Med. Educ. (ITME)*, Oct. 2018, pp. 327–331.
- [106] J. Zhang, Y. Zhang, and X. Xu, "Pyramid U-Net for retinal vessel segmentation," in *Proc. IEEE Int. Conf. Acoust., Speech Signal Process. (ICASSP)*, Jun. 2021, pp. 1125–1129.
- [107] N. Abraham, K. Illanko, N. Khan, and D. Androutsos, "Deep learning for semantic segmentation of brachial plexus nerves in ultrasound images using U-Net and M-Net," in *Proc. 3rd Int. Conf. Imag., Signal Process. Commun. (ICISPC)*, Jul. 2019, pp. 85–89.
- [108] R. Wang, H. Shen, and M. Zhou, "Ultrasound nerve segmentation of brachial plexus based on optimized ResU-Net," in *Proc. IEEE Int. Conf. Imag. Syst. Techn. (IST)*, Dec. 2019, pp. 1–6.
- [109] Y. Wang, J. Geng, C. Zhou, and Y. Zhang, "Segmentation of ultrasound brachial plexus based on U-Net," in *Proc. Int. Conf. Commun., Inf. Syst. Comput. Eng. (CISCE)*, May 2021, pp. 482–485.
- [110] A. Hilbert, V. I. Madai, E. M. Akay, O. U. Aydin, J. Behland, J. Sobesky, I. Galinovic, A. A. Khalil, A. A. Taha, J. Wuerfel, P. Dusek, T. Niendorf, J. B. Fiebach, D. Frey, and M. Livne, "BRAVE-NET: Fully automated arterial brain vessel segmentation in patients with cerebrovascular disease," *Frontiers Artif. Intell.*, vol. 3, p. 78, Sep. 2020.
- [111] M. Livne, "A U-Net deep learning framework for high performance vessel segmentation in patients with cerebrovascular disease," *Frontiers Neurosci.*, vol. 13, p. 97, Feb. 2019.
- [112] M. Jiang, J. D. Spence, and B. Chiu, "Segmentation of 3D ultrasound carotid vessel wall using U-Net and segmentation average network," in *Proc. 42nd Annu. Int. Conf. IEEE Eng. Med. Biol. Soc. (EMBC)*, Jul. 2020, pp. 2043–2046.
- [113] R. Gu, "CA-Net: Comprehensive attention convolutional neural networks for explainable medical image segmentation," *IEEE Trans. Med. Imag.*, vol. 40, no. 2, pp. 699–711, Nov. 2020.
- [114] A. Song, L. Xu, L. Wang, B. Wang, X. Yang, B. Xu, B. Yang, and S. E. Greenwald, "Automatic coronary artery segmentation of CCTA images with an efficient feature-fusion-and-rectification 3D-UNet," *IEEE J. Biomed. Health Informat.*, vol. 26, no. 8, pp. 4044–4055, Aug. 2022.
- [115] S. Hussain, F. Guo, W. Li, and Z. Shen, "DiUNet: A U-Net based architecture for blood vessels segmentation," *Comput. Methods Programs Biomed.*, vol. 218, May 2022, Art. no. 106732.
- [116] L. Dong, W. Jiang, W. Lu, J. Jiang, Y. Zhao, X. Song, X. Leng, H. Zhao, J. Wang, C. Li, and J. Xiang, "Automatic segmentation of coronary lumen and external elastic membrane in intravascular ultrasound images using 8-layer U-Net," *Biomed. Eng. Online*, vol. 20, no. 1, pp. 1–9, Dec. 2021.
- [117] T. J. Jun, J. Kweon, Y.-H. Kim, and D. Kim, "T-Net: Nested encoder-decoder architecture for the main vessel segmentation in coronary angiography," *Neural Netw.*, vol. 128, pp. 216–233, Aug. 2020.
- [118] J. Zeng, B. Zhu, Y. Huang, C. Qin, J. Zhu, F. Wang, Y. Zhai, J. Gan, Y. Chen, Y. Wang, R. D. Labati, V. Piuri, and F. Scotti, "Real-time segmentation method of lightweight network for finger vein using embedded terminal technique," *IEEE Access*, vol. 9, pp. 303–316, 2021.
- [119] W. Liu, Y. Jiang, J. Zhang, and Z. Ma, "RFARN: Retinal vessel segmentation based on reverse fusion attention residual network," *PLoS ONE*, vol. 16, no. 12, Dec. 2021, Art. no. e0257256.
- [120] P. K. Jain, N. Sharma, M. K. Kalra, A. Johri, L. Saba, and J. S. Suri, "Far wall plaque segmentation and area measurement in common and internal carotid artery ultrasound using U-series architectures: An unseen artificial intelligence paradigm for stroke risk assessment," *Comput. Biol. Med.*, vol. 149, Oct. 2022, Art. no. 106017.

- [121] M. L. Olender, L. S. Athanasiou, L. K. Michalis, D. I. Fotiadis, and E. R. Edelman, "A domain enriched deep learning approach to classify atherosclerosis using intravascular ultrasound imaging," *IEEE J. Sel. Topics Signal Process.*, vol. 14, no. 6, pp. 1210–1220, Oct. 2020.
- [122] S. A. David, C. Mahesh, V. D. Kumar, K. Polat, A. Alhudaif, and M. Nour, "Retinal blood vessels and optic disc segmentation using U-Net," *Math. Problems Eng.*, vol. 2022, pp. 1–11, Feb. 2022.
- [123] M. U. Dalmış, G. Litjens, K. Holland, A. Setio, R. Mann, N. Karssemeijer, and A. Gubern-Mérida, "Using deep learning to segment breast and fibroglandular tissue in MRI volumes," *Med. Phys.*, vol. 44, no. 2, pp. 533–546, Feb. 2017.
- [124] V. Padoia, B. Norman, S. N. Mehany, M. D. Bucknor, T. M. Link, and S. Majumdar, "3D convolutional neural networks for detection and severity staging of meniscus and PFJ cartilage morphological degenerative changes in osteoarthritis and anterior cruciate ligament subjects," *J. Magn. Reson. Imag.*, vol. 49, no. 2, pp. 400–410, Feb. 2019.
- [125] J. Wang, Y. Yu, R. Yan, J. Liu, H. Wu, D. Geng, and Z. Yu, "Coarse-to-fine multiplanar D-SEA UNet for automatic 3D carotid segmentation in CTA images," *Int. J. Comput. Assist. Radiol. Surg.*, vol. 16, no. 10, pp. 1727–1736, Oct. 2021.
- [126] T.-H. Lee, L.-T. Huang, P. Kuo, C.-K. Wang, and J.-I. Guo, "Focal-balanced attention U-Net with dynamic thresholding by spatial regression for segmentation of aortic dissection in CT imagery," in *Proc. IEEE 18th Int. Symp. Biomed. Imag. (ISBI)*, Apr. 2021, pp. 541–544.
- [127] X. Wang, L. Wang, J. Yang, and X. Feng, "Accurate 3D reconstruction of white matter hyperintensities based on attention-UNet," *Comput. Math. Methods Med.*, vol. 2022, pp. 1–7, Mar. 2022.
- [128] N. Zhang, J. Lin, B. Hui, B. Qiao, W. Yang, R. Shang, X. Wang, and J. Lei, "Lung nodule segmentation and recognition algorithm based on multi-position U-Net," *Comput. Math. Methods Med.*, vol. 2022, pp. 1–11, Mar. 2022.
- [129] P. Sun, Z. Mo, F. Hu, F. Liu, T. Mo, Y. Zhang, and Z. Chen, "Kidney tumor segmentation based on FR2PAAttU-Net model," *Frontiers Oncol.*, vol. 12, Mar. 2022, Art. no. 853281.
- [130] C. Li, Y. Tan, W. Chen, X. Luo, Y. Gao, X. Jia, and Z. Wang, "Attention UNet++: A nested attention-aware U-Net for liver CT image segmentation," in *Proc. IEEE Int. Conf. Image Process. (ICIP)*, Oct. 2020, pp. 345–349.
- [131] Q. Jin, Z. Meng, C. Sun, H. Cui, and R. Su, "RA-UNet: A hybrid deep attention-aware network to extract liver and tumor in CT scans," *Frontiers Bioeng. Biotechnol.*, vol. 8, p. 1471, Dec. 2020.
- [132] A. Machireddy, N. Meermeier, F. Coakley, and X. Song, "Malignancy detection in prostate multi-parametric MR images using U-net with attention," in *Proc. 42nd Annu. Int. Conf. IEEE Eng. Med. Biol. Soc. (EMBC)*, Jul. 2020, pp. 1520–1523.
- [133] X. Shen, J. Xu, H. Jia, P. Fan, F. Dong, B. Yu, and S. Ren, "Self-attentional microvessel segmentation via squeeze-excitation transformer UNet," *Computerized Med. Imag. Graph.*, vol. 97, Apr. 2022, Art. no. 102055.
- [134] X.-F. Du, J.-S. Wang, and W.-Z. Sun, "UNet retinal blood vessel segmentation algorithm based on improved pyramid pooling method and attention mechanism," *Phys. Med. Biol.*, vol. 66, no. 17, Sep. 2021, Art. no. 175013.
- [135] J. Shi, Y. Ye, D. Zhu, L. Su, Y. Huang, and J. Huang, "Comparative analysis of pulmonary nodules segmentation using multiscale residual U-Net and fuzzy C-means clustering," *Comput. Methods Programs Biomed.*, vol. 209, Sep. 2021, Art. no. 106332.
- [136] S. Bhatia, S. Alam, M. Shuaib, M. Hameed Alhameed, F. Jeribi, and R. I. Alsuwailam, "Retinal vessel extraction via assisted multi-channel feature map and U-Net," *Frontiers Public Health*, vol. 10, Mar. 2022, Art. no. 858327.
- [137] M. E. Gegundez-Arias, D. Marin-Santos, I. Perez-Borrero, and M. J. Vasallo-Vazquez, "A new deep learning method for blood vessel segmentation in retinal images based on convolutional kernels and modified U-Net model," *Comput. Methods Programs Biomed.*, vol. 205, Jun. 2021, Art. no. 106081.
- [138] J. Wang, X. Li, P. Lv, and C. Shi, "SERR-U-Net: Squeeze-and-excitation residual and recurrent block-based U-net for automatic vessel segmentation in retinal image," *Comput. Math. Methods Med.*, vol. 2021, pp. 1–16, Aug. 2021.
- [139] C. Guo, M. Szemenyei, Y. Yi, W. Wang, B. Chen, and C. Fan, "SA-UNet: Spatial attention U-Net for retinal vessel segmentation," in *Proc. 25th Int. Conf. Pattern Recognit. (ICPR)*, Jan. 2021, pp. 1236–1242.
- [140] S. Woo, J. Park, J. Y. Lee, and I. S. Kweon, "CBAM: Convolutional block attention module," in *Proc. Eur. Conf. Comput. Vis. (ECCV)*, Sep. 2018, pp. 3–19.
- [141] P. K. Jain, N. Sharma, A. A. Giannopoulos, L. Saba, A. Nicolaidis, and J. S. Suri, "Hybrid deep learning segmentation models for atherosclerotic plaque in internal carotid artery B-mode ultrasound," *Comput. Biol. Med.*, vol. 136, Sep. 2021, Art. no. 104721.
- [142] X. Li, H. Chen, X. Qi, Q. Dou, C.-W. Fu, and P.-A. Heng, "H-DenseUNet: Hybrid densely connected UNet for liver and tumor segmentation from CT volumes," *IEEE Trans. Med. Imag.*, vol. 37, no. 12, pp. 2663–2674, Dec. 2018.
- [143] A. Y. Yuan, "Hybrid deep learning network for vascular segmentation in photoacoustic imaging," *Biomed. Opt. Exp.*, vol. 11, no. 11, pp. 6445–6457, 2020.
- [144] R. Zhou, F. Guo, M. R. Azarpazhooh, S. Hashemi, X. Cheng, J. D. Spence, M. Ding, and A. Fenster, "Deep learning-based measurement of total plaque area in B-mode ultrasound images," *IEEE J. Biomed. Health Informat.*, vol. 25, no. 8, pp. 2967–2977, Aug. 2021.
- [145] A. Das, "Adaptive UNet-based lung segmentation and ensemble learning with CNN-based deep features for automated COVID-19 diagnosis," *Multimedia Tools Appl.*, vol. 81, no. 4, pp. 5407–5441, Feb. 2022.
- [146] Z. Fatemeh, S. Nicola, K. Sathesh, and U. Eranga, "Ensemble U-Net-based method for fully automated detection and segmentation of renal masses on computed tomography images," *Med. Phys.*, vol. 47, no. 9, pp. 4032–4044, Sep. 2020.
- [147] Y. Li, X. Huang, Y. Wang, Z. Xu, Y. Sun, and Q. Zhang, "U-Net ensemble model for segmentation in Histopathology images," in *Proc. MICCAI Workshop*, 2019.
- [148] W. H. Khoong, "BUSU-Net: An ensemble U-Net framework for medical image segmentation," 2020, *arXiv:2003.01581*.
- [149] C. Huang, Y. Lan, G. Xu, X. Zhai, J. Wu, F. Lin, N. Zeng, Q. Hong, E. Y. K. Ng, Y. Peng, F. Chen, and G. Zhang, "A deep segmentation network of multi-scale feature fusion based on attention mechanism for IVOCT lumen contour," *IEEE/ACM Trans. Comput. Biol. Bioinf.*, vol. 18, no. 1, pp. 62–69, Jan. 2021.
- [150] N. Ibtihaz and M. S. Rahman, "MultiResUNet: Rethinking the U-Net architecture for multimodal biomedical image segmentation," *Neural Netw.*, vol. 121, pp. 74–87, Jan. 2020.
- [151] S. Momin, Y. Lei, N. S. McCall, J. Zhang, J. Roper, J. Harms, S. Tian, M. S. Lloyd, T. Liu, J. D. Bradley, K. Higgins, and X. Yang, "Mutual enhancing learning-based automatic segmentation of CT cardiac substructure," *Phys. Med. Biol.*, vol. 67, no. 10, May 2022, Art. no. 105008.
- [152] E. D. Morris, A. I. Ghanem, M. Dong, M. V. Pantelic, E. M. Walker, and C. K. Glide-Hurst, "Cardiac substructure segmentation with deep learning for improved cardiac sparing," *Med. Phys.*, vol. 47, no. 2, pp. 576–586, Feb. 2020.
- [153] J. Jin, H. Zhu, Y. Teng, Y. Ai, C. Xie, and X. Jin, "The accuracy and radiomics feature effects of multiple U-Net-based automatic segmentation models for transvaginal ultrasound images of cervical cancer," *J. Digit. Imag.*, vol. 35, pp. 983–992, Mar. 2022.
- [154] L. Pan, "Aging of Chinese bony orbit: Automatic calculation based on UNet++ and connected component analysis," *Surgical Radiolog. Anatomy*, vol. 44, pp. 749–758, Apr. 2022.
- [155] N. Jávorszky, "Deep learning-based atherosclerotic coronary plaque segmentation on coronary CT angiography," *Eur. Radiol.*, vol. 32, pp. 7217–7226, May 2022.
- [156] C. Balakrishna, S. Dadashzadeh, and S. Soltaninejad, "Automatic detection of lumen and media in the IVUS images using U-Net with VGG16 encoder," 2018, *arXiv:1806.07554*.
- [157] H. Huang, L. Lin, R. Tong, H. Hu, Q. Zhang, Y. Iwamoto, X. Han, Y.-W. Chen, and J. Wu, "UNet 3+: A full-scale connected UNet for medical image segmentation," in *Proc. IEEE Int. Conf. Acoust., Speech Signal Process. (ICASSP)*, May 2020, pp. 1055–1059.
- [158] M. Wang, H. Jiang, T. Shi, and Y.-D. Yao, "HD-RDS-UNet: Leveraging spatial-temporal correlation between the decoder feature maps for lymphoma segmentation," *IEEE J. Biomed. Health Informat.*, vol. 26, no. 3, pp. 1116–1127, Mar. 2022.
- [159] M. Xia, W. Yan, Y. Huang, Y. Guo, G. Zhou, and Y. Wang, "Extracting membrane borders in IVUS images using a multi-scale feature aggregated U-Net," in *Proc. 42nd Annu. Int. Conf. IEEE Eng. Med. Biol. Soc. (EMBC)*, Jul. 2020, pp. 1650–1653.

- [160] R. Bajaj, X. Huang, Y. Kilic, A. Ramasamy, A. Jain, M. Ozkor, V. Tufaro, H. Safi, E. Erdogan, P. W. Serruys, J. Moon, F. Pugliese, A. Mathur, R. Torii, A. Baumbach, J. Dijkstra, Q. Zhang, and C. V. Bourantas, "Advanced deep learning methodology for accurate, real-time segmentation of high-resolution intravascular ultrasound images," *Int. J. Cardiol.*, vol. 339, pp. 185–191, Sep. 2021.
- [161] R. Arora, I. Saini, and N. Sood, "Multi-label segmentation and detection of COVID-19 abnormalities from chest radiographs using deep learning," *Optik*, vol. 246, Nov. 2021, Art. no. 167780.
- [162] J. Yang, M. Faraji, and A. Basu, "Robust segmentation of arterial walls in intravascular ultrasound images using dual path U-Net," *Ultrasonics*, vol. 96, pp. 24–33, Jul. 2019.
- [163] S. K. Hasan and C. A. Linte, "CondenseUNet: A memory-efficient condensely-connected architecture for bi-ventricular blood pool and myocardium segmentation," in *Proc. SPIE*, vol. 2020, vol. 1315, pp. 402–408, Mar. 2020.
- [164] D. Bhattacharya, C. Betz, D. Eggert, and A. Schlaefler, "Self-supervised U-Net for segmenting flat and sessile polyps," 2021, *arXiv:2110.08776*.
- [165] H. Lu, Y. She, J. Tie, and S. Xu, "Half-UNet: A simplified U-Net architecture for medical image segmentation," *Frontiers Neuroinform.*, vol. 16, Jun. 2022, Art. no. 911679.
- [166] K. He, X. Zhang, S. Ren, and J. Sun, "Deep residual learning for image recognition," in *Proc. IEEE Conf. Comput. Vis. Pattern Recognit. (CVPR)*, Jun. 2016, pp. 770–778.
- [167] A. Krizhevsky, I. Sutskever, and G. E. Hinton, "ImageNet classification with deep convolutional neural networks," *Commun. ACM*, vol. 60, no. 2, pp. 84–90, Jun. 2012.
- [168] K. Simonyan and A. Zisserman, "Very deep convolutional networks for large-scale image recognition," 2014, *arXiv:1409.1556*.
- [169] A. G. Howard, M. Zhu, B. Chen, D. Kalenichenko, W. Wang, T. Weyand, M. Andreetto, and H. Adam, "MobileNets: Efficient convolutional neural networks for mobile vision applications," 2017, *arXiv:1704.04861*.
- [170] M. Sandler, A. Howard, M. Zhu, A. Zhmoginov, and L.-C. Chen, "MobileNetV2: Inverted residuals and linear bottlenecks," in *Proc. IEEE/CVF Conf. Comput. Vis. Pattern Recognit.*, Jun. 2018, pp. 4510–4520.
- [171] N. Ma, X. Zhang, H.-T. Zheng, and J. Sun, "ShuffleNet V2: Practical guidelines for efficient CNN architecture design," in *Proc. Eur. Conf. Comput. Vis. (ECCV)*, Sep. 2018, pp. 116–131.
- [172] K. Han, Y. Wang, Q. Tian, J. Guo, C. Xu, and C. Xu, "GhostNet: More features from cheap operations," in *Proc. IEEE/CVF Conf. Comput. Vis. Pattern Recognit. (CVPR)*, Jun. 2020, pp. 1580–1589.
- [173] A. A. Albishri, S. J. H. Shah, S. S. Kang, and Y. Lee, "AM-UNet: Automated mini 3D end-to-end U-Net based network for brain claustrium segmentation," *Multimedia Tools Appl.*, vol. 81, pp. 36171–36194, Jan. 2022.
- [174] A. A. Albishri, S. J. H. Shah, A. Schmiedler, S. S. Kang, and Y. Lee, "Automated human claustrium segmentation using deep learning technologies," 2019, *arXiv:1911.07515*.
- [175] B. Baheti, S. Innani, S. Gajre, and S. Talbar, "Eff-UNet: A novel architecture for semantic segmentation in unstructured environment," in *Proc. IEEE/CVF Conf. Comput. Vis. Pattern Recognit. Workshops (CVPRW)*, Jun. 2020, pp. 358–359.
- [176] M. Tan and Q. Le, "EfficientNet: Rethinking model scaling for convolutional neural networks," in *Proc. Int. Conf. Mach. Learn.*, 2019, pp. 6105–6114.
- [177] L. Liu, J. Cheng, Q. Quan, F.-X. Wu, Y.-P. Wang, and J. Wang, "A survey on U-shaped networks in medical image segmentations," *Neurocomputing*, vol. 409, pp. 244–258, Oct. 2020.
- [178] J. S. Suri, "COVLIAS 1.0 Lesion vs. MedSeg: An artificial intelligence framework for automated lesion segmentation in COVID-19 lung computed tomography scans," *Diagnostics*, vol. 12, no. 5, p. 1283, May 2022.
- [179] J. S. Suri, "COVLIAS 2.0-cXAI: Cloud-based explainable deep learning system for COVID-19 lesion localization in computed tomography scans," *Diagnostics*, vol. 12, no. 6, p. 1482, Jun. 2022.
- [180] M. Biswas, V. Kuppli, T. Araki, D. R. Edla, E. C. Godia, L. Saba, H. S. Suri, T. Omerzu, J. R. Laird, N. N. Khanna, A. Nicolaides, and J. S. Suri, "Deep learning strategy for accurate carotid intima-media thickness measurement: An ultrasound study on Japanese diabetic cohort," *Comput. Biol. Med.*, vol. 98, pp. 100–117, Jul. 2018.
- [181] F. Molinari, G. Zeng, and J. S. Suri, "An integrated approach to computer-based automated tracing and its validation for 200 common carotid arterial wall ultrasound images: A new technique," *J. Ultrasound Med.*, vol. 29, no. 3, pp. 399–418, Mar. 2010.
- [182] K. M. Meiburger, "Automated carotid artery intima layer regional segmentation," *Phys. Med. Biol.*, vol. 56, no. 13, p. 4073, 2011.
- [183] F. Molinari, C. S. Pattichis, G. Zeng, L. Saba, U. R. Acharya, R. Sanfilippo, A. Nicolaides, and J. S. Suri, "Completely automated multiresolution edge snapper—A new technique for an accurate carotid ultrasound IMT measurement: Clinical validation and benchmarking on a multi-institutional database," *IEEE Trans. Image Process.*, vol. 21, no. 3, pp. 1211–1222, Mar. 2012.
- [184] F. Molinari, K. M. Meiburger, G. Zeng, U. R. Acharya, W. Liboni, A. Nicolaides, and J. S. Suri, "Carotid artery recognition system: A comparison of three automated paradigms for ultrasound images," *Med. Phys.*, vol. 39, no. 1, pp. 378–391, Dec. 2011.
- [185] K. Liu and J. S. Suri, "Automatic vessel identification for angiographic screening," U.S. Patent, 6 845 260 B2, Jan. 18, 2005.
- [186] L. Jin, "3AU-Net: Triple attention U-Net for retinal vessel segmentation," in *Proc. IEEE 2nd Int. Conf. Civil Aviation Saf. Inf. Technol. (ICCASIT)*, Oct. 2020, pp. 612–615.
- [187] Y. He, G. Yang, J. Yang, Y. Chen, Y. Kong, J. Wu, L. Tang, X. Zhu, J.-L. Dillenseger, P. Shao, S. Zhang, H. Shu, J.-L. Coatrieux, and S. Li, "Dense biased networks with deep priori anatomy and hard region adaptation: Semi-supervised learning for fine renal artery segmentation," *Med. Image Anal.*, vol. 63, Jul. 2020, Art. no. 101722.
- [188] S. P. Vacacela and M. E. Benalcázar, "2D semantic segmentation of the prostate gland in magnetic resonance images using convolutional neural networks," *IFAC-PapersOnLine*, vol. 54, no. 15, pp. 394–399, 2021.
- [189] L. Umapathy, W. Unger, F. Shareef, H. Arif, D. Martin, M. Altbach, and A. Bilgin, "A cascaded residual UNET for fully automated segmentation of prostate and peripheral zone in T2-weighted 3D fast spin echo images," 2020, *arXiv:2012.13501*.
- [190] G. Zeng, X. Yang, J. Li, L. Yu, P.-A. Heng, and G. Zheng, "3D U-Net with multi-level deep supervision: Fully automatic segmentation of proximal femur in 3D MR images," in *Proc. Int. Workshop Mach. Learn. Med. Imag.*, Cham, Switzerland: Springer, 17, pp. 274–282.
- [191] C. Wang, H. R. Roth, T. Kitasaka, M. Oda, Y. Hayashi, Y. Yoshino, T. Yamamoto, N. Sassa, M. Goto, and K. Mori, "Precise estimation of renal vascular dominant regions using spatially aware fully convolutional networks, tensor-cut and Voronoi diagrams," *Computerized Med. Imag. Graph.*, vol. 77, Oct. 2019, Art. no. 101642.
- [192] C. Li, Y. Tian, W. Li, J. Tian, and F. Zhou, "Low-contrast defects recognition using low-order residual network," *IEEE Access*, vol. 7, pp. 91193–91201, 2019.
- [193] D. Gunning and D. Aha, "DARPA's explainable artificial intelligence (XAI) program," *AI Mag.*, vol. 40, no. 2, pp. 44–58, Jun. 2019.
- [194] A. B. Arrieta, N. Díaz-Rodríguez, J. Del Ser, A. Bennetot, S. Tabik, A. Barbado, S. Garcia, S. Gil-Lopez, D. Molina, R. Benjamins, R. Chatila, and F. Herrera, "Explainable artificial intelligence (XAI): Concepts, taxonomies, opportunities and challenges toward responsible AI," *Inf. Fusion*, vol. 58, pp. 82–115, Jun. 2020.
- [195] L. Saba, R. Sanfilippo, S. Sannia, M. Anzidei, R. Montisci, G. Mallarini, and J. S. Suri, "Association between carotid artery plaque volume, composition, and ulceration: A retrospective assessment with MDCT," *Amer. J. Roentgenol.*, vol. 199, no. 1, pp. 151–156, Jul. 2012.
- [196] N. Ikeda, "Improved correlation between carotid and coronary atherosclerosis SYNTAX score using automated ultrasound carotid bulb plaque IMT measurement," *Ultrasound Med. Biol.*, vol. 41, no. 5, pp. 1247–1262, 2015.
- [197] T. Araki, N. Ikeda, D. Shukla, P. K. Jain, N. D. Londhe, V. K. Shrivastava, S. K. Banchhor, L. Saba, A. Nicolaides, S. Shafique, J. R. Laird, and J. S. Suri, "PCA-based polling strategy in machine learning framework for coronary artery disease risk assessment in intravascular ultrasound: A link between carotid and coronary grayscale plaque morphology," *Comput. Methods Programs Biomed.*, vol. 128, pp. 137–158, May 2016.
- [198] D. W. Apley and J. Zhu, "Visualizing the effects of predictor variables in black box supervised learning models," *J. Roy. Stat. Soc., Ser. B Stat. Methodol.*, vol. 82, no. 4, pp. 1059–1086, Sep. 2020.
- [199] S. M. Lundberg and S.-I. Lee, "A unified approach to interpreting model predictions," in *Proc. Adv. Neural Inf. Process. Syst.*, vol. 30, 2017, pp. 1–10.
- [200] L. McInnes, J. Healy, and J. Melville, "UMAP: Uniform manifold approximation and projection for dimension reduction," 2018, *arXiv:1802.03426*.

- [201] G. Yang, Q. Ye, and J. Xia, "Unbox the black-box for the medical explainable AI via multi-modal and multi-centre data fusion: A mini-review, two showcases and beyond," *Inf. Fusion*, vol. 77, pp. 29–52, Jan. 2022.
- [202] D. D. Gunashekar et al., "Explainable AI for CNN-based prostate tumor segmentation in multi-parametric MRI correlated to whole mount histopathology," *Radiat. Oncol.*, vol. 17, p. 65, 2022, doi: 10.1186/s13014-022-02035-0.
- [203] P. Schelb, A. A. Tavakoli, T. Tubtawee, T. Hielscher, J.-P. Radtke, M. Görtz, V. Schutz, T. A. Kuder, L. Schimmöller, A. Stenzinger, M. Hohenfellner, H.-P. Schlemmer, and D. Bonekamp, "Comparison of prostate MRI lesion segmentation agreement between multiple radiologists and a fully automatic deep learning system," *RöFo Fortschritte Auf Dem Gebiet Der Röntgenstrahlen Und Der Bildgebenden Verfahren*, vol. 193, no. 5, pp. 559–573, May 2021.
- [204] L. O. Teixeira, R. M. Pereira, D. Bertolini, L. S. Oliveira, L. Nanni, G. D. C. Cavalcanti, and Y. M. G. Costa, "Impact of lung segmentation on the diagnosis and explanation of COVID-19 in chest X-ray images," *Sensors*, vol. 21, no. 21, p. 7116, Oct. 2021.
- [205] A. Chattopadhyay, A. Sarkar, P. Howlader, and V. N. Balasubramanian, "Grad-CAM++: Generalized gradient-based visual explanations for deep convolutional networks," in *Proc. IEEE Winter Conf. Appl. Comput. Vis. (WACV)*, Mar. 2018, pp. 839–847.
- [206] S. S. Sanagala, A. Nicolaidis, S. K. Gupta, V. K. Koppula, L. Saba, S. Agarwal, A. M. Johri, M. S. Kalra, and J. S. Suri, "Ten fast transfer learning models for carotid ultrasound plaque tissue characterization in augmentation framework embedded with heatmaps for stroke risk stratification," *Diagnostics*, vol. 11, no. 11, p. 2109, Nov. 2021.
- [207] M. Agarwal, "Eight pruning deep learning models for low storage and high-speed COVID-19 computed tomography lung segmentation and heatmap-based lesion localization: A multicenter study using COVLIAS 2.0," *Comput. Biol. Med.*, vol. 146, Jul. 2022, Art. no. 105571.
- [208] F. Dubost, "GP-UNet: Lesion detection from weak labels with a 3D regression network," in *Proc. Int. Conf. Med. Image Comput. Comput.-Assist. Intervent*, Cham, Switzerland: Springer, 2017, pp. 214–221.
- [209] S. Chatterjee, A. Das, C. Mandal, B. Mukhopadhyay, M. Vipinraj, A. Shukla, R. N. Rao, C. Sarasaen, O. Speck, and A. Nürnberger, "TorchEsegeta: Framework for interpretability and explainability of image-based deep learning models," *Appl. Sci.*, vol. 12, no. 4, p. 1834, Feb. 2022.
- [210] S. Chatterjee, K. Prabhu, M. Pattadkal, G. Bortsova, C. Sarasaen, F. Dubost, H. Mattern, M. de Bruijne, O. Speck, and A. Nürnberger, "DS6, deformation-aware semi-supervised learning: Application to small vessel segmentation with noisy training data," 2020, *arXiv:2006.10802*.
- [211] S. Dasanayaka, V. Shantha, S. Silva, D. Meedeniya, and T. Ambegoda, "Interpretable machine learning for brain tumour analysis using MRI and whole slide images," *Softw. Impacts*, vol. 13, Aug. 2022, Art. no. 100340.
- [212] A. Myronenko, "3D MRI brain tumor segmentation using autoencoder regularization," in *Proc. Int. MICCAI Brainlesion Workshop*, Cham, Switzerland: Springer, 2018, pp. 311–320.
- [213] D. Melching, T. Strohmann, G. Requena, and E. Breitbarth, "Explainable machine learning for precise fatigue crack tip detection," *Sci. Rep.*, vol. 12, no. 1, pp. 1–14, Jun. 2022.
- [214] S. Poudel and S.-W. Lee, "Explainable U-Net model for Medical image segmentation," *Nordic Mach. Intell.*, vol. 1, no. 1, pp. 41–43, Nov. 2021.
- [215] X. Zhang and T. Chen, "Attention U-Net for interpretable classification on chest X-ray image," in *Proc. IEEE Int. Conf. Bioinf. Biomed. (BIBM)*, Dec. 2020, pp. 901–908.
- [216] J. Sun, F. Darbehani, M. Zaidi, and B. Wang, "SAUNet: Shape attentive U-Net for interpretable medical image segmentation," in *Proc. Int. Conf. Med. Image Comput. Comput.-Assist. Intervent*, Cham, Switzerland: Springer, 2020, pp. 797–806.
- [217] U. Acharya, M. Mookiah, S. V. Sree, R. Yanti, R. Martis, L. Saba, F. Molinari, S. Guerriero, and J. Suri, "Evolutionary algorithm-based classifier parameter tuning for automatic ovarian cancer tissue characterization and classification," *Ultraschall der Medizin Eur. J. Ultrasound*, vol. 35, no. 3, pp. 237–245, Dec. 2012.
- [218] Z. Zhuang, "Discrimination-aware channel pruning for deep neural networks," in *Proc. Adv. Neural Inf. Process. Syst.*, vol. 31, 2018, pp. 1–12.
- [219] Y. Jang, S. Lee, and J. Kim, "Compressing convolutional neural networks by pruning density peak filters," *IEEE Access*, vol. 9, pp. 8278–8285, 2021.
- [220] M. Hajabdollahi, R. Esfandiarpour, K. Najarian, N. Karimi, S. Samavi, and S. M. R. Soroushmehr, "Hierarchical pruning for simplification of convolutional neural networks in diabetic retinopathy classification," in *Proc. 41st Annu. Int. Conf. IEEE Eng. Med. Biol. Soc. (EMBC)*, Jul. 2019, pp. 970–973.
- [221] F. Tung and G. Mori, "Deep neural network compression by in-parallel pruning-quantization," *IEEE Trans. Pattern Anal. Mach. Intell.*, vol. 42, no. 3, pp. 568–579, Mar. 2018.
- [222] E. Jeczmiónek and P. A. Kowalski, "Flattening layer pruning in convolutional neural networks," *Symmetry*, vol. 13, no. 7, p. 1147, Jun. 2021.
- [223] J. Wang, S. Li, and W. Wang, "SVD-based channel pruning for convolutional neural network in acoustic scene classification model," in *Proc. IEEE Int. Conf. Multimedia Expo. Workshops (ICMEW)*, Jul. 2019, pp. 390–395.
- [224] L. Chen, S. Gong, X. Shi, and M. Shang, "Dynamical convolutional neural network channel pruning by genetic wavelet channel search for image classification," *Frontiers Comput. Neurosci.*, vol. 15, p. 95, Oct. 2021.
- [225] S. Tan, W. Wu, Z. Shao, Q. Li, B. Li, and J. Huang, "CALPA-NET: Channel-pruning-assisted deep residual network for steganalysis of digital images," *IEEE Trans. Inf. Forensics Security*, vol. 16, pp. 131–146, 2021.
- [226] R. K. Samala, H.-P. Chan, L. M. Hadjiiski, M. A. Helvie, C. Richter, and K. Cha, "Evolutionary pruning of transfer learned deep convolutional neural network for breast cancer diagnosis in digital breast tomosynthesis," *Phys. Med. Biol.*, vol. 63, no. 9, May 2018, Art. no. 095005.
- [227] Y. He, X. Zhang, and J. Sun, "Channel pruning for accelerating very deep neural networks," in *Proc. IEEE Int. Conf. Comput. Vis. (ICCV)*, Oct. 2017, pp. 1389–1397.
- [228] A. Chowdhury, A. Santamaria-Pang, J. R. Kubricht, J. Qiu, and P. Tu, "Symbolic semantic segmentation and interpretation of COVID-19 lung infections in chest CT volumes based on emergent languages," 2020, *arXiv:2008.09866*.
- [229] H. Hu, R. Peng, Y.-W. Tai, and C.-K. Tang, "Network trimming: A data-driven neuron pruning approach towards efficient deep architectures," 2016, *arXiv:1607.03250*.
- [230] M. M. S. Rani, P. Chitra, S. Lakshmanan, M. K. Devi, R. Sangeetha, and S. Nithya, "DeepCompNet: A novel neural net model compression architecture," *Comput. Intell. Neurosci.*, vol. 2022, pp. 1–13, Feb. 2022.
- [231] G. Tian, J. Chen, X. Zeng, and Y. Liu, "Pruning by training: A novel deep neural network compression framework for image processing," *IEEE Signal Process. Lett.*, vol. 28, pp. 344–348, 2021.
- [232] T. Wu, X. Li, D. Zhou, N. Li, and J. Shi, "Differential evolution based layer-wise weight pruning for compressing deep neural networks," *Sensors*, vol. 21, no. 3, p. 880, Jan. 2021.
- [233] S. Watanabe and H. Yamana, "Deep neural network pruning using persistent homology," in *Proc. IEEE 3rd Int. Conf. Artif. Intell. Knowl. Eng. (AIKE)*, Dec. 2020, pp. 153–156.
- [234] X. Xu, M. S. Park, and C. Brick, "Hybrid pruning: Thinner sparse networks for fast inference on edge devices," 2018, *arXiv:1811.00482*.
- [235] D. Wen, J. Jiang, J. Xu, K. Wang, T. Xiao, Y. Zhao, and Y. Dou, "RFC-HyPGCN: A runtime sparse feature compress accelerator for skeleton-based GCNs action recognition model with hybrid pruning," in *Proc. IEEE 32nd Int. Conf. Appl.-Specific Syst., Archit. Processors (ASAP)*, Jul. 2021, pp. 33–40.
- [236] C. Guo and P. Li, "Hybrid pruning method based on convolutional neural network sensitivity and statistical threshold," *J. Phys., Conf. Ser.*, vol. 2171, no. 1, Jan. 2022, Art. no. 012055.
- [237] J.-H. Luo, J. Wu, and W. Lin, "ThiNet: A filter level pruning method for deep neural network compression," in *Proc. IEEE Int. Conf. Comput. Vis. (ICCV)*, Oct. 2017, pp. 5058–5066.
- [238] H. Li, A. Kadav, I. Durdanovic, H. Samet, and H. P. Graf, "Pruning filters for efficient ConvNets," 2016, *arXiv:1608.08710*.
- [239] Y. Zhang, Y. Yuan, and Q. Wang, "ACP: Adaptive channel pruning for efficient neural networks," in *Proc. IEEE Int. Conf. Acoust., Speech Signal Process. (ICASSP)*, May 2022, pp. 4488–4492.
- [240] T. Choudhary, V. Mishra, A. Goswami, and J. Sarangapani, "Heuristic-based automatic pruning of deep neural networks," *Neural Comput. Appl.*, vol. 34, no. 6, pp. 4889–4903, Mar. 2022.
- [241] C. Y. Guo and P. Li, "Hybrid pruning for convolutional neural network convolution kernel," in *Proc. 4th Int. Conf. Adv. Electron. Mater., Comput. Softw. Eng. (AEMCSE)*, Mar. 2021, pp. 432–438.

- [242] B. Jena, S. Saxena, G. K. Nayak, L. Saba, N. Sharma, and J. S. Suri, "Artificial intelligence-based hybrid deep learning models for image classification: The first narrative review," *Comput. Biol. Med.*, vol. 137, Oct. 2021, Art. no. 104803.
- [243] J. S. Suri, S. Agarwal, S. Gupta, A. Puvvula, K. Viskovic, N. Suri, A. Alizad, A. El-Baz, L. Saba, M. Fatemi, and D. S. Naidu, "Systematic review of artificial intelligence in acute respiratory distress syndrome for COVID-19 lung patients: A biomedical imaging perspective," *IEEE J. Biomed. Health Informat.*, vol. 25, no. 11, pp. 4128–4139, Nov. 2021.
- [244] S. Paul, "Bias investigation in artificial intelligence systems for early detection of Parkinson's disease: A narrative review," *Diagnostics*, vol. 12, no. 1, p. 166, 2022.
- [245] N. Gupta, S. K. Gupta, R. K. Pathak, V. Jain, P. Rashidi, and J. S. Suri, "Human activity recognition in artificial intelligence framework: A narrative review," *Artif. Intell. Rev.*, vol. 55, pp. 4755–4808, Jan. 2022.
- [246] N. Siddique, S. Paheding, C. P. Elkin, and V. Devabhaktuni, "U-Net and its variants for medical image segmentation: A review of theory and applications," *IEEE Access*, vol. 9, pp. 82031–82057, 2021.
- [247] G. Du, X. Cao, J. Liang, X. Chen, and Y. Zhan, "Medical image segmentation based on U-Net: A review," *J. Imag. Sci. Technol.*, vol. 64, no. 2, 2020, Art. no. 20508.
- [248] G. Samarasinghe, M. Jameson, S. Vinod, M. Field, J. Dowling, A. Sowmya, and L. Holloway, "Deep learning for segmentation in radiation therapy planning: A review," *J. Med. Imag. Radiat. Oncol.*, vol. 65, no. 5, pp. 578–595, Aug. 2021.
- [249] A. Lagree, M. Mohebpour, N. Meti, K. Saednia, F.-I. Lu, E. Slodkowska, S. Gandhi, E. Rakovitch, A. Shenfield, A. Sadeghi-Naini, and W. T. Tran, "A review and comparison of breast tumor cell nuclei segmentation performances using deep convolutional neural networks," *Sci. Rep.*, vol. 11, no. 1, pp. 1–11, Apr. 2021.
- [250] S. B. Saadi, R. Ranjbarzadeh, O. Kazemi, A. Amirabadi, S. J. Ghouschi, O. Kazemi, S. Azadikhah, and M. Bendecheche, "Osteolysis: A literature review of basic science and potential computer-based image processing detection methods," *Comput. Intell. Neurosci.*, vol. 2021, pp. 1–21, Oct. 2021.
- [251] N. S. Punn and S. Agarwal, "Modality specific U-Net variants for biomedical image segmentation: A survey," 2021, *arXiv:2107.04537*.
- [252] X.-X. Yin, L. Sun, Y. Fu, R. Lu, and Y. Zhang, "U-Net-based medical image segmentation," *J. Healthcare Eng.*, vol. 2022, Apr. 2022, Art. no. 4189781.
- [253] Y. He, "Image-to-image translation of label-free molecular vibrational images for a histopathological review using the UNet+seg-cGAN model," *Biomed. Opt. Exp.*, vol. 13, no. 4, pp. 1924–1938, 2022.
- [254] J. Wu, W. Liu, C. Li, T. Jiang, I. M. Shariful, H. Sun, X. Li, X. Li, X. Huang, and M. Grzegorzec, "A state-of-the-art survey of U-Net in microscopic image analysis: From simple usage to structure mortification," 2022, *arXiv:2202.06465*.
- [255] Y.-W. Fan, W.-H. Liu, Y.-T. Chen, Y.-C. Hsu, N. Pathak, Y.-W. Huang, and J.-M. Yang, "Exploring kinase family inhibitors and their moiety preferences using deep Shapley additive exPlanations," *BMC Bioinf.*, vol. 23, no. S4, pp. 1–18, Apr. 2022.
- [256] Y. Ning, M. E. H. Ong, B. Chakraborty, B. A. Goldstein, D. S. W. Ting, R. Vaughan, and N. Liu, "Shapley variable importance cloud for interpretable machine learning," *Patterns*, vol. 3, no. 4, Apr. 2022, Art. no. 100452.
- [257] J. S. Suri, S. Agarwal, B. Jena, S. Saxena, A. El-Baz, V. Agarwal, M. K. Kalra, L. Saba, K. Viskovic, M. Fatemi, and S. Naidu, "Five strategies for bias estimation in artificial intelligence-based hybrid deep learning for acute respiratory distress syndrome COVID-19 lung infected patients using AP(AI)Bias 2.0: A systematic review," *IEEE Trans. Instrum. Meas.*, early access, May 11, 2022, doi: [10.1109/TIM.2022.3174270](https://doi.org/10.1109/TIM.2022.3174270).
- [258] E. Brion, J. Léger, A. M. Barragán-Montero, N. Meert, J. A. Lee, and B. Macq, "Domain adversarial networks and intensity-based data augmentation for male pelvic organ segmentation in cone beam CT," *Comput. Biol. Med.*, vol. 131, Apr. 2021, Art. no. 104269.
- [259] X. Xia and B. Kulis, "W-Net: A deep model for fully unsupervised image segmentation," 2017, *arXiv:1711.08506*.
- [260] S. Xie, R. Girshick, P. Dollár, Z. Tu, and K. He, "Aggregated residual transformations for deep neural networks," in *Proc. IEEE Conf. Comput. Vis. Pattern Recognit. (CVPR)*, Jul. 2017, pp. 1492–1500.
- [261] F. Ryan, K. L.-L. Román, B. Z. Gerbolés, K. M. Rebesch, M. S. Txurio, R. C. Ugarte, M. J. G. González, and I. M. Oliver, "Unsupervised domain adaptation for the segmentation of breast tissue in mammography images," *Comput. Methods Programs Biomed.*, vol. 211, Nov. 2021, Art. no. 106368.
- [262] Z. Khan and J. Yang, "Bottom-up unsupervised image segmentation using FC-dense U-Net based deep representation clustering and multi-dimensional feature fusion based region merging," *Image Vis. Comput.*, vol. 94, Feb. 2020, Art. no. 103871.
- [263] K. Yao, J. Sun, K. Huang, L. Jing, H. Liu, D. Huang, and C. Jude, "Analyzing cell-scaffold interaction through unsupervised 3D nuclei segmentation," *Int. J. Bioprinting*, vol. 8, no. 1, p. 495, Dec. 2021.
- [264] A. Zakeri, A. Hokmabadi, N. Ravikumar, A. F. Frangi, and A. Gooya, "A probabilistic deep motion model for unsupervised cardiac shape anomaly assessment," *Med. Image Anal.*, vol. 75, Jan. 2022, Art. no. 102276.
- [265] N. Araslanov and S. Roth, "Self-supervised augmentation consistency for adapting semantic segmentation," in *Proc. IEEE/CVF Conf. Comput. Vis. Pattern Recognit. (CVPR)*, Jun. 2021, pp. 15384–15394.
- [266] C. Ma, "SSL-Unet: A self-supervised learning strategy base on U-Net for retinal vessel segmentation," TechRxiv, 2021, doi: [10.36227/techrxiv.16823236.v1](https://doi.org/10.36227/techrxiv.16823236.v1).
- [267] Y. Liu and W. Yang, "Automatic liver segmentation using U-Net in the assistance of CNN," in *Proc. Int. Conf. Intell. Comput., Autom. Syst. (ICICAS)*, Dec. 2020, pp. 367–371.



JASJIT S. SURI (Fellow, IEEE) received the M.B.A. and Ph.D. degrees. He is currently the Chairperson of AtheroPoint, Roseville, CA, USA, dedicated to imaging technologies for cardiovascular and stroke. He is an innovator, a visionary, a scientist, and an internationally known world leader in biomedical engineering and its management. He is a fellow of the American Institute of Medical and Biological Engineering, the American Society of Ultrasound in Medicine, the Society

of Vascular Medicine, and the Asia Pacific Vascular Society. He was a recipient of the Lifetime Achievement Award from Marquis. He received the Director General's Gold Medal, in 1980. He has won numerous awards, and has ~29,000 citations, coauthored 50 books, over 50 patents, more than 200 artificial intelligence international journal publications, and has an H-index of 82.



MRINALINI BHAGAWATI received the M.Tech. degree. She is currently working as a Doctoral Scholar at the Department of Biomedical Engineering, School of Technology, North-Eastern Hill University, Shillong, India. She has published several international journals. Her research interests include computational biology, cardiovascular diseases/stroke risk stratification, biomedical instrumentation, and artificial intelligence.



SUSHANT AGARWAL (Member, IEEE) received the degrees in deep learning, data science, and specialization artificial intelligence for medical imaging. He is currently with the Advanced Knowledge Engineering Centre, Global Biomedical Technologies Inc., Roseville, CA USA, and the TechNet Cyber Solutions Pvt. Ltd., Andhra Pradesh, India. He has been a top performer in various national and international competitions. He has experience in image segmentation and analysis with research

papers in COVID-19-based image analysis. He is a member of the IEEE Computer Society.



SUDIP PAUL (Senior Member, IEEE) received the Ph.D. degree. He completed his postdoctoral research at the School of Computer Science and Software Engineering, The University of Western Australia, Perth, WA, USA. He is currently an Assistant Professor and a Teacher In-Charge with the Biomedical Engineering Department, SOT, North-Eastern Hill University (NEHU), Shillong, India. His research interests include biomedical engineering, AI, neural, and cognitive disorders.



JOHN R. LAIRD is currently pursuing the M.D. degree with St. Helena Hospital, St. Helena, CA, USA. He is an internationally renowned interventional cardiologist and his expertise is innovative procedures for carotid artery disease. He is a FACC.



AMIT PANDEY received the M.Tech. degree in computer science from the Deenbandhuchotu Ram University of Science and Technology, Sonapat, Haryana, India. He is currently a Research Scholar with the Computer Science Department, Bennett University, Greater Noida, India. His research interests include semantic segmentation for biomedical image segmentation and explainable artificial intelligence.



AMER M. JOHRI received the M.D. and M.Sc. degrees. He is currently working as an Associate Professor with the Department of Medicine, Division of Cardiology, Queen's University. He is a FRCP and FASE. He was the Part Chair of the ASE Circulation & Vascular Ultrasound Council.



SUNEET K. GUPTA (Member, IEEE) received the Ph.D. degree. He has been working as a Professor with the Department of Computer Science Engineering, Bennett University, Greater Noida, since 2017. Recently, he has completed a project funded by CST, Uttar Pradesh, India. His current research interests include wireless sensor networks, the Internet of Things, and natural language processing and optimization of neural networks.



MANUDEEP K. KALRA received the M.D. degree. He is currently working as an Associate Professor of radiology with the Harvard Medical School, Radiologist, Divisions of Thoracic and Cardiovascular Imaging, Massachusetts General Hospital, Boston, MA, USA.



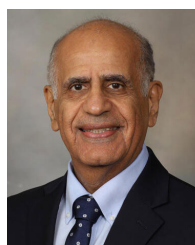
LUCA SABA is a Professor of radiology and Chief of the Department of Radiology with the University of Cagliari. His participation as lead author has resulted in more than 300 high-impact factor, peer-reviewed journal articles. His research interests include multi-detector-row computed tomography, magnetic resonance, ultrasound, neuroradiology, and diagnostic in vascular sciences.



MOSTAFA M. FOUDA (Senior Member, IEEE) received the Ph.D. degree in information sciences from Tohoku University, Japan, in 2011. He is currently an Assistant Professor with the Department of Electrical and Computer Engineering, Idaho State University, Pocatello, ID, USA. He also holds the position of an Associate Professor with Benha University, Egypt. His research interests include machine learning, the IoT, and 6G networks. He is an Editor of the IEEE TRANSACTIONS ON VEHICULAR TECHNOLOGY.



KOSMAS I. PARASKEVAS received the Ph.D. and M.D. degrees. He is currently a Vascular Specialist working with the Department of Vascular Surgery, Central Clinic of Athens, Athens, Greece. His research interests include carotid artery stenosis and abdominal aortic aneurysms.



MOSTAFA FATEMI (Life Fellow, IEEE) is currently an Electrical Engineer at the Mayo Clinic College of Medicine and Science, Rochester, MN, USA. His current research interests include ultrasonic methods for tissue viscoelasticity estimation for applications in cancer imaging and bladder function evaluation. He has published extensively in the field of medical ultrasound and holds ten patents in this field. He is an elected fellow of these institutions: AIMBE, ASA, and AIUM.



NARENDRA N. KHANNA received the M.D. and D.M. degrees. He is currently an Advisor of Apollo Group of Hospitals, India, and is also working as a Senior Consultant in cardiology and a Co-ordinator of vascular services at Indraprastha Apollo Hospital, New Delhi. He is a FACC.



SUBBARAM NAIDU (Life Fellow, IEEE) received the Ph.D. degree in electrical engineering (control systems engineering) from the Indian Institute of Technology (IIT), Kharagpur, India, in 1979. He has more than 220 publications. He has been nominated for the election to become a member of the NAE of the U.S. National Academies.

...